UNIVERSITÀ DEGLI STUDI DI TRIESTE

Dipartimento di Fisica

Corso di Laurea Magistrale in Fisica della Materia

Time resolved measurements of cuprate superconductors with stochastic and chirped light pulses

Misure risolte in tempo di cuprati superconduttori con impulsi di luce stocastici e non compressi

Relatore:
Prof. Daniele Fausti

Candidato:
Gabriele Bartolini
(Matr. SM2300705)

Correlatori:
Dott. Enrico Maria Rigoni

Dott.ssa Angela Montanaro

Anno accademico 2024/2025

Riassunto della tesi

Nella seguente tesi si riportano delle misure risolte in tempo di campioni del superconduttore ad alte temperature $Y - Bi_2Sr_2Ca_{0.92}Cu_2O_{\delta+8}$, della famiglia dei cuprati. I quattro campioni con diversi livelli di drogaggio sono stati analizzati utilizzando tecniche diverse per caratterizzare la risposta ottica del materiale in diverse temperature (e fasi). In particolare, dopo un'introduzione alle proprietà dei cuprati e ai concetti base di ottica non lineare, si presenta uno studio *pump-probe* dei modi elettronici B_{1g} e B_{2g} nel range $1.3 - 2\,\text{eV}$ tramite l'uso di un *probe* di luce bianca dopo un impulso di pompa nel medio infrarosso ($17\mu\text{m}$); la regione di energie individuata dal probe è accoppiata alle eccitazioni a basse energie. Le misure in temperatura di questi materiali sono servite a ottenere stime delle temperature di transizione T_c e T^*. Il segnale per i due modi risulta drasticamente diverso: il B_{1g} risulta molto debole e non particolarmente dipendente dal drogaggio, mentre il B_{2g} è ben visibile e il suo peso spettrale dipende visibilmente dal drogaggio, in particolare si sposta ad energie più basse all'aumentare di quest'ultimo.

In seguito si indaga un fenomeno di perturbazione del segnale in fase superconduttiva causato dall'introduzione di un *chirp* nell'impulso di *probe* che comporta la scomparsa del segnale nelle frequenze finali dell'impulso, presente altrimenti nelle misure ottenute con l'impulso compresso; gli effetti sono stati esaminati sia nella loro dipendenza dalla fluenza del *probe* che dal drogaggio del campione.

Nella parte successiva della tesi si mostrano misure di spettroscopia Raman elettronico risolte in tempo con risoluzione sub-picosecondo ottenute con la *Femtosecond Covariance Spectroscopy*, una tecnica che si basa sull' analisi delle correlazioni multimodo introdotte dal materiale in impulsi di *probe* spettralmente rumorosi. Il segnale di correlazione così ottenuto risulta presente non solo in fase superconduttiva, ma anche di pseudogap, suggerendo la presenza di accoppiamento locale. Il segnale misurato diminuisce di intensità al crescere della temperatura, scomparendo in fase normale, al di sopra della T^* stimata in precedenza.

" *Waiting. If you are sincere, you have light and success. Perseverance brings good fortune. It is advantageous to cross the great water.*"

I Ching, Hexagram 5 (Xū, Waiting)

Contents

Introduction

The language that atoms use to communicate and hold together the world we see around us is the electromagnetic field, and photons are its words; every chemical reaction, technology, and the fact itself that we can see is mediated through light. The understanding that light is the trace of all these interactions and how it behaves is one of the most important parts of modern physics. Moreover, light-matter interaction can be exploited to characterize materials which interacted with electromagnetic waves. This principle forms the foundation of spectroscopic techniques—experimental methods in which light interacts with a material and is subsequently measured to extract information about the material's properties.

With the advent of *ultrafast* laser sources, it became possible to study not only the equilibrium but also the dynamical response of materials to non-equilibrium stimulations [1], an approach that gives results unattainable in static way. In particular, ultrafast optical spectroscopy has proven to be a fundamental tool for investigating complex materials—often referred to as "quantum materials"—whose behavior deviates from that of systems historically described by the independent or nearly-independent electron paradigm [2], making their theoretical description a decades long challenge. In these materials, the interplay of vibrational, electronic, and magnetic degrees of freedom gives rise to exotic macroscopic phases. Non-equilibrium spectroscopy techniques give us the possibility to disentangle these features, allowing us to get closer to the origin of these properties. If we could comprehend them, we would be able to understand if it is possible and how to engineer these exotic phases and obtain, for example, materials capable of superconducting at room temperature.

In this thesis will focus on the non-equilibrium study of high-temperature superconductor $Y - Bi_2Sr_2Ca_{0.92}Cu_2O_{\delta+8}$, which belong to Cuprates, one of the most studied family of superconductors. In this class of materials, the pairing mechanism that allows the existence of superconductivity at such high temperatures is still a mystery after almost 40 years of theoretical and experimental efforts. Furthermore, this is not the only exotic phase displayed by unconventional superconductors. For example the pseudogap region is one of the must puzzling of the phase diagram, showing possible traces of local pairing without superconducting behavior. These superconductors present strong anisotropic properties (e.g., the superconducting gap with *d-wave* symmetry) and coupling between excitations at great energy differences. One of the typical approaches towards the study of such behaviors is the observation of electronic excitations characteristic of the superconducting phase. We explore the phenomena in two unprecedented ways: we characterize dynamics of the B_{1g} and B_{2g} electronic modes with (energy-resolved) birefringence measurements on a broadband visible/near-infrared spectrum, observing the spectral weight change caused by a mid-infrared excitations. These modes are Raman scattering channels that probe different regions of the Brillouin Zone of the material, and as a consequence different points of the superconducting gap. We then observe time-resolved electronic Raman scattering experiment where we access the sub-ps dynamics through the study of multimode correlations in the material.

The thesis is organized as it follows. In Section 1 the main properties of unconventional superconductors and their optical properties will be covered, together with the concepts of nonlinear spectroscopy and the particular setup used for our experiments. In section 2 the electronic modes of the material will be thus studied with pump and probe approach, using a white light supercontinuum probe to obtain a birefringence signal. In section 3 an unexpected phenomenon concerning the use of chirped light as a probe will be covered, while finally in section 4 the superconductor will be studied through the use of Femtosecond Covariance Spectroscopy, a unique technique that allows the collection of time-resolved Raman spectra in the form of statistical correlation.

1 High temperature superconductivity and nonlinear spectroscopy

In the following section we introduce the subject of our research and the general concepts of nonlinear and pump-probe measurements. In the first part we introduce the history and physical properties of high-temperature superconductors of the family of cuprates, that includes our sample; we will focus on the properties that can be probed through spectroscopic techninques. In the second part we will introduce the main aspects of nonlinear optics and its application in pump-probe measurements, that will then be explained. In the last two parts of the section we show some useful models and discoveries of non-equilibrium measurements on the materials of our interest and then the experimental setup that will be used throughout the whole thesis.

1.1 Cuprate High-Temperature superconductors

One of the most interesting and technologically useful discoveries of the last century was the superconducting phase. In 1911 H. K. Onnes managed, through his discoveries in helium liquefaction, to cool down mercury to temperatures close to the absolute zero. In the moment it reached 4.2 K he recorded a sudden drop in resistivity: it was the first observation of a phenomenon that would only be explained theoretically by Bardeen, Cooper and Schrieffer in 1957 (*BCS Theory*, [3]). The explanation was given in a very elegant model that described superconductivity through the coupling of bound electron-electron states (*Cooper pairs*) that occurs due to the electron interaction with the crystal lattice.

The next experimental and theoretical efforts pushed the limits of superconductivity and established that the phenomenon was confined at low temperatures. But in 1986 Bednorz and Müller [4] observed the same drop in resistivity in a sample of $LaBaCuO$, but at $35K$. This was not an exception to the results of BCS Theory: it was clear after finding other materials that had even higher critical temperatures that the phenomenon was something else entirely, the highly correlated ground state of this materials could not be explained by the same causes. After almost 40 years from the discovery of *High temperature superconductivity* there isn't a theory that describes it and great experimental and theoretical effort is still being directed to the study of these highly correlated materials, to discover what is the glue that binds electrons together, or to understand if this glue exists at all [5].

1.1.1 Cuprate structure and phases

Many materials based on different elements have shown the onset of a superconducting phase at high temperature. The most studied HTSC are copper based superconductors, called for this reason *Cuprates*. This class of ceramic materials shows a perovskite-like structure and they are characterized by layers of CuO_2 alternated by layers of an insulator that acts as a charge reservoir (e.g., the unit cell of BSCCO in figure 1). Most of the superconducting properties depend on the CuO_2 planes and interaction between layers is another missing piece of the puzzle.

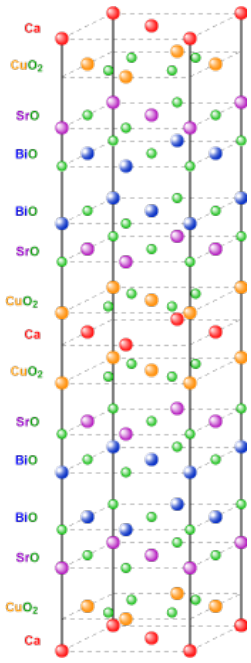

Figure 1: Unit cell of $Bi2212$

The properties of cuprates depend strongly on the temperature, pressure they are and on the doping of the sample[1]. Our interest will be in exploring the properties of Yttrium substituted $Bi_2Sr_2Ca_{0.92}Cu_2O_{\delta+8}$ (also called $Y-Bi2212$ o $Y-BSCCO$) along the doping (in particular hole-doping) and temperature axis. Due to the strong correlations present, the phase diagram of cuprates has many different regions with exotic properties (figure 2) of unclear origin [6]. We will only focus on a few of them, the most relevant to our experiments.

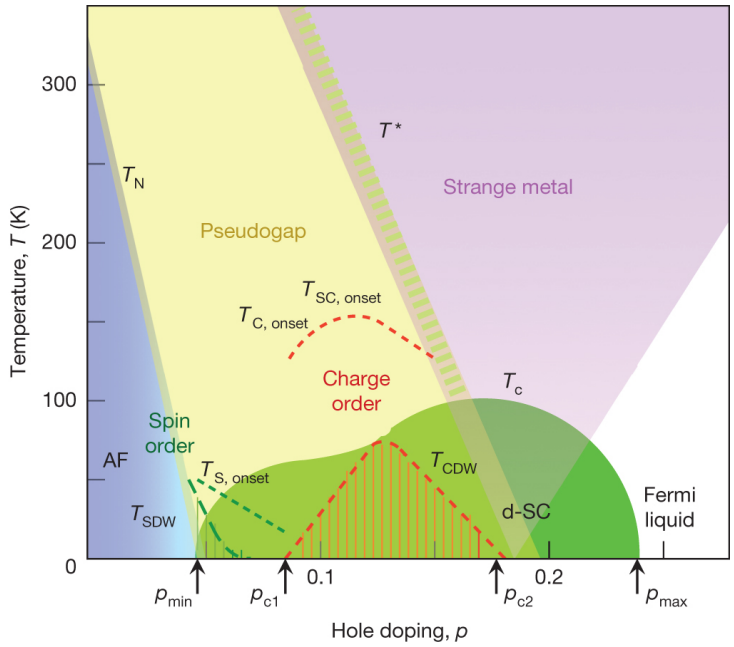

Figure 2: Typical phase diagram of cuprates, taken from [6].

[1]We define doping (p) the concentration of carriers (electrons/holes) in the system obtained by the addition/substitution of chemical elements.

- Pristine cuprates are *Mott insulators*, since the band structure of the material predicts a metallic behavior (the *Cu* sites present an odd number of electrons), but due to the strong electron-electron repulsion that does not allow for doubly-occupied sites. An interesting property of the low-doping region of the phase diagram is that it presents an antiferromagnetic long range ordering due to virtual charge fluctuations generate super-exchange interaction involving *Cu-O-Cu* atoms. The presence of this phase may indicate the involvement of spin fluctuations in the origin of HTSC.

- By increasing the doping p the antiferromagnetic ordering disappears and we enter in the region of the superconducting phase at low temperatures, for each doping there is a critical temperature $T_c(p)$, that increases to a maximum (called *optimal doping*, at $p \sim 0.16$) and then goes back to zero: for this reason this is called the *superconducting dome*. Like in BCS theory the onset of the superconducting phase is characterized by the opening of an electronic gap Δ, but in this case the symmetry of the gap is *d-wave* and not *s-wave*, so there is a dependence on the direction of the momentum $\mathbf{k}$ in the Brillouin zone (see 1.1.4).

- Above the underdoped region (and a little of the overdoped) of the SC dome there is a peculiar phase called *pseudogap*. It endures up to a temperature $T^*(p)$, and while the material is in this state, it presents properties that do not allow it to be defined as a metal or a superconductor: resistivity, specific heat, optical conductivity and the appearance of an electronic gap. There is still a debate if this phase is in competition with superconductivity or is actually a precursor of it with the presence of Cooper pairs that lack phase coherence. This same region contains local orderings of different nature (e.g. short-range Charge Density Wave) and its boundaries are probably the most discussed [7].

- At temperatures above T^* cuprates have another singular phase which is of *strange metallicity* or *normal phase*[2], metallic but with strong correlation effects that differ from the predictions of *Fermi liquid theory*. One example of these properties is the anomalous linear dependence of the resistivity from the temperature and an anomalous charge carrying behavior [8].

- At higher doping the materials go back to a normal metallic state (Fermi liquid behavior).

The presence of other orders hints at what could be the interaction from which superconductivity emerges, such as charge and spin orders. Studies of the underdoped region, which is the richest of this phenomena, have pointed to the possible link between the establishment of a charge order and the emergence of phase coherence [9].

1.1.2 Electronic structure

Pristine cuprates show macroscopic properties that depend mostly on the layers of copper oxides that compose them, while the buffer layers that separate them are electrically inert. The strong electronegativity of the Oxygen atoms deprives each Copper atom of 2 electrons, leaving it with a hole with $d_{x^2-y^2}$ symmetry (figure 3). The strong localization of the states formed makes it very energetically costly (the Hubbard U energy represents this repulsion) to move an electron from a site to another, making the material a Mott insulator[3].

[2] We will refer to this phase this way throughout the text.

[3] The spin of the electron remains a degree of freedom and the virtual hopping of these electrons produces, via the Pauli exclusion principle, an antiferromagnetic interaction between neighboring spins [6].

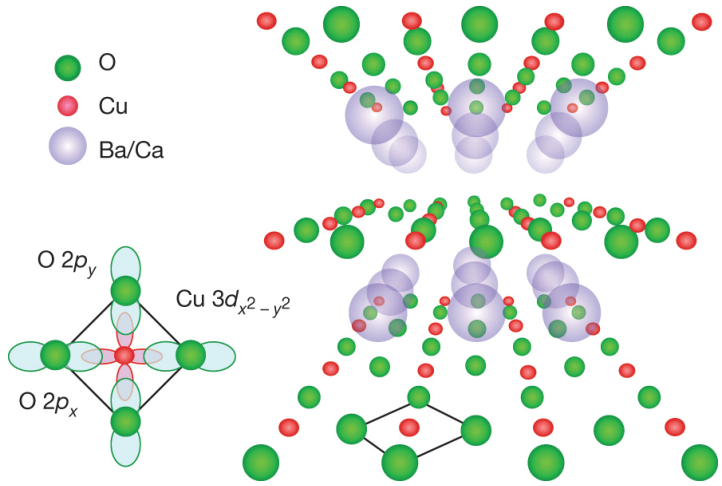

Figure 3: Layered structure of the CuO_2 planes separated by insulating layers in cuprates and associated orbitals. In particular, the electronic structure shown involves the hybridisation of of a $3d_{x^2-y^2}$ hole on the copper sites with planar-coordinated $2p_x$ and $2p_y$ oxygen orbitals. taken from [6].

The repulsion causes the splitting of the *Cu d-band* in a full lower (LHB) and an empty upper Hubbard band (UHB), separated by an energy $U \sim 8 - 10\,\text{eV}$. The O *2p* is $\sim 2\,\text{eV}$ below the UHB, and the transition between the two represents the charge-transfer of the aforementioned $3d_{x^2-y^2}$ hole to the $2p_{x,y}$ states. This gives origin to a charge-transfer gap in the density of states, that sets a lower bound to the electron-hole continuum [10].

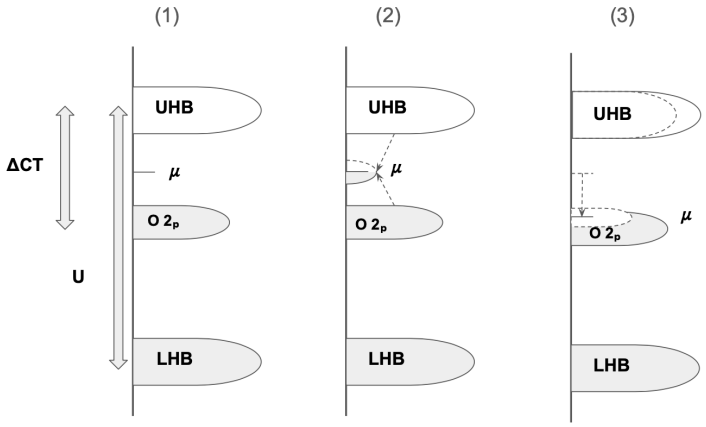

Figure 4: Schematic representation of the possible effects of doping the parent compound (1): the chemical potential μ is pinned and states move toward it (2) or it shifts toward the top of the valence band (LHB in this case), causing a transfer of spectral weight through electronic correlations (3).

The result of hole doping the material is to fill the charge-transfer gap with transitions caused by the introduced itinerant carriers [11]. This could cause either only the creation of in-gap states (Figure 4 (2)) or the linear shift of the chemical potential to lower energies (Figure 4 (3)). In BSCCO the behavior seems to be something in between: the chemical potential does not seem to move much for a doping $< p \sim 0.05$, but it then starts to shift rapidly; this is quite different from LSCO, where the "pinning" of the chemical potential survives until optimal doping [12].

1.1.3 Optical properties and spectral weight transfer

The optical properties of cuprates depend on the discussed electronic structure, and even though there are some differences across this family of High T_c superconductors, the main features are shared. In particular, reflectivity measurements show two different behaviors at low and high energies, with the border set by the dressed plasma frequency ω_p[4]:

- At low energies the signal is dominated by zero-frequency Drude response of the free carriers and mid-infrared excitations possibly related to transition of states close to Fermi energy and the Hubbard bands [13].
- At high energies the signal is similar to charge transfer absorption edge ($E > 2.5\,\text{eV}$).

The excitations in the $1.25 - 2\,\text{eV}$ energy range, which will be the one that we will investigate in this thesis, still are not clear in their origin, which could be found in Cu-O mixed band and states transition or, as suggested by resonant inelastic x-ray scattering (RIXS), by *dd* orbital transitions [14].

The conservation of charge carriers in a material gives us a further constraint on the optical conductivity, which is called the *frequency-sum rule*, that must be true at every temperature:

$$\int_0^\infty \sigma(\omega)d\omega = \frac{\pi n e^2}{2m} = A, \tag{1}$$

where $\sigma(\omega)$ is the real part of the optical conductivity, n, e and m are the electronic density, charge and mass respectively. We now define the low and high-energy spectral weight in the normal state, A_N and B_N. When the material transitions to a superconductive state the existence of perfectly conducting charge carriers must be included[5] and further spectral weight D must be considered. At this point the more general Ferrel-Tinkham-Glover [15] conservation rule holds:

$$D = A_N - A_{SC} + B_N - B_{SC} \tag{2}$$

In BCS superconductors the opening of the gap causes a rearrangement of the excitation spectrum in a range comparable to 2Δ, thus affecting only the low energy spectral weight ($B_N = B_{SC}$). In cuprates the situation is different, as it has been observed that redistribution of the spectral weight happens also at much higher energies. Through spectroscopic ellipsometry it has been observed in BSSCO that there is a redistribution of spectral weight at energies orders of magnitude greater than the gap [16].

1.1.4 Superconducting gap

Like mentioned before, the superconducting gap of HTSC presents a strong anisotropic gap with *d-wave symmetry*: the value of the gap changes depending on the considered direction in the Brillouin zone, with regions that present a maximal value (antinodes, along the ΓX direction, see figure 5) which changes sign after a 90° rotation and regions were the gap goes to zero (nodes, along the ΓM direction, see figure 5). As a direct consequence, the energy required to break a Cooper pair into two quasiparticles changes across the BZ and since it is zero in the nodal regions there is a QP population that dominates the equilibrium response of the material, even at temperatures close to 0 K. Importantly, relaxation dynamics and non-thermal response of antinodal excitations can be addressed with an out-of-equilibrium approach [13].

[4] i.e. the frequency at which the real part of the dielectric function goes to zero.
[5] In the optical conductivity this will result as a real δ-like component at zero frequency.

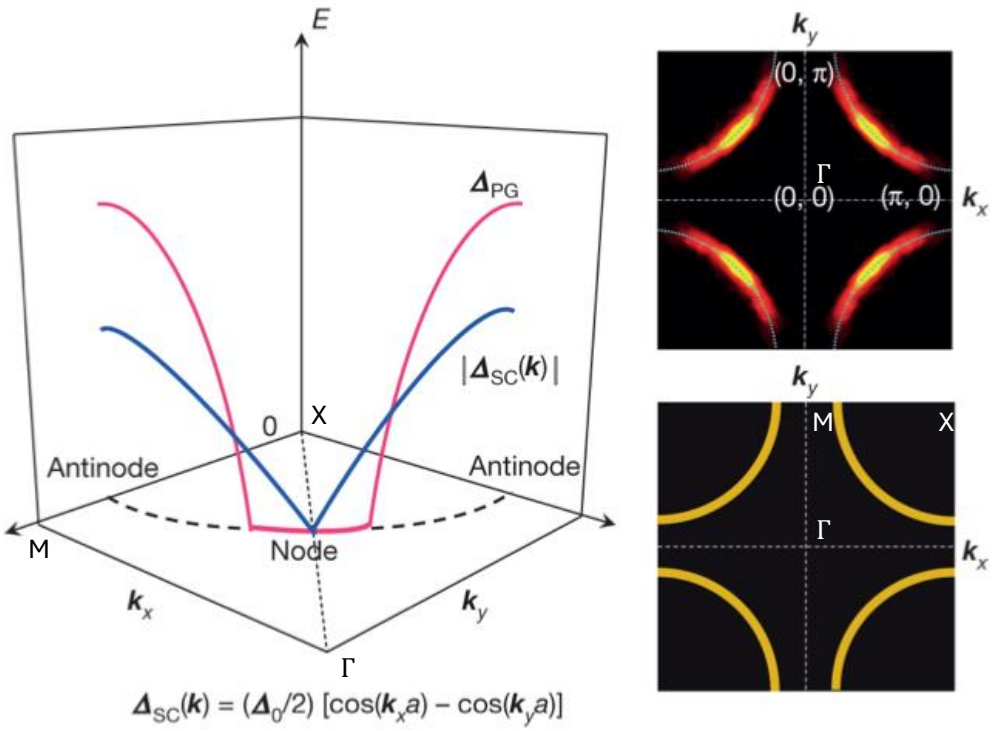

Figure 5: On the left, the anisotropy of the superconducting gap (light blue) and pseudogap (pink) in the Brillouin Zone of cuprates. Bottom right, the large Fermi surface predicted by band theory and confirmed by ARPES experiments [17]. Top right, the Fermi arcs that emerge below T^* [18]. Taken from [6].

1.2 Nonlinear spectroscopy

We introduced the subject of our study, it is now important to introduce the main concepts behind our tools of investigation. Nonlinear measurements provide information on a material through higher-order interactions induced by high intensity fields. One of the main types of experiments in this context is *pump-probe*, which allows the study of the ultrafast dynamics of the system after a nonlinear excitation pulse; in the resulting time-resolved signal it is possible to isolate the timescales of the different excitations involved in the current phase of the material.

1.2.1 Concepts of nonlinear optics

The interaction of an electric field $E(t)$ with a material can be modeled by considering the displacement of the electrons from their equilibrium positions $r(t)$, resulting in a dipole moment $\mu(t) = -e\,r(t)$, with e the charge of an electron. Adding up all the N electric dipoles in a unit volume will give us its macroscopic polarization

$$\mathbf{P}(t) = N\boldsymbol{\mu}(t), \tag{3}$$

that in terms of electric field and susceptibility of the material χ (that encloses the sample contribution to the optical response of the material[6]) becomes

$$\mathbf{P}(t) = \varepsilon_0 \int \chi(t-t')\mathbf{E}(t')dt', \text{ or its transform in the frequency domain } \mathbf{P}(\omega) = \varepsilon_0\chi(\omega)\mathbf{E}(\omega), \tag{4}$$

where ε_0 is the dielectric permittivity of vacuum. A field that is weak with respect to the attraction between nuclei and electrons allows us to approximate the interaction as an harmonic

[6]The susceptibility has been simplified to only have time dependence, which is true for homogeneous materials.

perturbation and the dependence between field and polarization is linear, like it is shown in the last equation. But for high-intensity fields, such as the ones produced by lasers, anharmonicity effects emerge and an expansion of the polarization to higher orders of the electric field is needed:

$$P = P_L + P_{NL} = \varepsilon_0[\chi^{(1)}E + \chi^{(2)}E^2 + \chi^{(3)}E^3 + \dots]. \tag{5}$$

Equation 5 is the most direct approximation to the more complete expression of P, since we reduced the vectorial nature of E and tensorial[7] nature of $\chi^{(n)}$ to a scalar model.

The nonlinear processes that the different orders of the polarization give origin to are fundamental to the technological apparatus for nonlinear spectroscopy (see 9) and to describe the field's interaction with the material. Symmetry considerations of the system allow us to put further constraints: for centrosymmetric structures all the even-order susceptibilities vanish, having $\chi^{(3)}$ as their lowest nonlinear order.

In the framework of light-matter interaction, the third order susceptibility tensor mediates the 'four wave mixing' process, i.e. a phenomenon in which the interaction of three different fields generates of signal field, according to the energy and momentum conservation laws. This is the picture in we study Pump-Probe processes, as the interaction of the intense pump pulse and the probe pulse (the former accounts for two of the four fields, or from quantum point of view, two photons) to produce the signal field E_s. By assuming the pump photons to have equal and opposite momentum $\mathbf{k_{p1}} = -\mathbf{k_{p2}}$ by momentum-conservation we will have the same direction for probe and signal:

$$\mathbf{k_{p1}} + \mathbf{k_{p2}} + \mathbf{k_{probe}} = \mathbf{k_s}\,. \tag{6}$$

The signal field has a very weak intensity and would be very difficult to detect, but due the presence of the co-propagating probe pulse the signal is amplified by the interferometric effect called *heterodyne process*, so the detected intensity reads as

$$I(t) = \frac{n(\omega_s)c}{4\pi}|E_s(t) + E_{Probe}(t)|^2 = I_s(t) + I_{Probe}(t) + \underbrace{\frac{n(\omega_s)c}{2\pi}\Re(E_s^*(t)E_{probe}(t))}, \tag{7}$$

and we can isolate the signal from the last term. In general the heterodyne process is obtained by adding an external beam, called *local oscillator*. Pump-Probe measurements are a specific case in which the probe itself acts as a local oscillator, so the process is said to be *self-heterodyned*.

1.2.2 Theoretical introduction to Pump-Probe measurements

The characterization of complex materials often requires approaches that extend beyond linear response techniques, since the interplay among multiple degrees of freedom cannot be fully captured within this framework [13]. Nonlinear spectroscopic methods, such as pump–probe spectroscopy, provide a powerful means to disentangle these interactions. In a pump–probe experiment, the material is exposed to two ultrashort light pulses. The first pulse, referred to as the *pump*, excites the system, while the second pulse, the *probe*, interrogates the system after a controlled delay time Δt (figure 6). By analyzing the probe signal-either in reflection or transmission-it is possible to reconstruct the material's dynamical response.

[7] The $n-th$ order susceptibility would be a tensor of rank $(n+1)$.

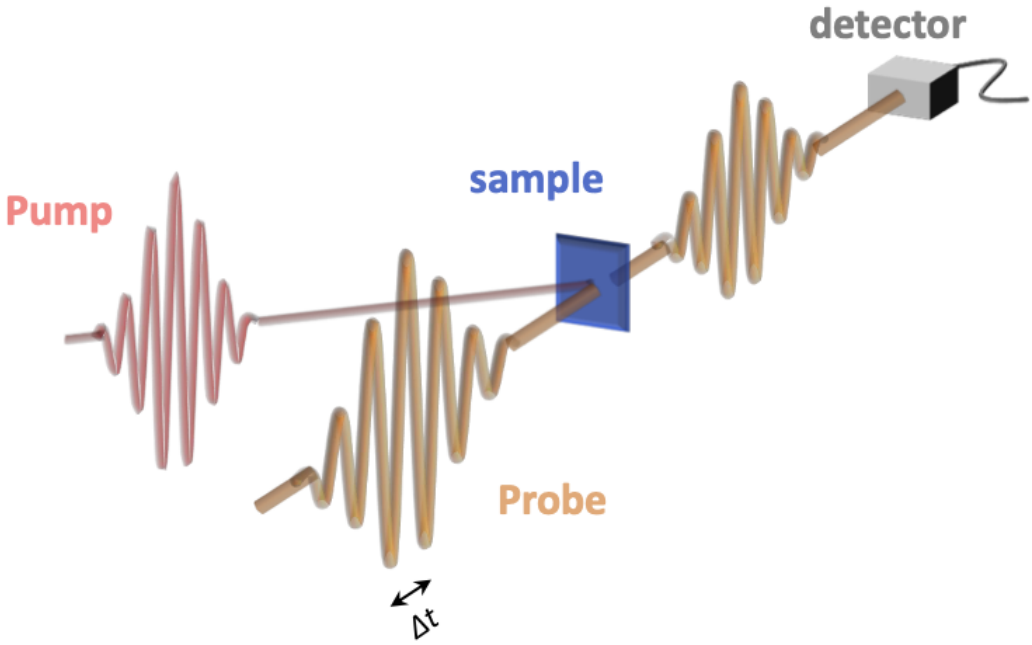

Figure 6: Sketch of a Pump-Probe experiment in transmission configuration. Taken from [19].

The time-resolved study of the probe intensity allows the observation of the characteristic timescales of different interaction processes, such as the ones of the field with the electrons (EM-e), electron-electron interaction (e-e), interactions with the lattice (e-L) and the following thermalization of the lattice. A typical pump-probe trace, illustrating in a simple way these scales, is represented in figure 7.

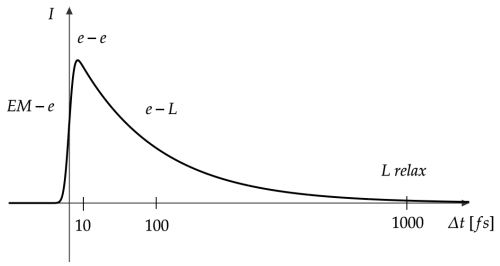

Figure 7: Sketched example of pump-probe intensity trace. Adapted from [20].

1.3 Non-equilibrium measurements of cuprates

Having established the main properties of a cuprate superconductor and the basics of time-resolved Pump-Probe measurements, we can now discuss the results of the non-equilibrium approach on these exotic materials.

1.3.1 Superconductors non-equilibrium dynamics

The model that is most commonly used to describe non-equilibrium dynamics after the interaction of a pump pulse with a superconductor is based on a phenomenological take by Rothwarf and Taylor (therefore called Rothwarf-Taylor model [21]). The model was developed from the

theory and observations made for BCS superconductors, but describes quite well cuprate's dynamics too; the main hypotheses here are:

- The presence of a superconducting gap Δ.
- The emission and absorption of bosons coupling to pair dynamics.

While there are obvious differences for HTSC, given the anisotropy of the superconducting gap, the presence of the pseudogap and the difference in the coupling channel[8], the mechanism of the *bottleneck regime* the model describes remains valid. The model can be split in three steps.

1. A Cooper pair splits due to the pump's excitation, creating quasiparticles at higher energies (Figure 8, 1).
2. The quasiparticles recombine into Cooper pairs emitting a phonon $E_{ph} \geq 2\Delta$ (Figure 8, 2).
3. The emitted phonon has enough energy to break another Cooper pair, and so on (Figure 8, 3).

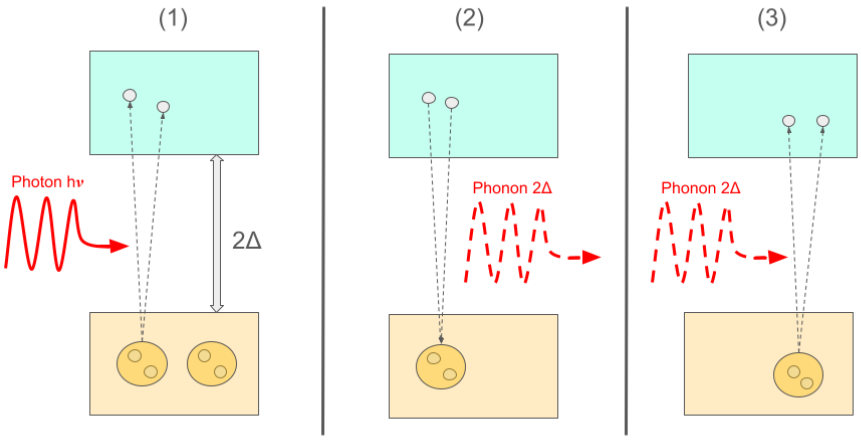

Figure 8: Schematic representation of the Rothwarf-Taylor model.

The recovery dynamics of the condensate is therefore linked to the phonon lifetime: the longer the lifetime, the higher the probability of interacting and breaking a Cooper pair, slowing down the recovery dynamics. The balance between creation of quasiparticles and phonons puts a limit to this slowdown, causing the aforementioned bottleneck regime. The equations that describe this phenomenological model are:

$$\frac{\partial n}{\partial t} = I_{qp}(t) + \eta p - \beta n^2 \tag{8}$$

$$\frac{\partial p}{\partial t} = I_p(t) - \frac{\eta p}{2} + \frac{\beta n^2}{2} - \gamma(p - p_T), \tag{9}$$

where n and p are respectively the number of quasiparticles and phonons in the system, I_{qp} and I_p are the the number of injected quasiparticle/phonons (in this case I_p should be negligible). The transition probability for pair breaking due to phonon absorption is represented by η, while

[8] In the following explanation I will often use phonons to be coherent with the original model, but as already explained these bosons are not the mediators of electronic pairing in HTSC.

βn is rate of quasiparticle recombination. The other phonon decay mechanisms are represented by the term in γ, that contains the equilibrium population of phonons at temperature T, p_T. It is quite straightforward to see that $\gamma \ll \eta$.

Some anomalous behaviors emerges when the density of excitations is increased as an intense pulse can cause an ultrafast response to be superimposed to the slower recovery dynamics [22].Other studies have showed that SC state can be transiently melted without affecting the pairing strength (and thus without breaking the Cooper pairs) by addressing and destroying the long-range coherence of the condensate [23].

1.3.2 Sub-gap excitations

In the presence of a gapped system the distribution of quasiparticles at equilibrium affects the value of the energy gap [13], [15]; modifying the quasiparticle distribution can enhance the gap and allow to have a superconducting state at $T \geq T_c$, it is important though not to change the number of quasiparticles and therefore one must not split Cooper pairs and this calls for the use of sub-gap excitations. A sub-gap pulse does not have enough energy to split a Cooper pair but it can promote thermal quasiparticles in the low-lying states at $\Delta \leq E_k \leq \Delta + \hbar\omega$, to the less populate states at energies $E_k \geq \Delta + \hbar\omega$: the intuitive result is an increase in the states at $E_k \geq \Delta$ that are available for the formation of the condensate (thus increasing the value of the gap). Due to the anisotropic nature of the gap in non-conventional superconductors it is difficult to extend such processes to them, as the nodal regions will cause the breaking of pairs for some $\mathbf{k}$ value. Nevertheless, the experiments that were done on HTSC have shown that even in these materials transient superconducting states can be photo-induced ([24–26]), even though the origin of this phenomenon is still unclear. Our studies will focus to resonant sub-gap excitations optical excitations ($\hbar\omega \leq 2\Delta(T)$).

1.4 Experimental setup

In this section, we explain the general aspects of the setup that was used in all of the measurements of the thesis, leaving the specifics to the relative chapters. The objective is to do pump-probe measurements to study the dynamics of BSCCO electronic modes in the energy region $1.2 - 2.5\,\text{eV}$ under sub-gap excitation in the superconducting states and to obtain time-resolved Raman measurements in this same region. To do so we need an impulsed laser source and a setup capable of producing the frequencies for pump and probe beams. To be able to isolate modes relative to different regions of the Brillouin zone we will also need to discriminate two different polarizations of the probe in the detection (the theoretical reason can be found in Section 2, at 2.1).

The fundamental frequency of the setup is provided by a 1030 nm Ti-Sapphire laser source (Pharos, Light Conversion). The coherent pulses ($400\,\mu\text{J}$, $50\,\text{kHz}$) emitted by the laser source are used to generate three different beams through nonlinear optical processes:

1. Broadband white-light beam ($550 - 950\,\text{nm}$).
2. Visible/near-IR beam ($650 - 900\,\text{nm}$).
3. MIR beam ($4.5 - 18\,\mu\text{m}$).

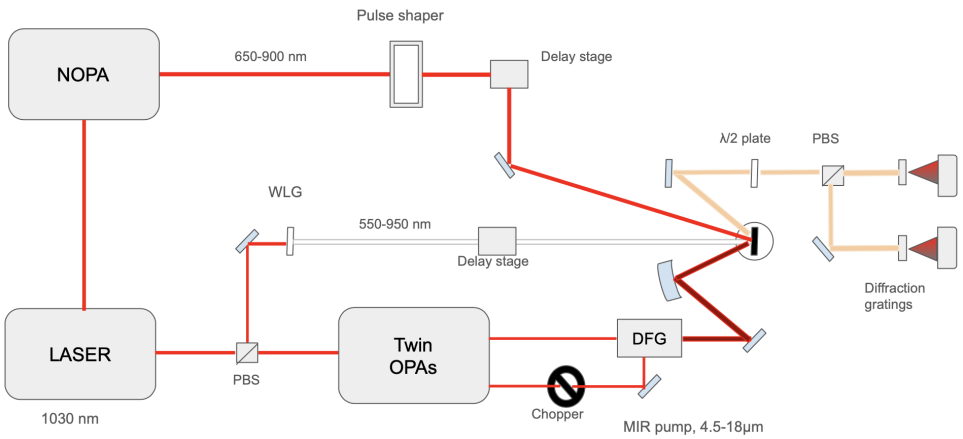

Figure 9: Sketch of the experimental setup used in all of the measurements of this thesis.

White light generation

To generate the "white light" beam $10\,\mu$J of the 1030 nm laser are filtered and focused in a 6 mm thick sapphire crystal (Al_2O_3), in which third order phenomena of self phase modulation and self focusing produce the broadband supercontinuum. The $550 - 950$ nm ($1.3 - 2.25$ eV) spectrum is shown in figure 10, where it can be seen that at high wavelengths the signal is truncated due to the presence of a filter that prevents the fundamental frequency from entering the detection.

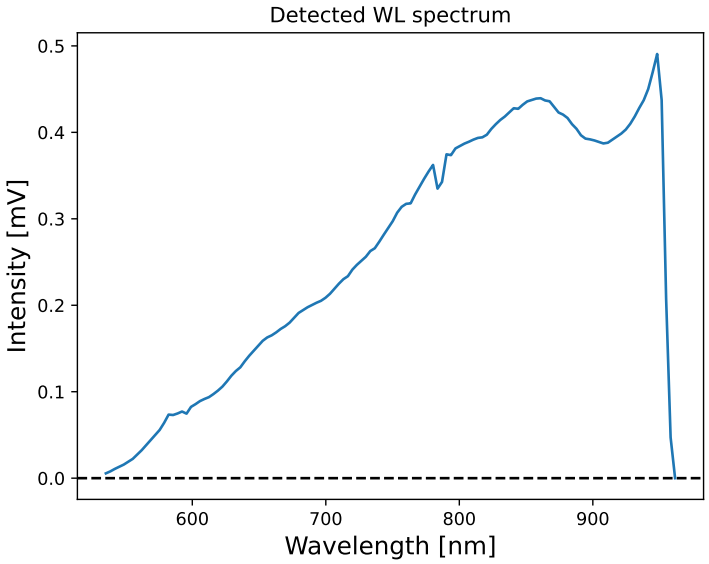

Figure 10: Average detected white-light supercontinuum probe signal.

The produced pulses are positively chirped (i.e. the low frequencies arrive first) determining an elongated temporal profile ($<$ 1 ps). These pulses are used as a probe to measure the broadband optical response of the material.

Visible/near-IR

$40\,\mu$J of the 1030 nm laser are sent to a Non-Collinear Optical Parametric Amplifier (Orpheus-N, Light Conversion) to generate ultra-short ($<$ 25 fs) pulses at wavelengths tunable in the range $650 - 900$ nm, which as explained before in 1.1.3 sits in the region coupled to the low energy excitations, and will be thus used as a probe.

MIR

The remaining 350 μJ of the emitted fundamental laser are used in the pump-pulse generation through a Twin Optical Parametric Amplifier system (Orpheus-TWIN, Light Conversion). The two output beams are then used to produce the final beam through Difference Frequency Generation (DFG) in a GaSe crystal, which is filtered to remove wavelengths shorter than 4μ m; the range of tunability of the resulting pump is $4.5 - 18\,\mu$m and its temporal duration is > 100 fs.

Sample and cryostat

The three beams described in the previous section are redirected and focused onto the sample, which is mounted into a closed-loop helium cryostat. By ensuring that the sample is in thermal contact with the cold finger of the closed cycle liquid helium cryostat (DE 204, *Advanced Research Systems*), we can perform measurements at cryogenic temperatures ($8 - 300$ K) and explore different phases of complex materials. The customized mechanical structure on which the cryostat is arranged allows for tridimensional adjustments; to add a rotational degree of freedom a (removable) piezoelectric rotator (*Attocube*, ANR240) is present between sample and holder. The sample holder is kept in vacuum conditions using a turbomolecular pump (*Pfeiffer*, HiCube 80 Eco), with typical pressures of around $10^{-7} - 10^{-8}$ mbar.

The pulses reach the sample through a diamond window and the reflected light travels outside the same window and then to the detection stage; diamond is used because of its broad transparency range and isotropic optical response. The temperature of the sample and of the cold finger are measured with thermocouples mounted on them (for the sample, the thermocouple is very close to it). The presence of the rotator decreases the efficiency of cooling, increasing the minimum temperature reached from 10 K to 40 K.

The four Y-BSCCO samples used in this theses have four different doping: two underdoped samples with $T_c = 88, 91$ K, one optimally doped sample with $T_c = 95$ K and an overdoped sample, with $T_c = 91$ K; they will respectively be called UD88, UD91, OP95 and OD91.

Detection

The reflection from the sample is guided using mirrors to the detection stage; using a $\lambda/2$ waveplate and a Polarizing Beam Splitter (PBS) we can separate the contributions of the different polarizations. Each beam is then dispersed in its different spectral components with a transmission grating (see figure 9) and then focused on a NMOS detector, constituted by an array of 128 silicon photodiodes (Hamamatsu, S8380-128Q). The detectors are synchronized with the laser source and allow single-shot acquisition up to 5 kHz [9]. The information recorded for every acquisition is the voltage generated at each pixel (photodiode), which must be converted to frequency information through an accurate calibration.

For the white-light probe the frequency calibration is obtained directly using a commercial bandpass filter (FGB67, Thorlabs) with a characterized transmission spectrum: the transmitted frequencies are associated to the pixel they impinge on and the remaining ones are interpolated.

The other probe is calibrated by using a Spatial Light Modulator (SLM), a programmable liquid-crystal based device which is at the core of our pulse shaping apparatus. The pulse shaper itself is characterized in its response every time the setup is realigned; the calibration procedures and the working principle of this optical component are described in 4.2.3.

Differential acquisition

The objective of pump and probe experiments is to study the differential signal associated to the pump-induced excitation, so one must obtain both the excited signal and the one at

[9] Beyond such repetition rates the signal is integrated over the different pulses.

equilibrium. To sort the signal in *unpumped* and *pumped* pulses a chopper is placed to stop the pump at a chosen frequency. The maps that will be shown for the birefringence measurements will therefore be *differential reflectivity* maps, expressed as a function of the detection frequency ω and the Pump-Probe delay time Δt:

$$\frac{\Delta R(\omega, \Delta t)}{R} = \frac{R_{pumped}(\omega, \Delta t) - R_{unpumped}(\omega, \Delta t)}{R_{unpumped}(\omega, \Delta t)} \tag{10}$$

The Pump-Probe delay time Δt is controlled through the delay stage, which increases the optical path of the probe pulse.

2 White-light birefringence measurements of BSCCO

Measurements using a supercontinuum probe on cuprates have been already made in the past [27], allowing the observation of the broadband optical response of the material, and the selective probing of electronic modes through birefringence has started to be considered after the paper of *Giusti et al.* [28]. In this project we combine the two ideas for the first time. In the present section we will examine dynamic birefringence measurements of B_{1g} and B_{2g} electronic modes of $Y - Bi_2Sr_2Y_{0.08}Ca_{0.92}Cu_2O_{\delta+8}$ samples for four different doping levels in the three different phases. This Pump-Probe experiment uses $17\,\mu$m pump and the white-light probe, covering a broad band of excitation in the visible and near-infrared ($1.3 - 2\,$eV). The mode isolation will allow us to probe the anisotropic properties of cuprates and the use of the supercontinuum probe will allow us to see these dynamics on a broadband spectrum in the region where high and low energy excitations are coupled (see 1.1.3).

In the first part of this section we will introduce the selection rules and models that are used to isolate the two electronic modes through birefringence. In the second part we will introduce how our data is processed and the maps for reflectivity signal of a single polarization, for a first characterization of the optical response of the samples across the different phases and as a function of temperature. In the same way we are then going to characterize the response of the two modes.

2.1 Theoretical introduction on the measurements

One of the common grounds in the theoretical understanding of High-T_c superconductors is that they present a *d-wave* symmetry. By using the crystal symmetry of BSCCO it is possible to isolate electronic excitations in different zones of the Brillouin zone and therefore to perform a momentum-resolved investigation of the anisotropic properties of cuprates. To understand our approach we will first introduce a quantum model for Raman scattering and the theoretical picture in which we isolate the B_{1g} and B_{2g} electronic modes.

Quantum model for Raman scattering

Raman scattering is an effect that, since its discovery [29], has been a staple in the world of spectroscopy, allowing for analysis of samples in all branches of science. Light matter interaction results most of the time in the elastic scattering of it, but some of it is absorbed and re-emitted at a different energy: the energy difference in this inelastic scattering phenomenon is a trace of the elementary excitations that exist in solids, such as phonons, plasmons, excitons and spin fluctuations [30]. The process can be reduced to three steps:

1. The material couples to an external electromagnetic field: the absorption of a photon gives origin to an electron-hole pair (virtual intermediate level).

2. The pair transitions to another state, creating an elementary excitation.

3. The pair recombines, producing a photon: this is what can be measured during an experiment.

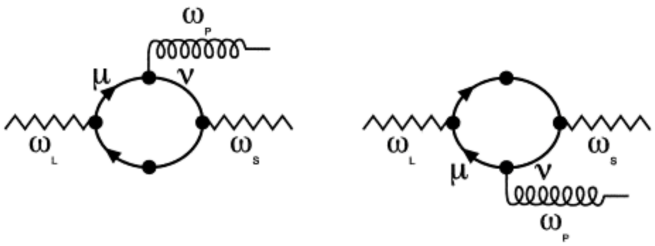

Figure 11: Description of Raman process through Feynman diagrams: on the left, an photon with frequency ω_L interacts with an electron to create an intermediate virtual state μ, which emits a phonon at frequency ω_P to transition to a level ν. The recombination finally produces a scattered phonon at frequency ω_S. On the right the analogous process for a photon-hole excitation. Taken from [31].

Depending on the band structure of the material, these excitations can be excited directly or through the mediation of electrons [32]. The structure of the material also creates a constraint on the allowed excitation modes.

There are classical phenomenological interpretations of Raman scattering that grasp the main aspects of it, but the effects are purely quantum mechanical and thus need a quantum mechanical model.

The model we will follow develops from second-order perturbation theory. We will consider the Hamiltonian for a system of N electrons of mass m and charge e in a electromagnetic field, where the perturbation is given by the field's vector potential $\hat{A}$:

$$H = \sum_i^N \frac{1}{2m}(\hat{p}_i + \frac{e}{c}\hat{A}(r_i))^2 + H_{Coulomb} + H_{field} \ , \tag{11}$$

where $\hat{p}_i$ and r_i are the momentum operator and the coordinates (spatial and temporal) of the i^{th} particle, put together in what we call the *kinetic term*. The two other Hamiltonians in the expression represent the Coulomb interactions between the electrons and the free electromagnetic field. Expanding the kinetic term we obtain

$$H = \tilde{H} + \frac{e}{emc}\sum_i^N (\hat{p}_i\hat{A}(r_i) + \hat{A}(r_i)\hat{p}_i)^2 + \frac{e^2}{2mc^2}\sum_i^N \hat{A}(r_i)\hat{A}(r_i) \equiv \tilde{H} + H'_{INT} + H''_{INT} \tag{12}$$

where we define

$$H = \tilde{H} = \frac{1}{2m}\sum_i^N \hat{p_i}^2 + H_C + H_F$$

In electronic Raman scattering experiments, we measure the total cross section (or rather the *scattering efficiency*) of all the electrons illuminated by the incident pulses. Theoretically we can derive the probability of a photon of frequency ω_i and polarization $\mathbf{e}_i$ to be scattered within a solid angle range $(\Omega, \Omega + d\Omega)$ in a frequency range $(\omega_s, \omega_s + d\omega_s)$ (i.e. the differential cross section of the process) from Fermi's Golden Rule:

$$\frac{\partial^2\sigma}{\partial\Omega\partial\omega_s} \propto \frac{\omega_s}{\omega_i}\frac{1}{\mathcal{Z}}\sum_{I,F} e^{-\frac{E_I}{k_B T}}|M_{F,I}|^2\delta(E_F - E_I - \hbar(\omega_i - \omega_s)), \tag{13}$$

where k_B is Boltzmann's constant, $\mathcal{Z}$ is the partition function, I and F indicate the initial and final states and $M_{F,I}$ is the matrix element of the effective light-scattering operator up to the second order perturbation-theory:

$$M_{F,I} = \langle F|H'_{INT} + H''_{INT}|I\rangle \ ,$$

this part of the equation is what determines the selection rules for the polarization, while the Dirac's delta ensures the Energy conservation. To calculate $M_{F,I}$ we use second-quantization formalism for the electronic states [30]:

$$M_{F,I} = \mathbf{e}_i \cdot \mathbf{e}_s \sum_{\alpha,\beta} \rho(\mathbf{q}_i - \mathbf{q}_s) \tag{14}$$

where c_γ and $c_\gamma^\dagger$ are the annihilation and creation operators of the electronic states, while $\rho_{\gamma,\gamma'}(\mathbf{q})$[10] is the matrix element for single-particle density fluctuations and $p_{\gamma,\gamma'}$ is the momentum density matrix element

Selection rules and models

The aforementioned expression results greatly simplified by taking into consideration the constraint given by the crystal structure. The selection rules for Raman scattering are easily accessible through the Raman tensor R since $M_{FI} = \langle F|R|I\rangle$, and R can be decomposed in the basis of the irreducible representation of the symmetry group $\{\phi_\alpha\}$:

$$R = \sum_\alpha R_\alpha \phi_\alpha. \tag{15}$$

Most of the cuprates can be described by a D_{4h} tetragonal point group and have inversion centers, this last information allows us to split the excited modes in even (g, gerade) and odd (u, ungerade) under the inversion operation. The u modes are IR-active, while the g mode are Raman active and will be our only concern in the calculations:

$$A_{1g}^{(1)} \to \begin{pmatrix} a & & \\ & a & \\ & & \end{pmatrix} \quad A_{1g}^{(2)} \to \begin{pmatrix} & & \\ & & \\ & & b \end{pmatrix} \quad B_{1g} \to \begin{pmatrix} c & & \\ & -c & \\ & & \end{pmatrix} \quad B_{2g} \to \begin{pmatrix} & d & \\ d & & \\ & & \end{pmatrix}$$

$$A_{2g} \to \begin{pmatrix} & d & \\ -d & & \\ & & \end{pmatrix} \quad E_g^{(1)} \to \begin{pmatrix} & & e \\ & & \\ e & & \end{pmatrix} \quad E_g^{(2)} \to \begin{pmatrix} & & \\ & & e \\ & e & \end{pmatrix}$$

we can select a specific projection of the Raman tensor by having control on the polarization of the incoming and scattered light, and a single projection will contain a few of these modes. The configuration we will focus on is the one that we employ in the experiments: the pulses will impinge on the sample parallel to its $\hat{c}$ axis, i.e. perpendicular to the CuO_2 planes, with a resulting Raman tensor

$$R = \frac{1}{2}\begin{pmatrix} R_{A_{1g}} + R_{B_{1g}} & R_{B_{2g}} \\ R_{B_{2g}} & R_{A_{1g}} - R_{B_{1g}} \end{pmatrix}. \tag{16}$$

In equation 16 there is no contribution from the A_{2g} mode because it only becomes relevant for circular polarization of light [32].

By now considering the representative basis functions $\phi_\alpha(k)$ from the complete set of Brillouin-zone (BZ) harmonics of the D_{4h} group [33] we make manifest the possibility of making momentum-resolved measurements of the excitations through polarization control in Raman scattering:

$$\begin{aligned} A_{1g} &\to \frac{1}{2}(\cos(k_x a) + \cos(k_y a)) \\ B_{1g} &\to \frac{1}{2}(\cos(k_x a) - \cos(k_y a)) \\ B_{2g} &\to \sin(k_x a)\sin(k_y a) \end{aligned} \tag{17}$$

[10] Where $\rho_{\gamma,\gamma'}(\mathbf{q}) = \sum_i \langle\gamma|e^{i\mathbf{q}\cdot\mathbf{r}}|\gamma'\rangle$.

The A_{1g} mode is total-symmetric, while the other two modes are strongly anisotropic in the BZ, in particular the B_{1g} is maximum along the ΓM direction and B_{2g} is maximum along the ΓX direction (see figure 12). Remembering the anisotropy of the d-wave gap in the superconductor, we will say that the B_{1g} probes anti-nodal excitations, while B_{2g} probes nodal excitations.

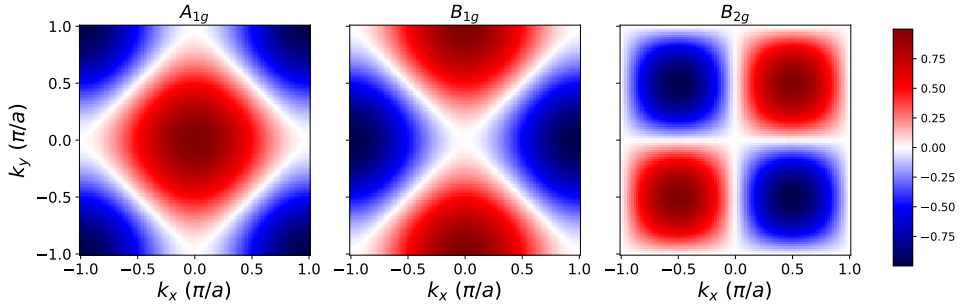

Figure 12: Brillouin zone harmonics for the three electronic modes allowed in the experimental configuration of our experiments.

First order model

Pump and probe experiments are interpreted as a four-wave mixing process, but for spontaneous Raman scattering measurement a simpler static approach can be followed, which describes the experiment through what we call *first order model*. The model does not account for the pump's interaction with the system, so it is fit for equilibrium experiments.

The interaction of the light with the sample is treated through the knowledge of the Jones vector of the incoming probe pulse, the Raman tensor of the system and the Jones vector of the scattered probe pulse:

$$|I\rangle = \begin{pmatrix} \cos(\theta) \\ \sin(\theta) \end{pmatrix} \qquad |F\rangle = \begin{pmatrix} \cos(\alpha) \\ \sin(\alpha) \end{pmatrix} \tag{18}$$

where θ and α are relative to the CuO axis. Computing the matrix element $M_{F,I}$, given 16, returns:

$$M_{F,I} = \langle F|R|I\rangle = (\cos(\alpha),\ \sin(\alpha))\ \frac{1}{2} \begin{pmatrix} R_{A_{1g}} + R_{B_{1g}} & R_{B_{2g}} \\ R_{B_{2g}} & R_{A_{1g}} - R_{B_{1g}} \end{pmatrix} \begin{pmatrix} \cos(\theta) \\ \sin(\theta) \end{pmatrix} \tag{19}$$

$$M_{F,I} = R_{A_{1g}} \cos(\theta - \alpha) + R_{B_{1g}} \cos(\theta + \alpha) + R_{B_{2g}} \sin(\theta + \alpha). \tag{20}$$

The angles θ and α are tunable parameters of the experiment: we can select the polarization of the incoming pulse and of the scattered light that reaches the analyzer through polarizers, beam splitters and $\lambda/2$ waveplates. In our experiments in particular we select two orthogonal projections of the probe pulse, we measure them and then subtract them to obtain the birefringence signal. To isolate the desired modes we choose $\alpha = \theta \pm 45°$, so that the respective contributions to the transient differential reflectivity are

$$\Delta R^{\pm} \propto R_{A_{1g}} \cos(\mp 45°) + R_{B_{1g}} \cos(2\theta \pm \alpha) + R_{B_{2g}} \sin(2\theta \pm \alpha),$$

which results in a birefringence signal

$$\Delta\Delta R = \Delta R^{+} - \Delta R^{-} \propto -R_{B_{1g}} \sin(2\theta) + R_{B_{2g}} \cos(2\theta). \tag{21}$$

Equation 21 shows that for the first order model we can use birefringence measurements to avoid the contribution of the A_{1g} mode and to isolate the B_{1g} and B_{2g} modes by simply selecting the polarization of the incoming probe beam.

Third order model

To introduce the interaction of the pump with the material, which would be rather odd to ignore in a pump and probe experiment, we introduce the formalism of the *third order model*, that considers also the pump polarization.

The pump-probe process must be modeled by expanding the interaction Hamiltonian (equation 12), leading to the definition of the 4^{th} rank Raman Tensor

$$R^{(3)}_{ijkl} = R^{ij}_{A_{1g}} R^{kl}_{A_{1g}} + R^{ij}_{B_{1g}} R^{kl}_{B_{1g}} + R^{ij}_{B_{2g}} R^{kl}_{B_{2g}},$$

Were the i, j, k, l are indices that run on the two axes directions of the copper oxide planes [34]. Remembering the calculations that brought us to equation 16, in this expansion we get

$$R^{(3)}_{ijkl} = \begin{pmatrix} \begin{pmatrix} a^2+c^2 & \\ & a^2-c^2 \end{pmatrix} & \begin{pmatrix} & d^2 \\ d^2 & \end{pmatrix} \\ \begin{pmatrix} & d^2 \\ d^2 & \end{pmatrix} & \begin{pmatrix} a^2-c^2 & \\ & a^2+c^2 \end{pmatrix} \end{pmatrix}$$

where the first two indices are linked to the pump polarization and the last two to the probe and the scattered light (i.e. the signal). Maintaining the notation of the simpler model and adding now the angle ϕ of the pump polarization with respect to the CuO direction

$$\begin{pmatrix} \cos(\phi) & 0 \\ 0 & \cos(\phi) \\ \sin(\phi) & 0 \\ 0 & \sin(\phi) \end{pmatrix}$$

The resulting reflectivity is thus

$$\Delta R \propto A_{1g} \cos(\theta - \alpha) + B_{1g} \cos(\theta - \alpha) \cos(2\phi) + B_{2g} \sin(\theta - \alpha) \sin(2\phi),$$

where we can now put the $\alpha = \theta \pm 45°$ and subtract the two to obtain the birefringence signal:

$$\Delta\Delta R \propto -B_{1g} \sin(2\theta) \cos(2\phi) + B_{2g} \cos(2\theta) \sin(2\phi). \tag{22}$$

The calculated birefringence is analogous to the first order one from the point of view of the removal of the total-symmetric mode, but it shows a different angular dependence due to the new parameter ϕ, that allows the isolation of a single mode by the selection of the pump polarization.

The angular dependence of the model, like the one of the first order model, has been tested in [19], giving rather unexpected results, above all what seems an asymmetric trend; to reach the scope of this thesis we will only explore the configurations that isolate a single mode.

Detection configuration

The calculations of the birefringence contributions lead us to the choice of two possible configurations, shown in figure 13:

- B_{1g} *isolation*: we set the pump polarization parallel to the CuO direction and the probe parallel to the $CuCu$ direction.
- B_{2g} *isolation*: we set the pump polarization parallel to the $CuCu$ direction and the probe parallel to the CuO direction.

Figure 13: Configurations of pump and probe polarizations and detection in the birefringence experiments: on the left the configuration for the B_{1g} mode isolation and on the right for the B_{2g} mode. The green arrows represent the projected polarizations of the probe that are sent to the two detectors. Taken from [19].

To switch from a configuration to the other we rotate the sample by 45° using the rotator mounted on the sample holder.

2.2 Single channel measurements and procedures

The focus of this part of the project is on the birefringence signal that allows us to isolate the B_{1g} and B_{2g} modes, but the information contained in the single channel measurements is still useful as conveys information on the $A_{1g} + B_{1g}/B_{2g}$ modes. Before the birefringence section we thus introduce the data correction and analysis procedures and the resulting single channel maps.

2.2.1 Data analysis and chirp correction

As already mentioned in 9 the pulse obtained through WLG is positively chirped (for the definition of chirp, see the introduction to section 3), which is typical for this kind of experiment. During the analysis of the data a fit of the overlap signal is made, and the signal for every pixel is shifted accordingly, so that every frequency arrives at the same time. This has been a standard procedure in past articles on high temperature superconductors ([27,35]) and it has been shown that the long duration of the probe pulse does not affect the time resolution of the experiment, which remains the one of transform limited pulses [36] (i.e. pulses with the shortest duration allowed by their bandwidth according to the uncertainty principle) as long as the different spectral components are resolved.

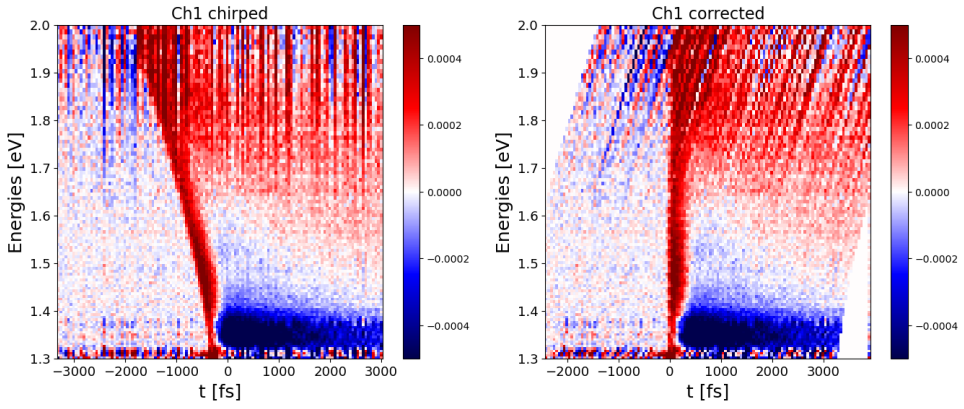

Figure 14: Example of a white-light transient differential reflectivity measurement, before and after the correction of its chirp. The measurement comes from an optimally doped sample of *Y-BSCCO* in SC state, with pump polarization ∥ to the *CuCu* direction

The result of a pump-probe measurement on our setup is shown in figure 14, along with the corrected version: the differential reflectivity signal is shown as a 2D map, function of the energy of the probe pulse (on the y-axis) and the time delay (on the x-axis). The possibility of correcting the data maintaining optimal time resolution overcomes the great technical challenge that would be properly compressing such a broadband pulse, but as we will discuss in section 3 the presence of the chirp might affect the measurement.

2.2.2 Pump fluence

In this section we test the pump fluence dependence on the broadband reflectivity of the sample. This has the double objective of understanding the limits of the "linear"[11] regime in which all of the measurements are done and studying the possible nonlinearities that the high pump intensity could introduce. A disclaimer must be given: the fluences are measured in a way that overestimates the actual amount of energy delivered to the sample, so the shown values have the role of giving a relative intensity estimate, rather than giving a quantitative statement about the phenomena. The birefringence measurements were all taken at 17 μm pump wavelength, but since we will be using the 10 μm for the FCS we have also done a fluence study at this wavelength (not reported in the thesis). The study was done for all of the four samples, but for the sake of conciseness, we will present just the measurements performed on the OP95 sample.

The subgap excitation produces dynamics which are rather similar in the single channel for both the pump orientations, so the following observations and figure will limit only to the one with the pump polarization $\parallel CuO$.

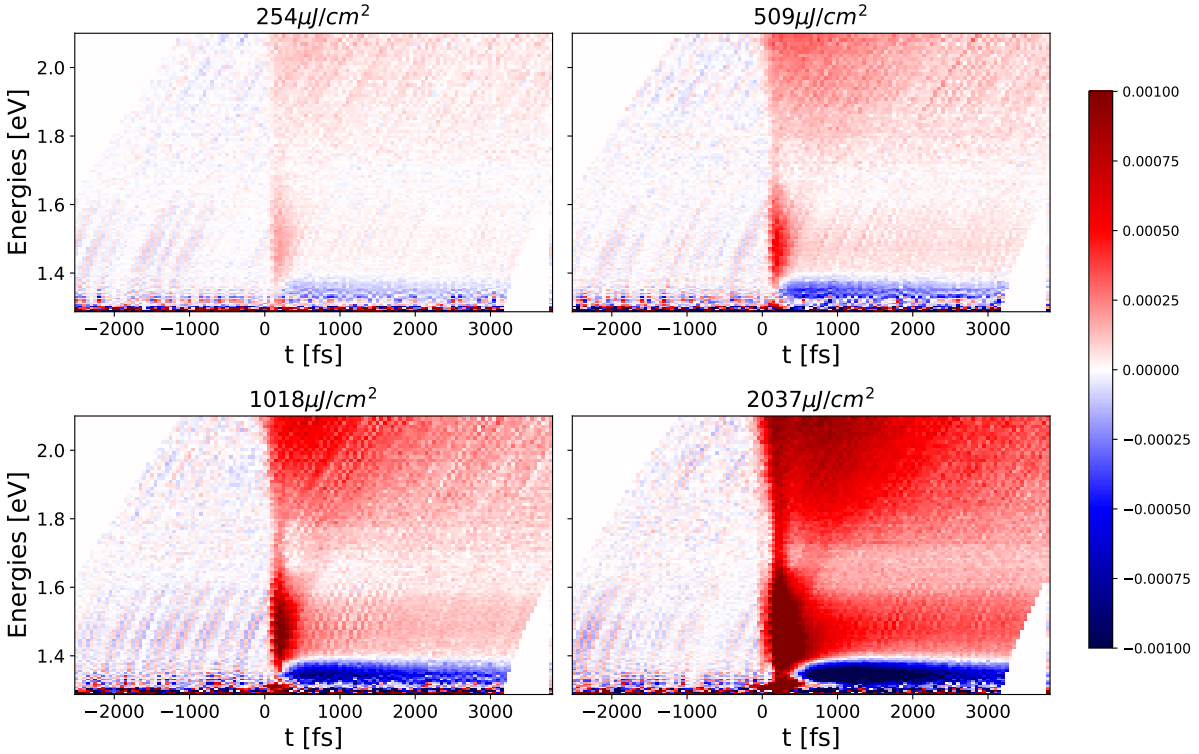

Figure 15: Single channel $\Delta R/R$ signal at different pump fluences with **17** μm pump wavelength

Like mentioned before the only interest we have in these tests is to observe at what measured fluences we observe the boundaries of our linear regime, represented by the emergence of a

[11] What is meant by linear in this context is that by doubling the pump power the resulting signal is doubled, without other qualitative changes.

second peak dynamic at higher fluences [22], such as the one that appears in Figures 16b, 16c. In figure 16a the same phenomenon could be represented by the shift at more positive times of the negative dynamic due to the emergence of a positive peak after the overlap.

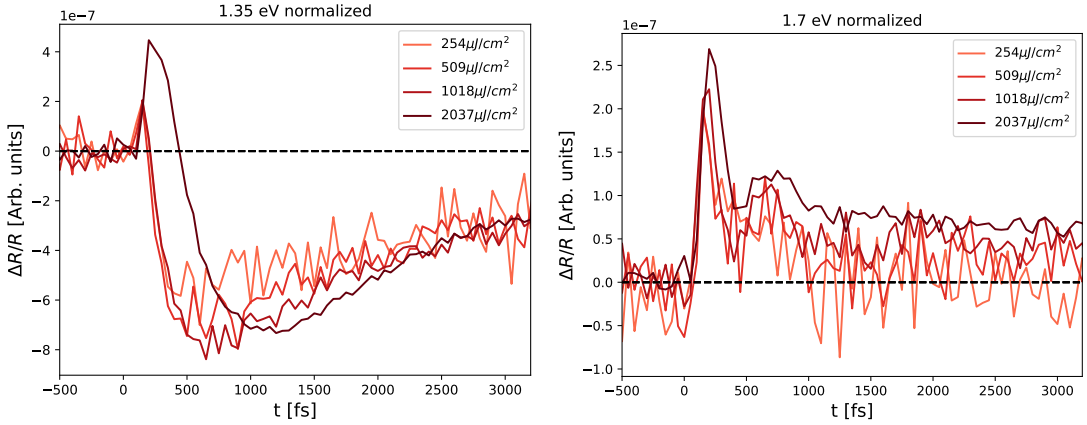

(a)

(b)

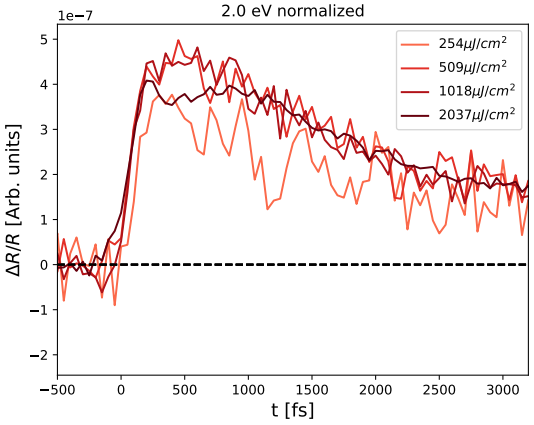

(c)

Figure 16: Cuts at fixed energy of the signals in figure 15, divided by their pump fluence value to better visualize the emergence of nonlinearities. The titles of the plots indicate the chosen energy and the labels the pump fluences.

Following these measurements (and those in same conditions, different configuration) we fixed the probe fluence at $764\,\mu\mathrm{J/cm^2}$ for all the birefringence experiments, which clearly sits below the boundary of the linear regime, that should be between $1000 - 2000\,\mu\mathrm{J/cm^2}$ from the observation of 16.

2.3 Single channel response

We start our investigation by presenting the Single Channel response, that is dynamic map measured with a single detector (e.g. Channel 1 in figure 27) and is hence associated to a single polarization component, which is the kind of information also presented in the previous fluence study (see 2.2.2).

Most of our observations are quite similar to the results of *Giannetti et al.* [27] for the different doping regimes, even though in their experiment they used a pump in the visible and therefore at energies higher than the gap. By switching our pump to $10\,\mu\mathrm{m}$ we obtain analogous results to the $17\,\mu\mathrm{m}$ experiment, with the only qualitative difference found in the emergence of the ultrafast response at high fluences that was discussed in section 1.3.1 and discovered in [22],

associated to above gap excitations.

Since the extent of three phases is different for different doping, to have a constant reference on the measurements we will examine the samples at close temperatures: around 80 K for SC, 108 K for and 300 K for normal phase. All the measurements were taken in the linear regime explored in section 2.2.2.

Superconducting phase

The dynamic response measured in the superconducting phase is characterized by a slow decay dynamics, usually attributed to the bottleneck regime described by the Rohwarf-Taylor model (see the cuts at fixed energy of figure 17 in figure 2.3); if fitted with the convolution of an exponential and a Gaussian curve, the decay constant ranges from $\tau \sim 1.4$ to 1.7 ps[12], in particular it's lowest at lower energies. As visible in figure 17 there is a strong doping dependence for what concerns the sign of the reflectivity: the high energy signal is positive in every sample, but going to low energies we see negative features appearing towards higher dopings. In particular, for overdoped and underdoped samples we observe a fast positive (~ 100 fs) peak followed by a negative decay dynamic centered at ~ 1.35 eV.

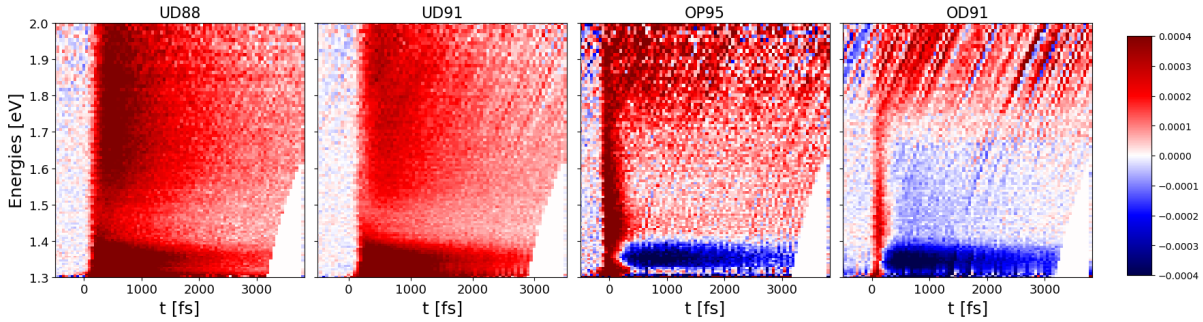

Figure 17: Single channel signal (pump $\parallel$ *CuO* configuration) for all the tested dopings in the superconducting phase.

[12]The fit on the whole spectrum can be done on the UD samples, the negative trace in the others cannot be fitted by this function.

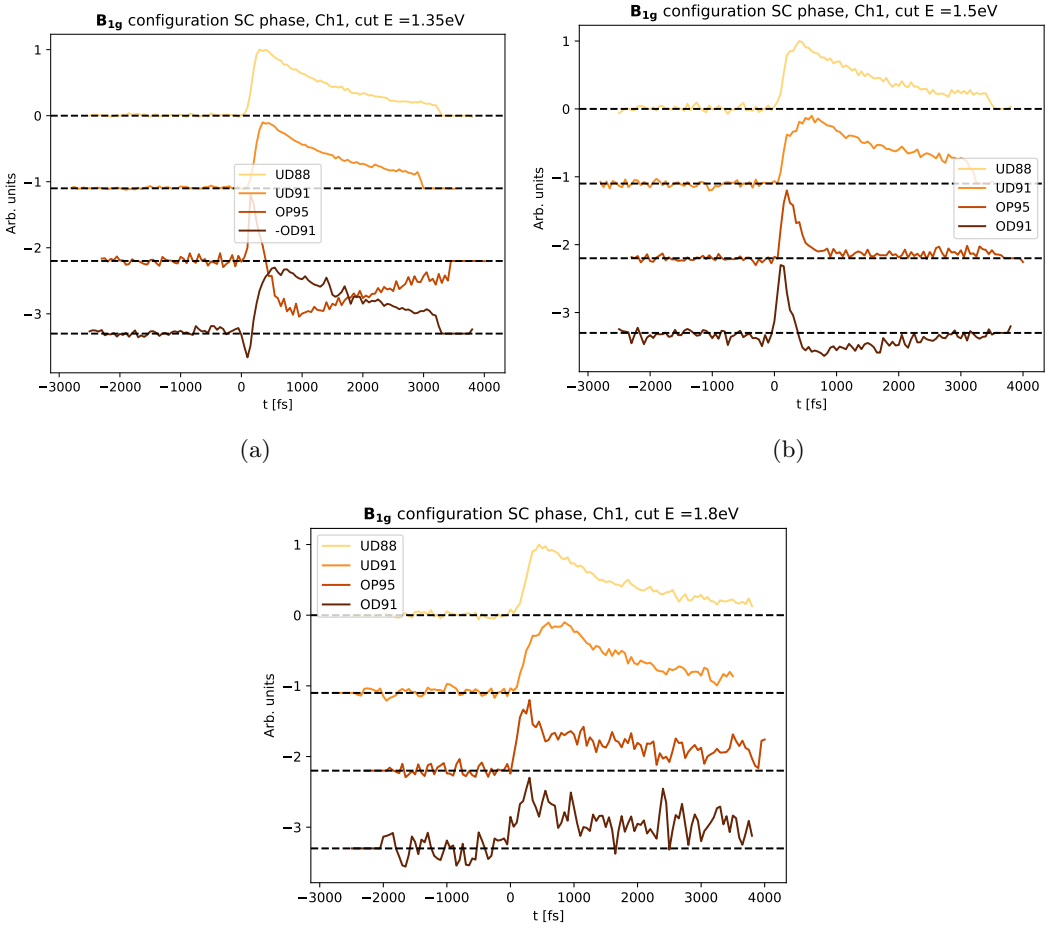

Figure 18: Cuts at fixed energies (in the titles) for the superconducting single channel maps of figure 17.

In the OD sample, the reflectivity changes sign at $\sim 1.7\,\text{eV}$, with lower intensity compared to the already discussed feature. In the OP samples the negative signal is limited to below $1.35\,\text{eV}$ and in the UD samples it is always positive. The structure of the signal does not change strongly in temperature within the phase.

Pseudogap phase

From figure 19 we can see that the pseudogap response is characterized by a positive signal localized at low energies, with a decay time of $\tau \sim 0.7\,\text{ps}$. In all the samples, a negative fast-decaying signal appears at higher energies and slowly closes as the sample approaches T^*. By increasing the doping[13] the negative trace opens at higher energies, leaving a wider positive signal in the lower part of the map.

[13] Thus also decreasing T^*.

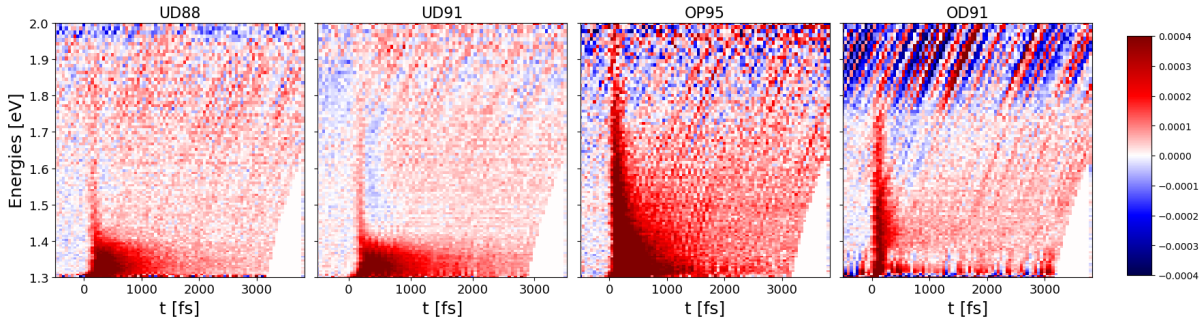

Figure 19: Single channel signal (pump $\parallel$ CuO configuration) for the four samples in the pseudogap phase. The optimally doped sample is noisy, in other similar measurements it shows the negative trace characteristic of this phase.

Normal phase

In this phase there are no peculiar structures, the signal is always positive and fast decaying for all the samples, as shown in figure 20.

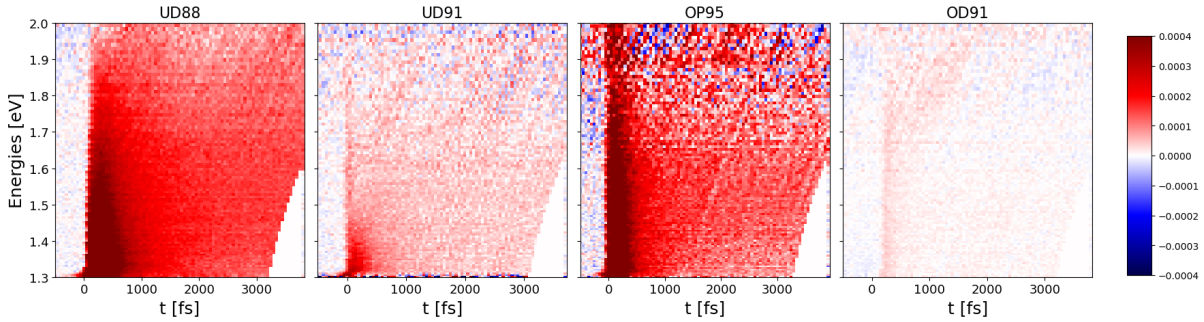

Figure 20: Single channel signal (pump $\parallel$ CuO configuration) for the four samples in the normal phase.

2.3.1 Temperature dependence

To show how the single channel signal changes across the different transitions, in the present section we will the results of temperature scans across the expected transition temperatures T_c and T^*; we will use the information contained in these measurements if it is possible to do an "optical estimation" of the temperatures. In particular we will focus on the transition to the normal phase, which we will see is also harder to retrieve from the birefringence measurements. To this end we report maps obtained by averaging the first picosecond of signal and plots derived by further averaging energy regions of these maps.

In general, the transition between superconducting and pseudogap phase is quite abrupt, in a few Kelvin the map passes from figure 17 to figure 19, while the transition to normal phase is more gradual.

UD88

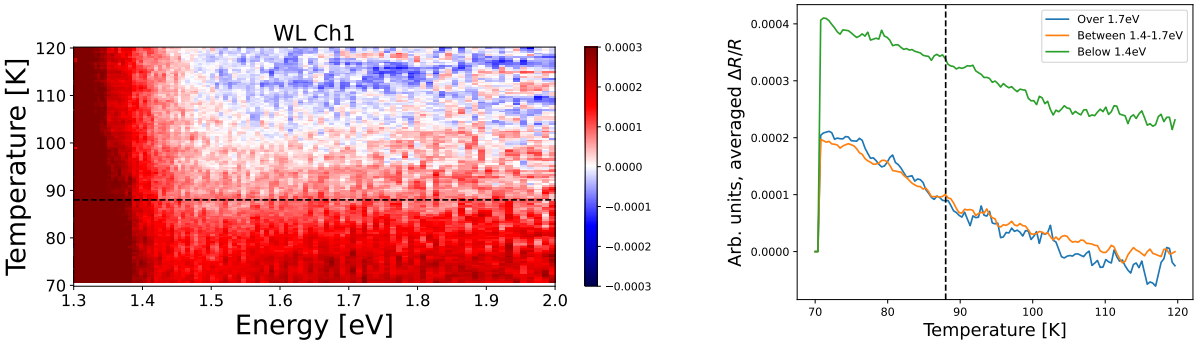

(a) (b)

Figure 21: Differential reflectivity signal temperature scan across T_c for the UD88 sample in the B_{1g} configuration. In figure (a) the measurement has been averaged along a picosecond duration to show the intensity of the reflectivity as a function of frequency an temperature, while in figure (b) it has been also averaged to compare the weight of different spectral regions (the regions are in the labels). The dashed lines indicates T_c.

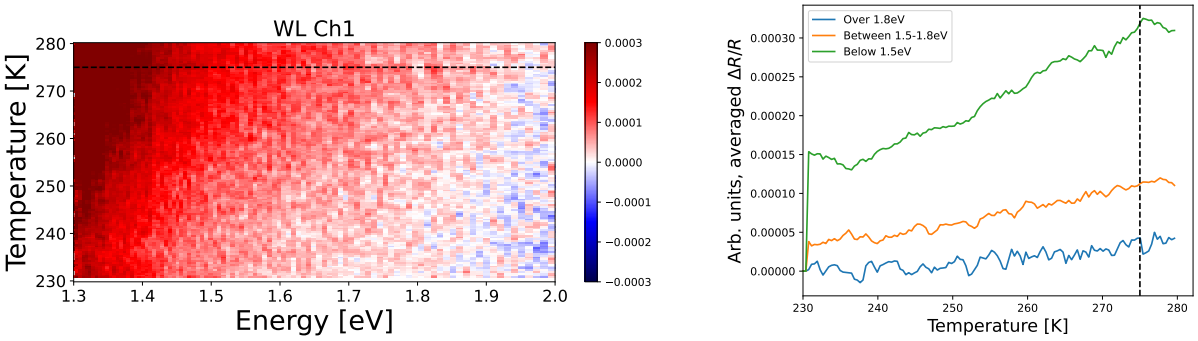

(a) (b)

Figure 22: Differential reflectivity signal temperature scan across T^* for the UD88 sample in the B_{1g} configuration. In figure (a) the measurement has been averaged along a picosecond duration to show the intensity of the reflectivity as a function of frequency an temperature, while in figure (b) it has been also averaged to compare the weight of different spectral regions (the regions are in the labels). The dashed lines indicates the estimated T^*.

UD91

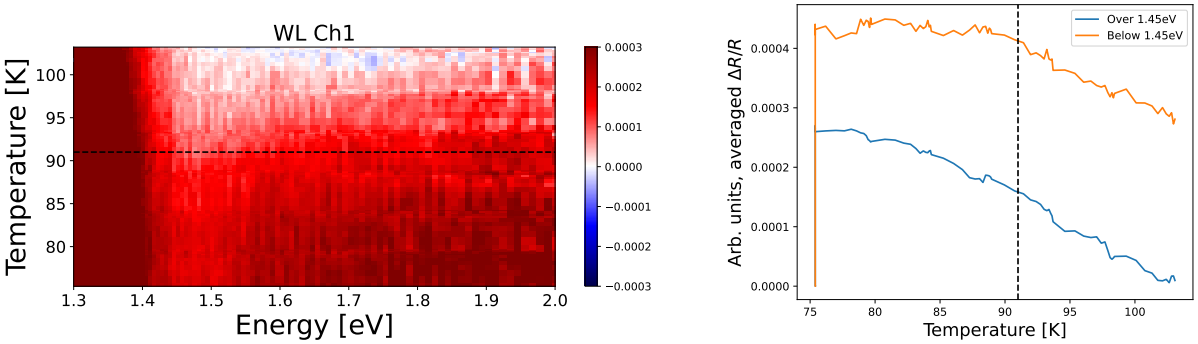

(a) (b)

Figure 23: Differential reflectivity signal temperature scan across T_c for the UD91 sample in the B_{1g} configuration. In figure (a) the measurement has been averaged along a picosecond duration to show the intensity of the reflectivity as a function of frequency an temperature, while in figure (b) it has been also averaged to compare the weight of different spectral regions (the regions are in the labels). The dashed lines indicates T_c.

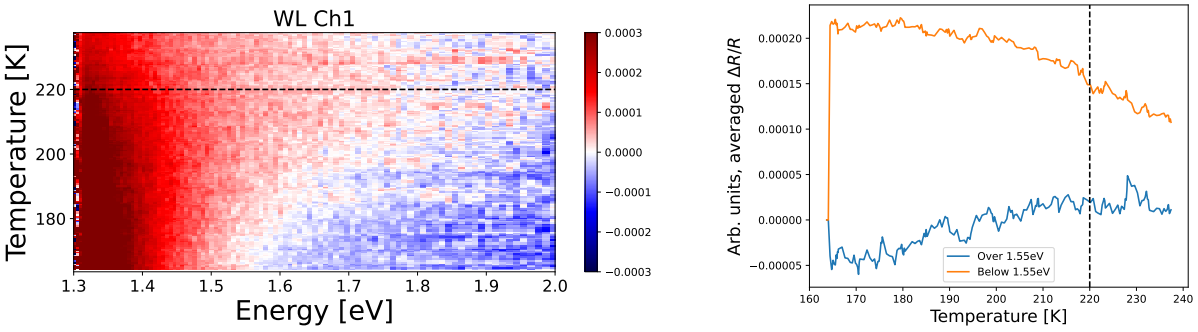

(a) (b)

Figure 24: Differential reflectivity signal temperature scan across T^* for the UD91 sample in the B_{1g} configuration. In figure (a) the measurement has been averaged along a picosecond duration to show the intensity of the reflectivity as a function of frequency an temperature, while in figure (b) it has been also averaged to compare the weight of different spectral regions (the regions are in the labels). The dashed lines indicates the estimated T^*.

OP95

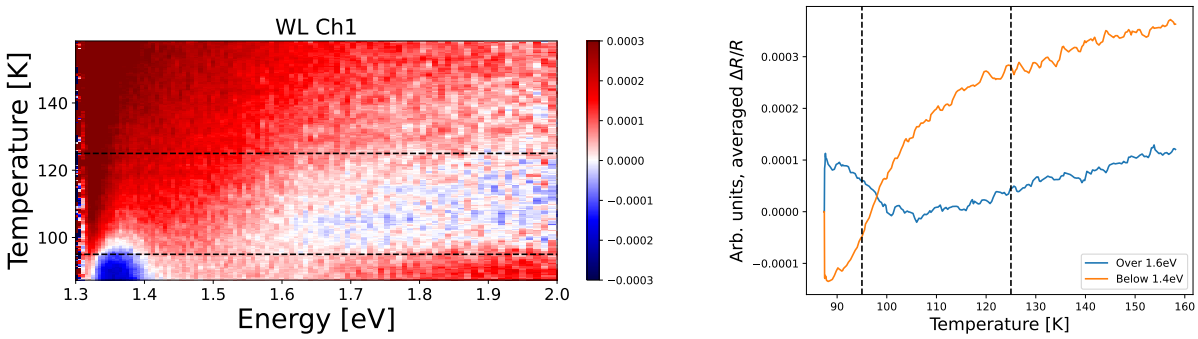

(a) (b)

Figure 25: Differential reflectivity signal temperature scan across T_c and T^* for the OP95 sample in the B_{1g} configuration. In figure (a) the measurement has been averaged along a picosecond duration to show the reflectivity of the birefringence as a function of frequency an temperature, while in figure (b) it has been also averaged to compare the weight of different spectral regions (the regions are in the labels). The dashed lines indicate T_c and the estimated T^*.

OD91

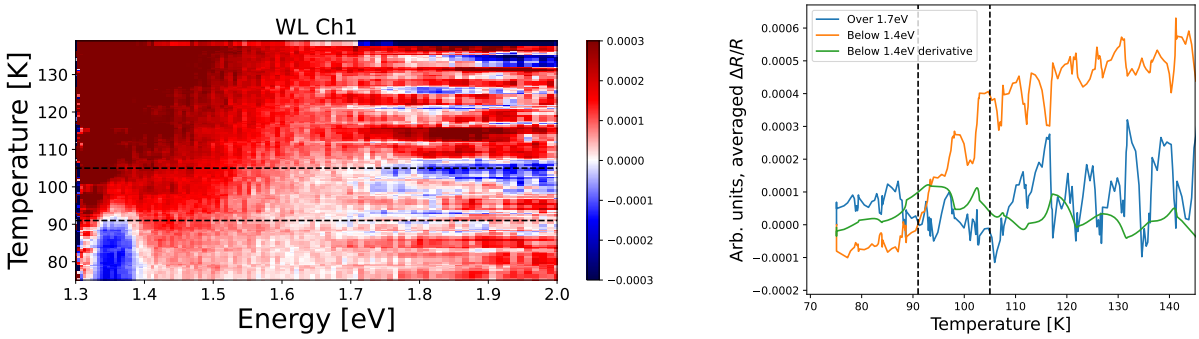

(a) (b)

Figure 26: Differential reflectivity signal temperature scan across T_c and T^* for the OD91 sample in the B_{1g} configuration. In figure (a) the measurement has been averaged along a picosecond duration to show the intensity of the reflectivity as a function of frequency an temperature, while in figure (b) it has been also averaged to compare the weight of different spectral regions (the regions are in the labels). The dashed lines indicate T_c and the estimated T^*.

In every sample the transition to pseudogap is defined by the opening of the negative signal, the lower bound of which increases with the increasing of the doping (see figures 21a, 23a, 25a, 26a); in the OP95 and OD91 samples the nonlinear feature at low energies also disappears at T_c. In the underdoped samples the positive features at higher energies leave space to the negative signal, while the positive signal at lower energies decreases (at higher temperatures this signal increases again). The end of the pseudogap is instead marked in all samples by the slow closing of the negative trace, which results in an increase of the signal obtained by integrating the upper portion of the spectrum, as visible in figures 22b, 24b, 25b, 26b. By using the change of trend in these plots as a reference (it ends in a plateau), we can extrapolate an estimate for T^* underdoped samples. For the OP95 and OD91 the transition is better mapped by the integration of the low energy signal, that rapidly increases and then settles to linear growth. In

this case the T^* could be defined from this change of trend[14].

Sample	UD88	UD91	OP95	OD91
T^* estimate [K]	275	220	125	105

These estimates are not to define the real values of the pseudogap, but to have a reference and to understand what this kind of measurements can show, reasonably being linked to the actual transition (this approach probably underestimates the real size of the pseudogap region).

Single channel conclusions

The single channel measurements do not give us information on the specific electronic modes, but they clearly show us how the doping affects the signal in the superconducting state. The signal in the pseudogap phase is similar in all of the samples, apart from a shift in the characteristic negative trace. Temperature scans allow us to map the different phases and transition temperatures, in particular the end of the superconducting phase could be easily identified in all the samples, while T^* is harder to state due to noise in the measurements and to the gradual nature of the transition, but still detectable.

2.4 Birefringence measurements: B_{1g} electronic mode

Before introducing the content of this section we show all the information that goes into a single birefringence map, as explained in equation 21. In figure 27 we see both the detection channels and the difference (*Ch0-Ch1*) is the resulting birefringence signal.

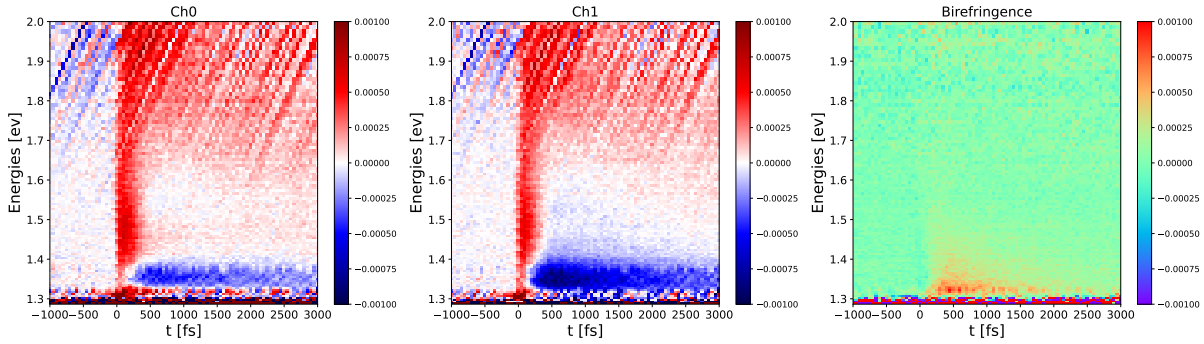

Figure 27: Two single channel maps (on the left and center) and their difference (on the right), result of a measurement in the superconducting phase.

The reader might have noticed (already from the single channel measurements) that even though the spectrum of the white light reaches 2.2 eV the signal is not shown beyond 2 eV. This is because of the working range of the polarizing beam splitter used for the birefringence measurement (see figure 9, before the detection).

By orienting the pump polarization parallel to the CuO direction we can isolate the B_{1g} electronic mode. This direction is associated to antinodal excitations.

2.4.1 Superconducting phase

The observed response is rather similar between samples: there is an ultra-fast peak at the overlap, and a low intensity signal present at all energies (picture 28).

[14] Using a Gaussian filter on the data and the doing their derivative can help finding the point of constant slope accurately.

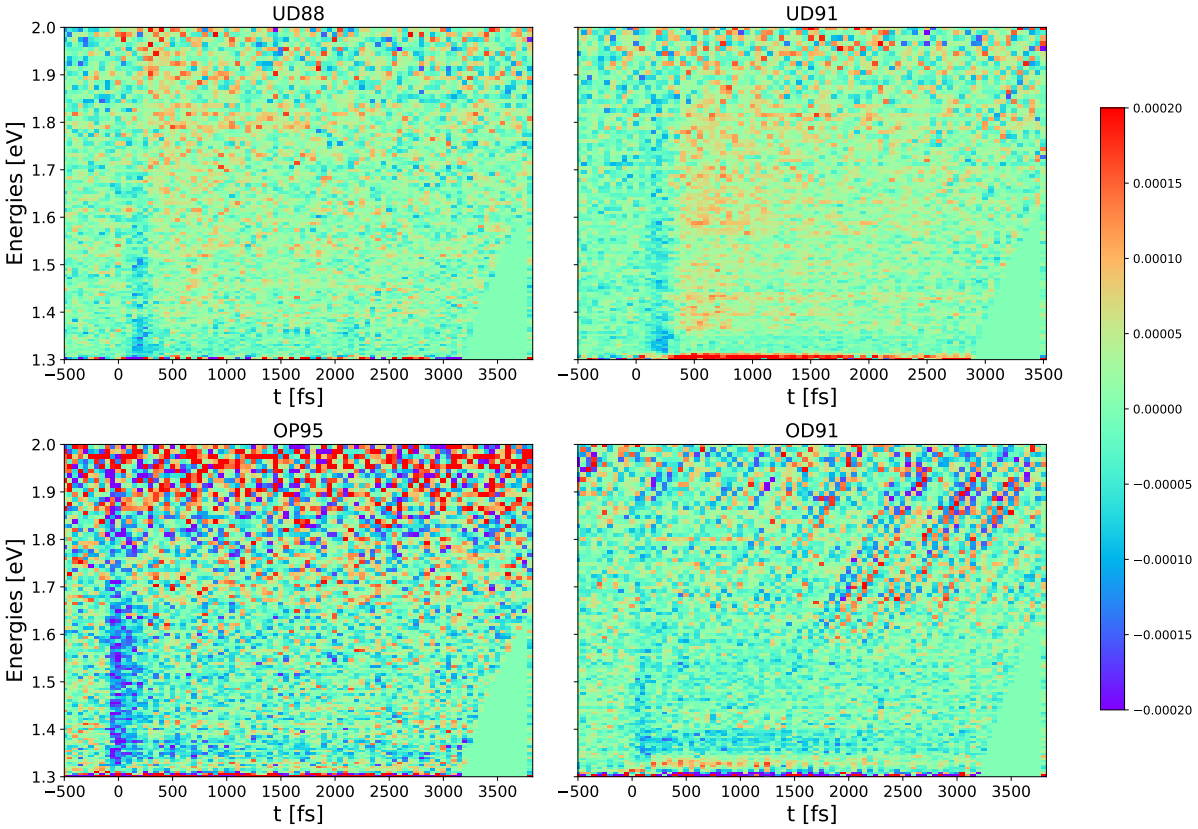

Figure 28: Birefringence signal of the four samples in the superconducting phase in the B_{1g} electronic mode isolation configuration.

While the sign of the birefringence is arbitrary, it should be noted that all maps show a negative ultrafast feature at the overlap, but the following weak signal changes sign from the underdoped to the overdoped regime.

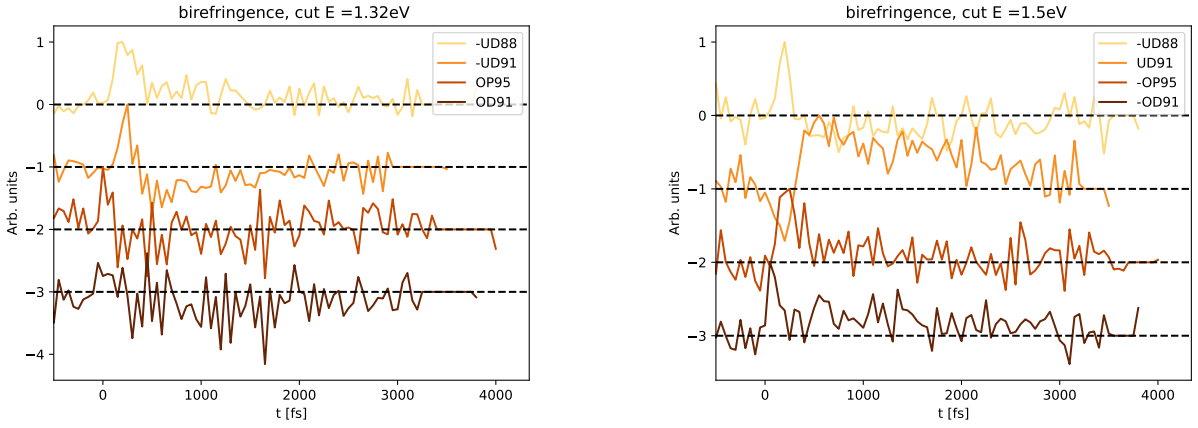

(a) (b)

Figure 29: Cuts obtained by setting $E = 1.32\,\text{eV}$ (a) and $E = 1.5\,\text{eV}$ (b) in the superconducting birefringence maps (37). To reduce the noise the map has been averaged around the central frequency, in a $\pm 10\,\text{meV}$ range. In the legend the minus signs indicate a multiplication by -1 to make a clearer comparison between the different samples. The noise in the OD91 sample is due to probe instability.

At low energies one can see that the signal changes sign between $\sim 1.3 - 1.4\,\text{eV}$. This was originally dismissed as an artifact caused by a frequency calibration mismatch, but the

reality of this feature became more feasible as it presented for all the samples only in the B_{1g} configuration, even though the signal is still too weak to make strong statements. The feature is observable in the fixed time cut in figure 30, and by reading the legends of the figures in 29 one can notice that between the two energies there is a sign flip.

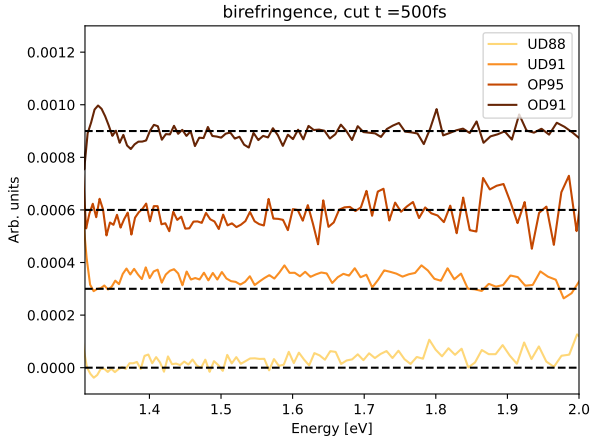

Figure 30: Cuts at fixed delay $\Delta t = 500\,\mathrm{fs}$ in in the superconducting birefringence maps (28). At all energies the signal is much weaker than the B_{2g} counterparts.

2.4.2 Pseudogap phase

In the pseudogap phase the long lived signal disappears, leaving a significant short lived signal localized in the low energy region (figure 31). This region is the same where the positive signal is localized in the single channel measurements. (figure 19).

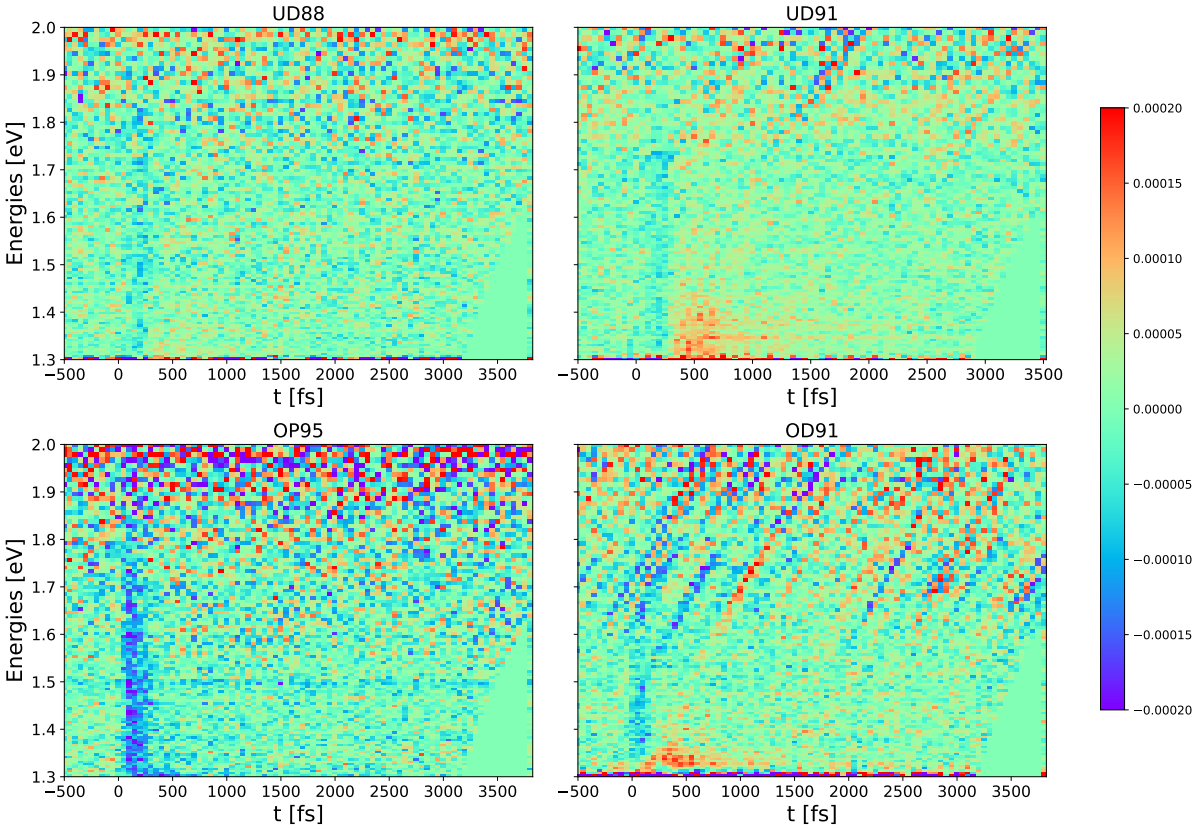

Figure 31: Birefringence signal of the four samples in the pseudogap phase in the B_{1g} electronic mode isolation configuration.

2.4.3 Normal phase

In the normal phase the birefringence still shows the ultrafast response at the overlap and a very weak signal afterwards in all samples but the OD91, where the signal is zero (see figure 32).

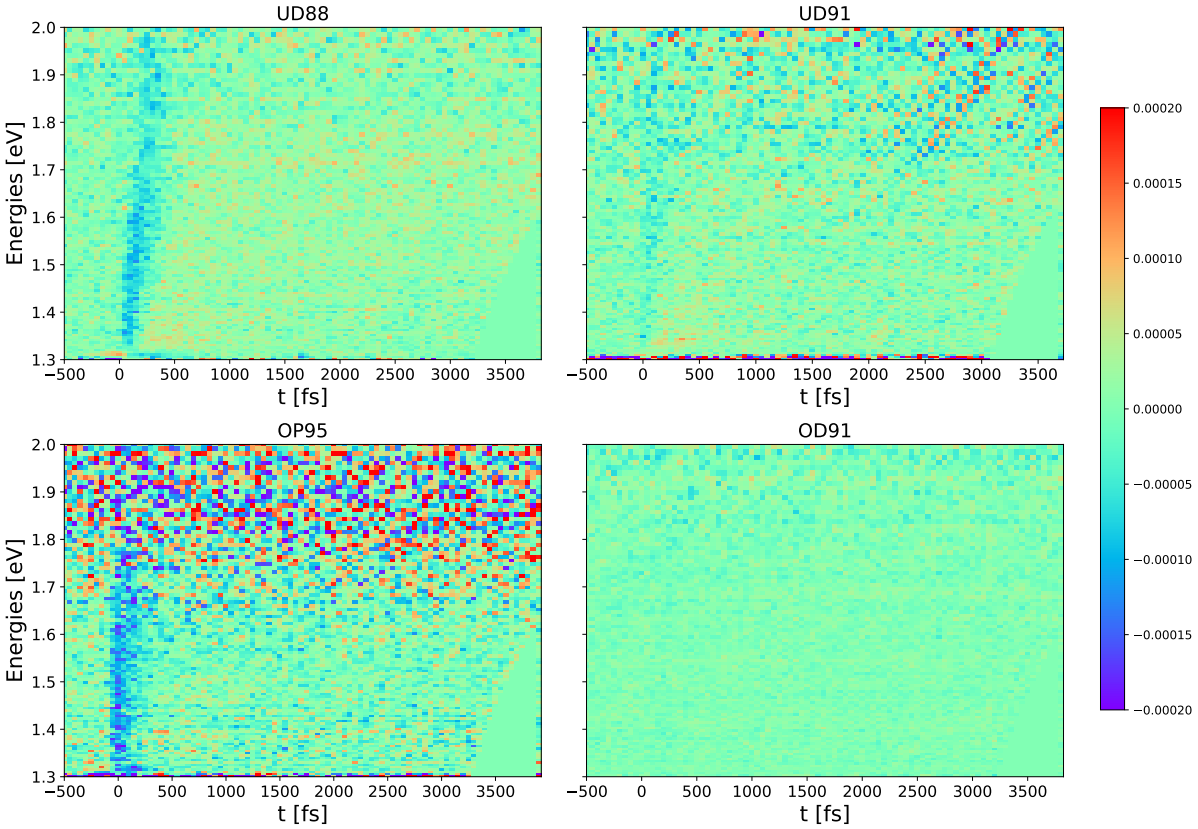

Figure 32: Birefringence signal of the four samples in the pseudogap phase in the B_{1g} electronic mode isolation configuration.

2.4.4 Temperature dependence of the B_{1g} mode

In the past sections we have seen how the signal is in the different phases, and more precisely how it is at $T = 80, 108, 300\,\mathrm{K}$, at temperatures at which we know the samples are respectively in the superconducting, pseudogap and normal phase. To characterize the transitions between the different phases, we performed temperature scans of the samples: through the control of the cryostat we repeated the measurements by gradually increasing the temperature across their transitions; it has to be clarified that the measured temperature is a good but not high precision reference, because it doesn't account for the laser heating (which is an intrinsic problem of pump-probe measurements); as a matter of fact if the following section the transition will happen at temperatures lower than the actual T_c, which will be shown for reference. For this last consideration an effective temperature can be evaluated but it is not of our interest to have such a precise value.

In this section we will show some of the results of these experiments for the B_{1g} electronic mode, in particular for the superconducting-to-pseudogap transition. Temperature scans of the pseudogap-to-normal phase transitions were also taken, but their birefringence is very weak and in most samples it is difficult to see a change in the signal (see Appendix A), so they will not be shown.

The plots shown in this section are obtained by averaging of the first picosecond of the temperature scan (on the left side), so they are a function of temperature and energy, and by further averaging energy ranges of these we obtain the other plots of the section, which help to visualize the presence of a phase transition (on the right side).

UD88

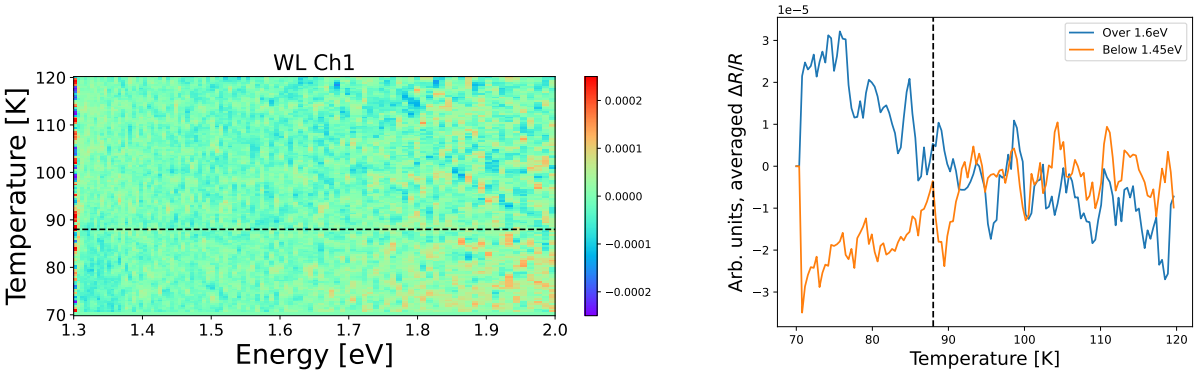

(a) (b)

Figure 33: Birefringence signal temperature scan across T_c for the UD88 sample in the B_{1g} configuration. In figure (a) the measurement has been averaged along a picosecond duration to show the intensity of the birefringence as a function of frequency an temperature, while in figure (b) it has been also averaged to compare the weight of different spectral regions (the regions are in the labels).

UD91

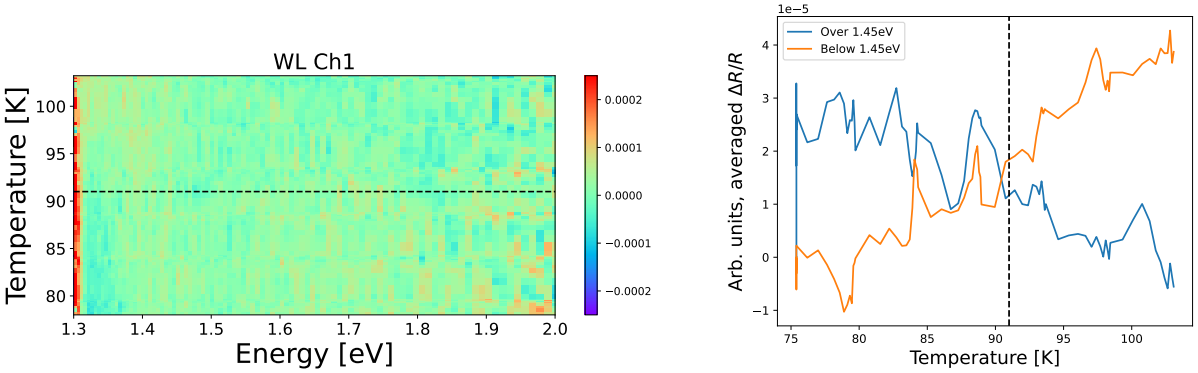

(a) (b)

Figure 34: Birefringence signal temperature scan across T_c for the UD91 sample in the B_{1g} configuration. In figure (a) the measurement has been averaged along a picosecond duration to show the intensity of the birefringence as a function of frequency an temperature, while in figure (b) it has been also averaged to compare the weight of different spectral regions (the regions are in the labels).

OP95

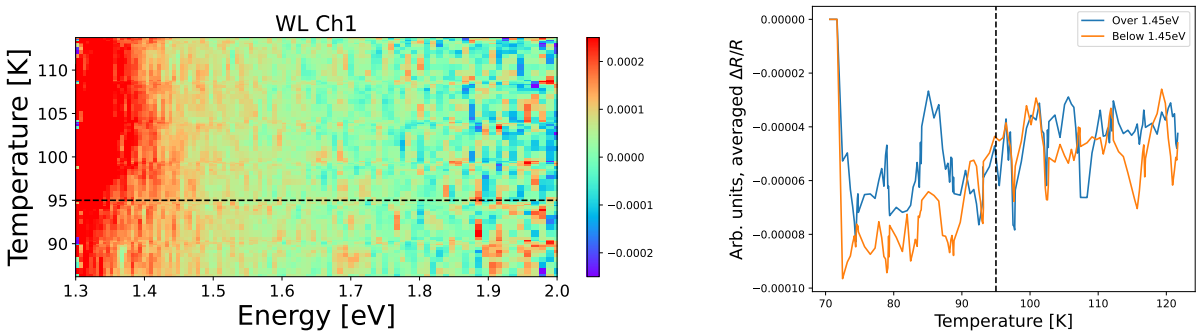

(a) (b)

Figure 35: Birefringence signal temperature scan across T_c for the OP95 sample in the B_{1g} configuration. In figure (a) the measurement has been averaged along a picosecond duration to show the intensity of the birefringence as a function of frequency an temperature, while in figure (b) it has been also averaged to compare the weight of different spectral regions (the regions are in the labels).

OD91

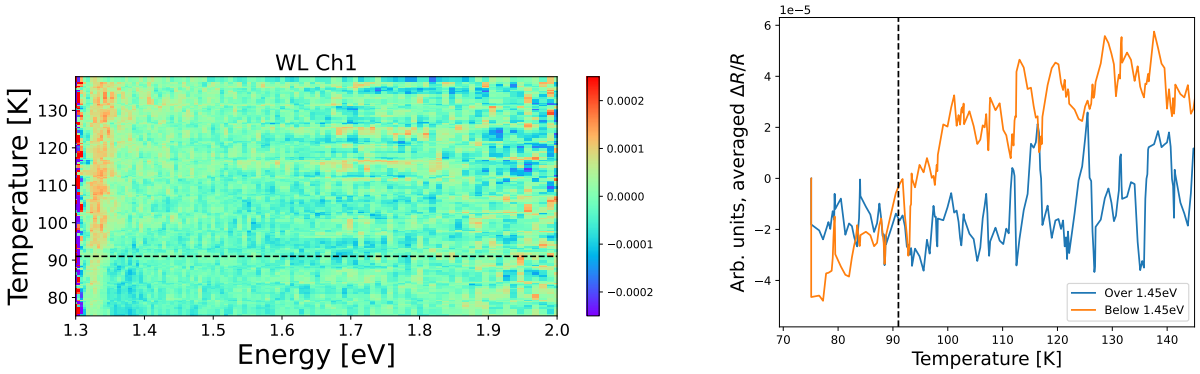

(a) (b)

Figure 36: Birefrincence signal temperature scan across T_c for the OD91 sample in the B_{1g} configuration. In figure (a) the measurement has been averaged along a picosecond duration to show the intensity of the birefringence as a function of frequency an temperature, while in figure (b) it has been also averaged to compare the weight of different spectral regions (the regions are in the labels).

From both the left side and right side images it is possible to distinguish a change of trend around critical temperature for every sample. In the UD88 sample (see figure 33a), one can see how both the negative signal at low energies and the positive signal at higher energies decay to zero, as shown in their integration in figure 33b. In the UD91 sample instead the change is visible as a form of spectral weight transfer to lower energies, as visible in figures 34b and 34b. In the OP95 sample it is harder to define a trend but from figures 35b and 35b it can be seen that the low energy signal increases across the transition, while for the OD91 this increase in signal is clearly visible (see figures 36b and 36b)

2.5 Birefringence measurements: B_{2g} electronic mode

By orienting the pump polarization parallel to the $CuCu$ axis of the sample we can isolate the B_{2g} electronic mode. This direction is associated to nodal excitations.

2.5.1 Superconducting phase

By orienting the pump polarization parallel to the $CuCu$ direction in the sample we can isolate the B_{2g} electronic mode; this direction is associated to nodal excitations. Differently from the B_{1g} mode we see a clear intense signal (figure 37) with a long-lived exponential decay at different energies, as visible in figure 38. In this configuration the energy localization of the long-lived excitations largely depends on the doping of the samples: the response of the signal in the observed range moves from higher energies in the underdoped regime to lower ones increasing the doping, as clearly visible in figure 39.

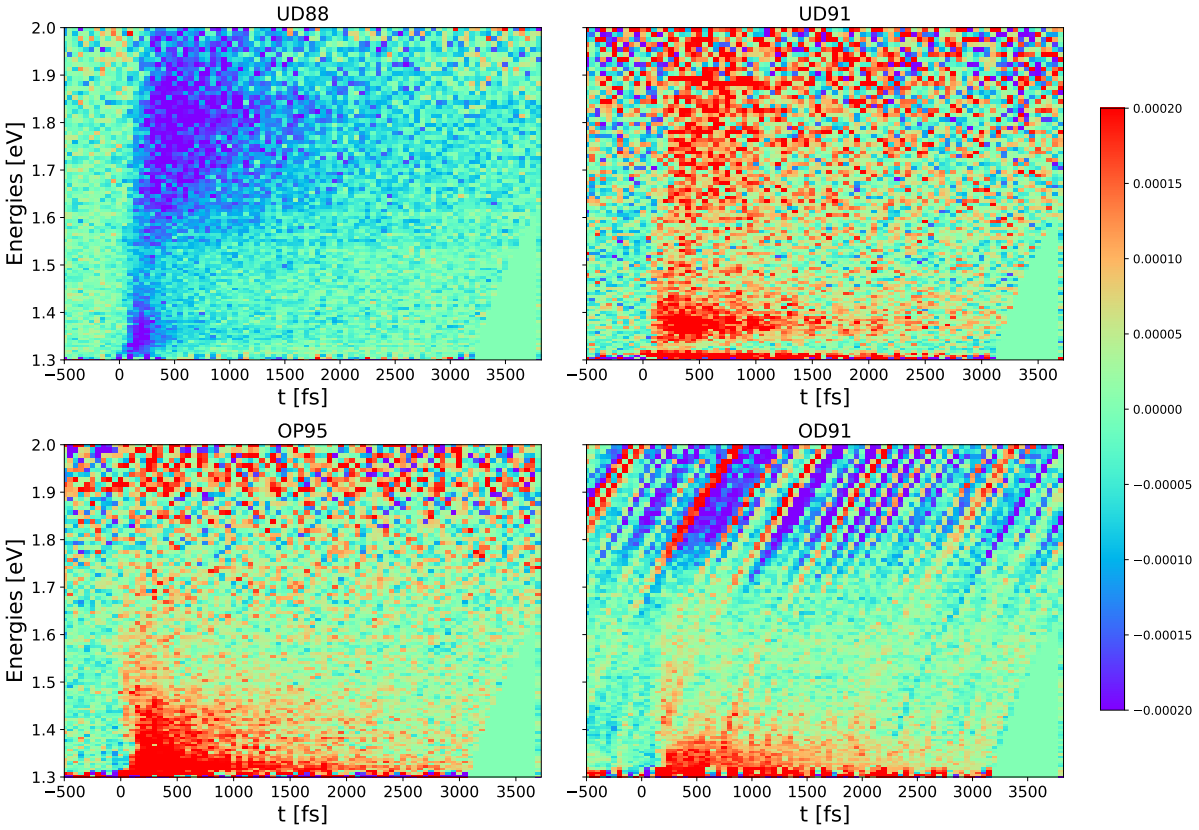

Figure 37: Birefringence signal of the four samples in the superconducting phase in the B_{2g} electronic mode isolation configuration.

In the regions were a slow decay dynamic is present the signal decays to zero in the order of picoseconds. The sign of the birefringence is in general not meaningful, as it depends on our arbitrary definition of $\frac{\Delta\Delta R}{R}$ and on the choice of the axis. It is interesting though that the signal shows the same sign at all energies in the samples in this configuration.

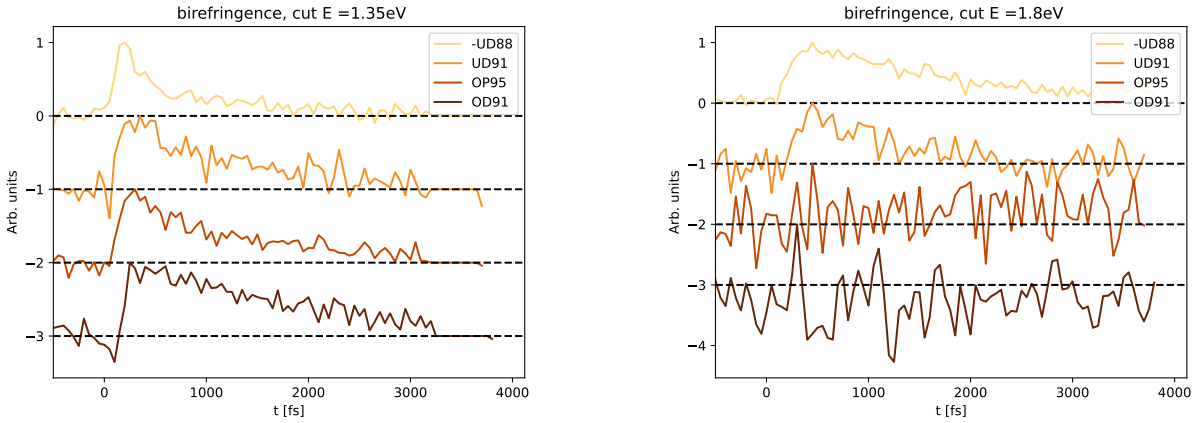

Figure 38: Cuts obtained by setting $E = 1.35\,\text{eV}$ (a) and $E = 1.8\,\text{eV}$ (b) in the superconducting birefringence maps (37). To reduce the noise the map has been averaged around the central frequency, in a $\pm 10\,\text{meV}$ range. The UD88 map has been multiplied by -1 to be compare more easily with the others.

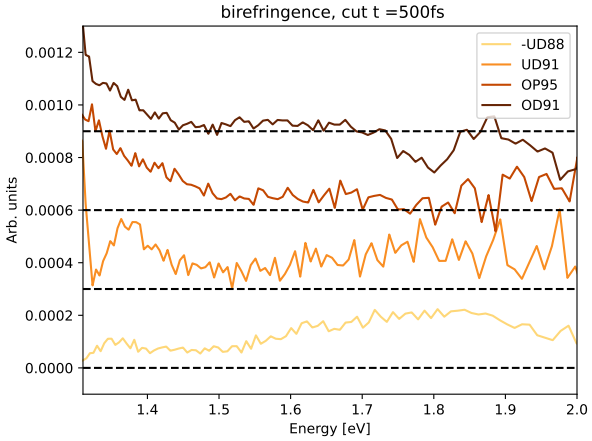

Figure 39: Cuts at fixed delay $\Delta t = 500\,\text{fs}$ in in the superconducting birefringence maps (37). The signal that appears at energies higher than 1.75 eV in the OD91 sample is just noise, the response should be flat otherwise.

2.5.2 Pseudogap phase

By heating the samples, bringing them in the pseudogap phase (Figure 40), the signal changes noticeably, both in its energy response and lifetime: the response results localized at lower energies (below 1.5 eV) in all of the samples, and its lifetime is drastically decreased, disappearing in around $\sim$ 1ps.

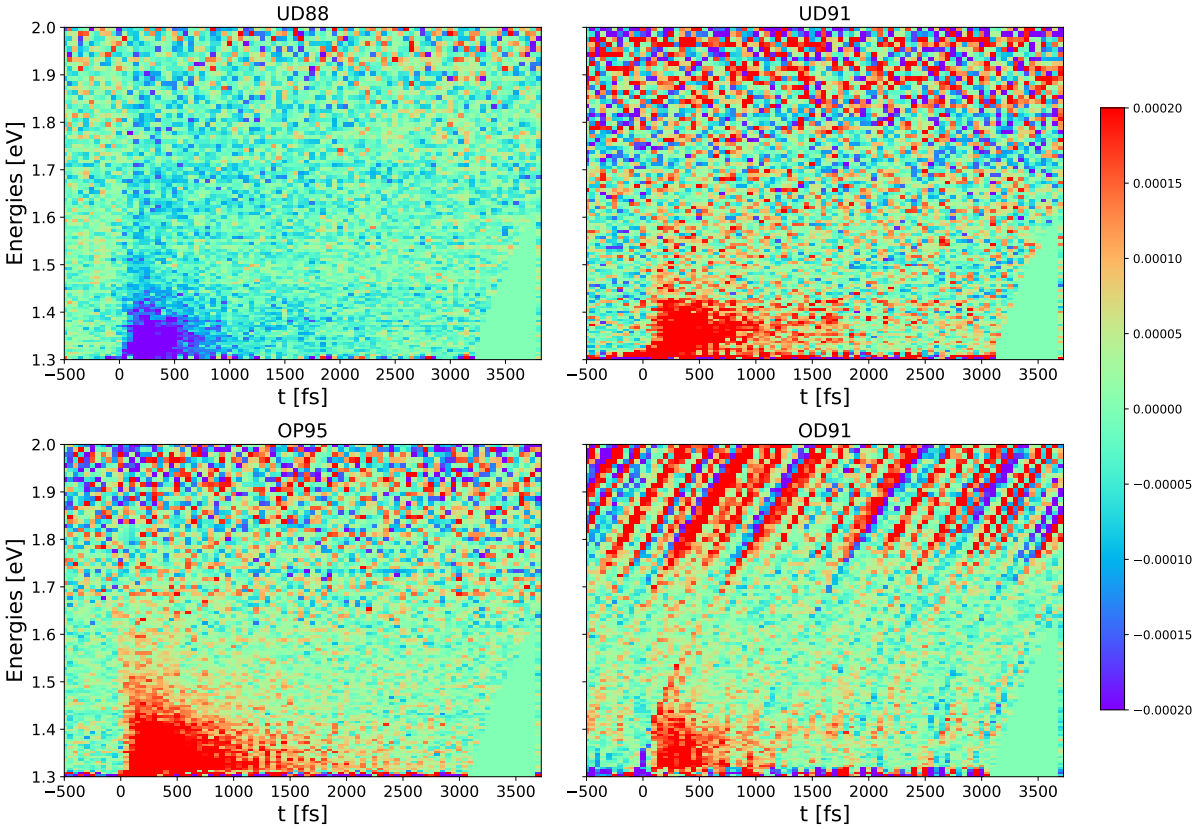

Figure 40: Birefringence signal of the four samples in the pseudogap phase in the B_{2g} electronic mode isolation configuration.

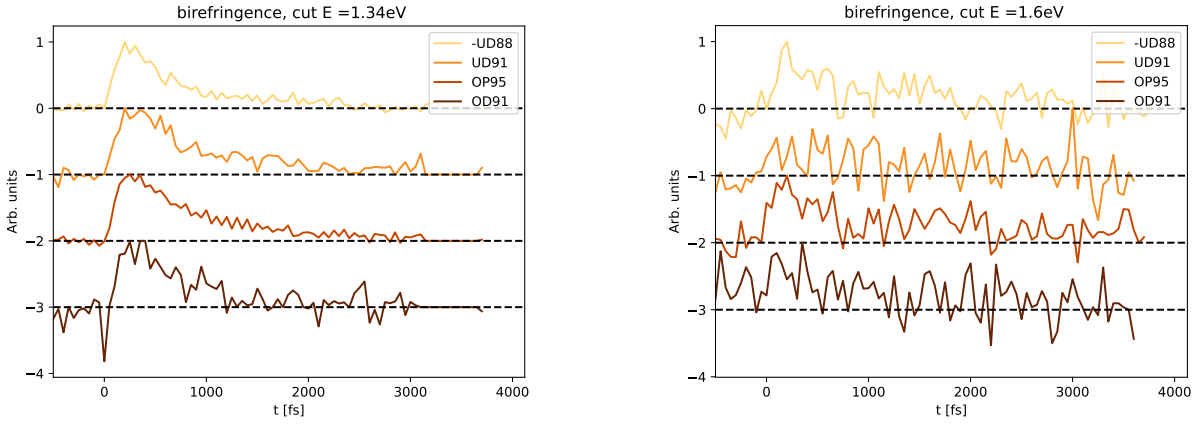

(a) (b)

Figure 41: Cuts obtained by setting $E = 1.35\,\text{eV}$ (a) and $E = 1.6\,\text{eV}$ (b) in the pseudogap birefringence maps (37). To reduce the noise the map has been averaged around the central frequency, in a $\pm 10\,\text{meV}$ range. The UD88 map has been multiplied by -1 to be compare more easily with the others. The noise in the OD91 sample is due to probe instability.

It is worth noticing that the region that in the single channel shows the characteristic negative reflectivity of the pseudogap does not show any peculiar birefringence trace. This could mean that the negative feature is not related to the B_{2g} electronic mode.

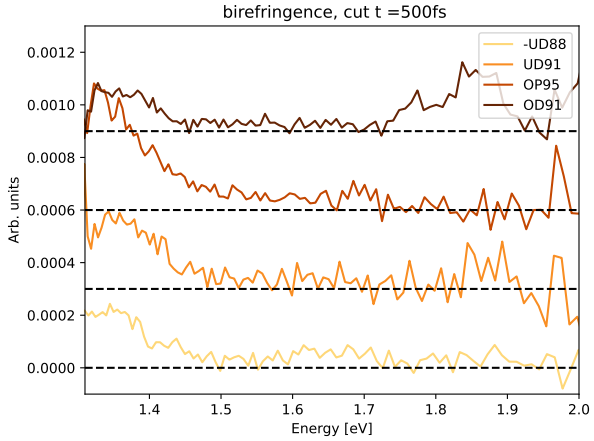

Figure 42: Cuts at fixed delay $\Delta t = 500\,\text{fs}$ in in the pseudogap birefringence maps (37). The signal that appears at energies higher than 1.75 eV in the OD91 sample is just noise, the response should be flat otherwise.

2.5.3 Normal phase

In the normal phase what remains of the signal is just a weak ultra-fast response at the overlap as can be seen in figure 43; the signal at positive times in the UD91 sample is noise as it doesn't appear in other measurements on this sample in similar conditions.

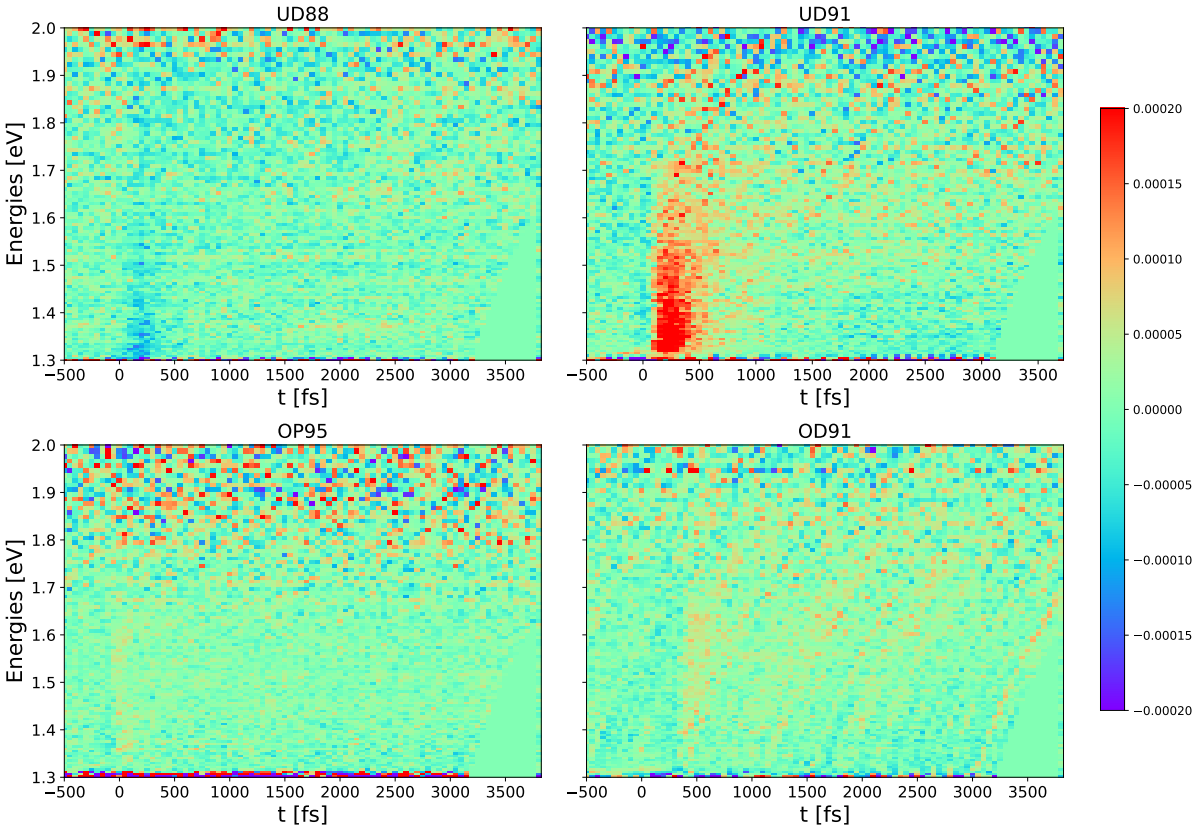

Figure 43: Birefringence signal of the four samples in the pseudogap phase in the B_{2g} electronic mode isolation configuration.

2.5.4 Temperature dependence of the B_{2g} mode

Like we have already done for the B_{1g} mode, we now present the plots that show the temperature dependence for the B_{2g} electronic mode in the different samples. The plots are made in the same way of the ones in 2.4.4. In this configuration the UD88 sample shows an exchange of spectral weight between lower and higher energies happening at temperatures lower than the expected T_c, at $T \sim 80$ (see figures 44a and 44b); something similar seems to be happening also in the UD91 sample (see figures 45a and 45b). In the optimally doped sample there are not any clear changes in figure 46a, the integration at low energies 46b shows a sudden increase of the signal at T_c.

UD88

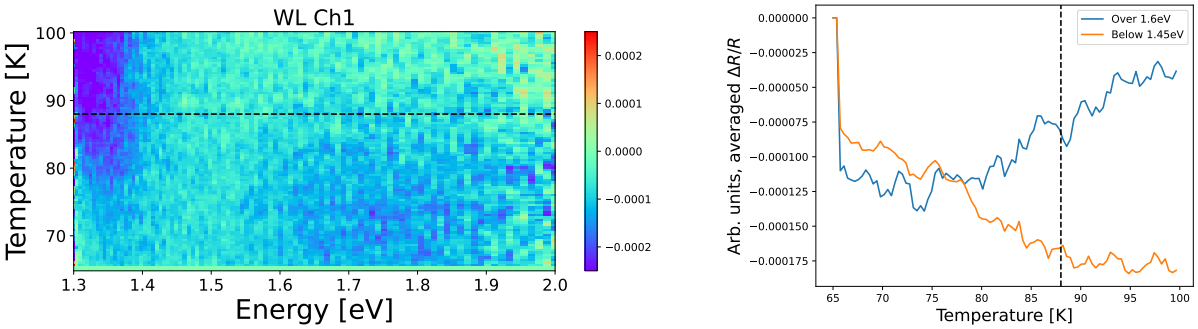

(a) (b)

Figure 44: Birefringence signal temperature scan across T_c for the UD88 sample in the B_{2g} configuration. In figure (a) the measurement has been averaged along a picosecond duration to show the intensity of the birefringence as a function of frequency an temperature, while in figure (b) it has been also averaged to compare the weight of different spectral regions (the regions are in the labels).

UD91

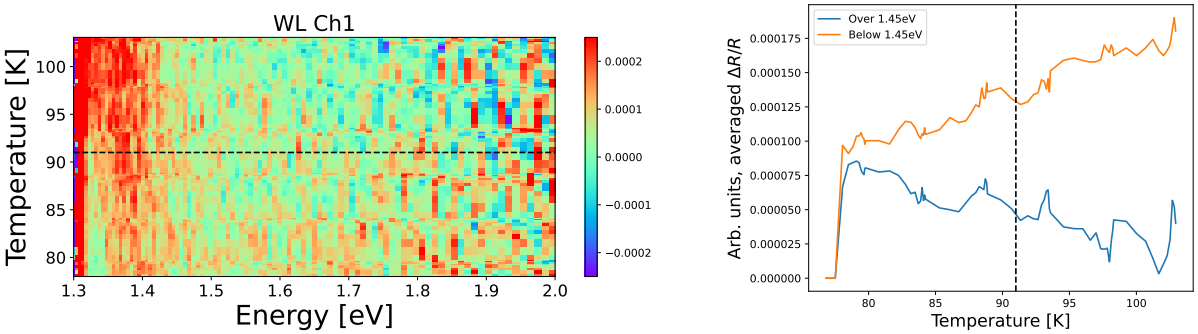

(a) (b)

Figure 45: Birefringence signal temperature scan across T_c for the UD91 sample in the B_{2g} configuration. In figure (a) the measurement has been averaged along a picosecond duration to show the intensity of the birefringence as a function of frequency an temperature, while in figure (b) it has been also averaged to compare the weight of different spectral regions (the regions are in the labels).

OP95

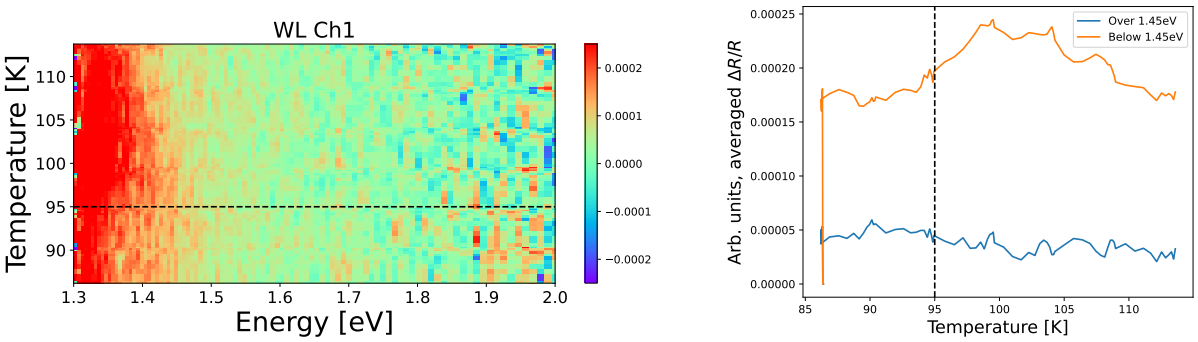

(a) (b)

Figure 46: Birefringence signal temperature scan across T_c for the OP95 sample in the B_{2g} configuration. In figure (a) the measurement has been averaged along a picosecond duration to show the intensity of the birefringence as a function of frequency an temperature, while in figure (b) it has been also averaged to compare the weight of different spectral regions (the regions are in the labels).

OD91

We did not manage to obtain a good measurement of the B_{2g} mode in the OD91 sample, due to strong instabilities in the supercontinuum. We managed to do a temperature scan using a detector for the reference signal, just to check the single-polarization information and the transition temperature.

2.6 Discussion

Having observed the different birefringence signals associated with the B_{1g} and B_{2g} electronic modes we can now summarize observations that could give more insight in the understanding of the optical properties of cuprates.

- **Phase dependence:** The observed signal is, as expected, richer and more visible in the superconducting state, where it is also more affected by the doping (see next points); this is consistent with the past measurements on BSCCO made by our group. In the pseudogap phase all the samples show a similar response.

- **Mode intensity:** The two electronic modes are rather different in these measurements, in particular the intensity of the signal, being much lower in the B_{1g} mode. This is more clearly observable in the cuts at fixed time (Figures 30,39), that show a difference in peak intensity which is more than a factor of two at the same delay with the same pump fluence. These observations are consistent with past experiments on BSCCO by our group ([19, 37]).

- **Doping dependence:**

  The B_{1g} superconducting signal is not affected by the doping in its spectral distribution, while the sign flip of the signal between the underdoped and the optimally/overdoped region can give us information and reflects the behavior of past measurements with monochromatic probe. Still it is hard to make solid statements due to the weakness of the signal.
  The B_{2g} electronic mode is radically affected by the doping, with a shift of the signal from high to low energies as the doping is increased. It is interesting to observe on a broadband scale that not only the full spectral weight (i.e. what we see in the single channel), but a single electronic mode is affected by the anomalous spectral weight distribution. In the pseudogap phase also this mode does not show marked qualitative differences at different dopings.

From these birefringence measurement we thus learned that the B_{1g} and B_{2g} broadband response for a sub-gap excitation is radically different, in particular the latter is strongly affected in its distribution by the doping of the sample, showing more spectral weight at higher frequencies, figure 39 exemplifies this behavior. From the the temperature studies it is clear that even with the weak B_{1g} signal it is possible to observe the transition between superconducting and pseudogap phases.
To move to the next section we remember once again that the results and observations just discussed have been obtained through a *chirped* supercontinuum probe, and that the first part of the spectrum impinging on the sample si the low frequency one.

3 Effects of chirped probe light in the superconducting phase

As already stated in section 2.2.1 the results of *Polli et al.* [36] tell us that in pulse frequency resolved experiments we can obtain the same time resolution of compressed probe pulse experiments by using chirped pulses and then correcting the resulting map. The white-light supercontinuum probe experiments on BSCCO done so far follow this paradigm. However, we know that a chirped pulse can have strong effects on complex materials, and in recent simulations [38] also high-temperature superconductors have been shown to present a reaction to chirped excitations.

To test the possibility that introducing a chirp our probe might produce any change in the signal, we used the SLM based pulse shaper to manipulate the probe. This component allows us to independently control spectral amplitude and spectral phase, making it possible to choose which frequency components to slow down. To make clear what we mean by negative and positive chirp, we show a graphic example in figure 47. A signal is said to be chirped if its instantaneous frequency[15] increases (or decreases) continuously with time. In the context of the experiment this means that for a positive chirp the first frequencies impinging on the sample are the low frequencies, while for the negative chirp it is the opposite.

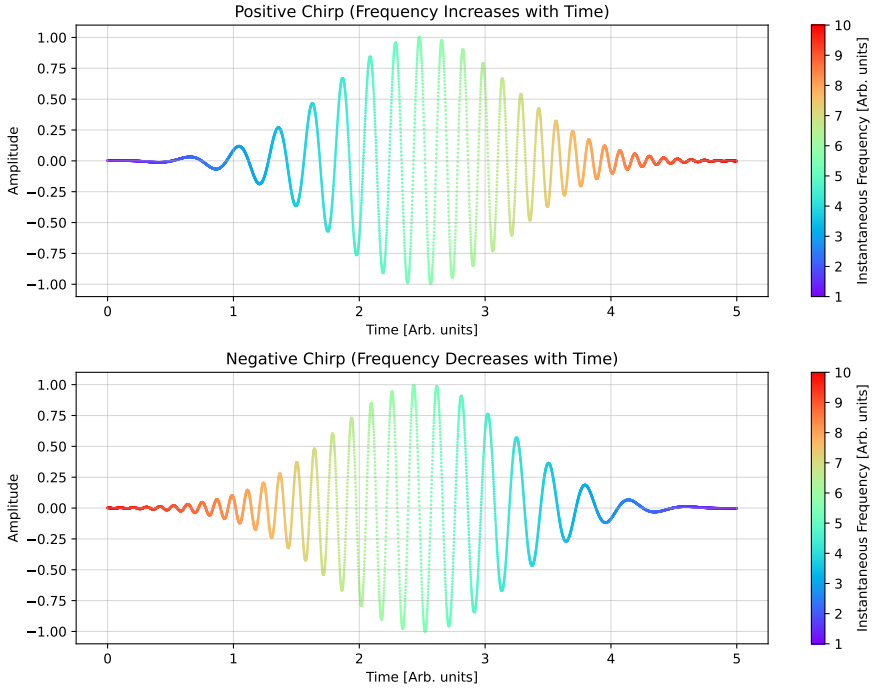

Figure 47: Graphic example of a chirped signal evolution in time

3.1 Tests and results

What was observed is that for even a slight chirp (positive or negative) the shape of the signal noticeably changed: **the spectral weight shifts to different frequencies, in particular in the direction of frequencies that interact first with the sample**. The effect does not appear to be affected by the doping of the system. Independently from the explanation of the phenomenon, this reminds us the complex nature of quantum correlated materials and that even the probe causes a non-negligible effect in such experiments.

[15] In nonlinear optics this refers to the frequency of the carrier wave of the pulse, to be specific.

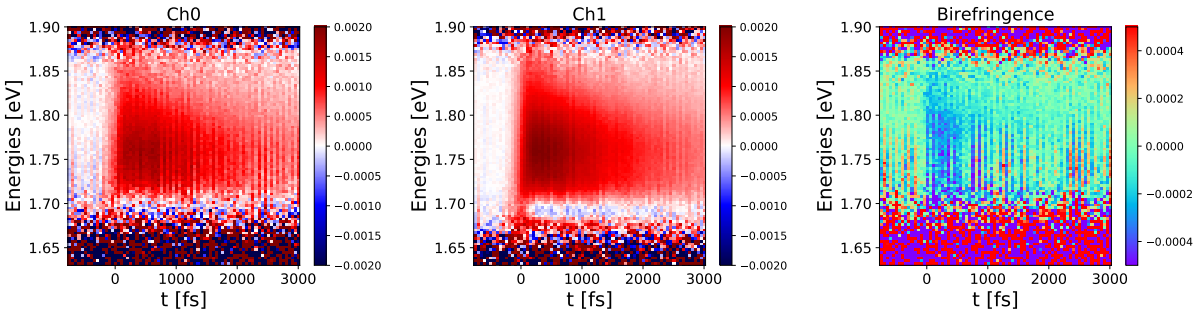

Figure 48: Maps from a birefringence measurement in SC phase, with chirp-corrected probe pulse.

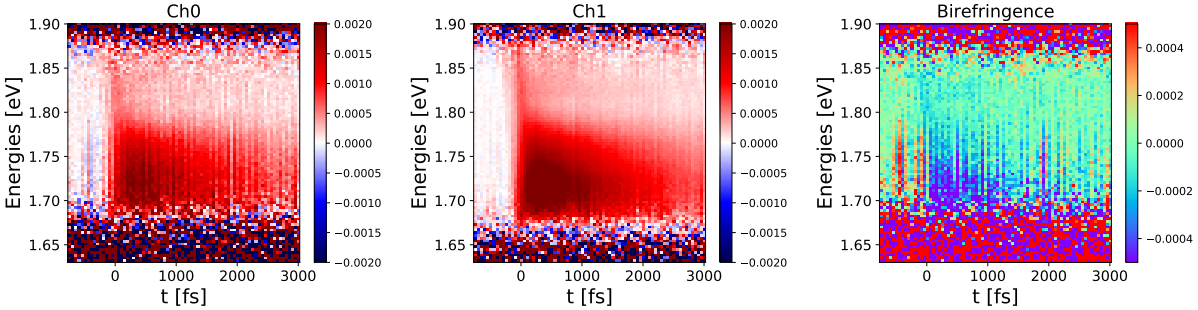

Figure 49: Maps from a birefringence measurement in SC phase, with slightly chirped probe.

By comparing figures 48 and 49, respectively a measurement with a compressed pulse and one where a positive chirp has been applied and the pulse has been dilated of $\sim 250\,\text{fs}$, we can clearly see this change in the signal and how it also affects the birefringence. This raises questions about white-light experiments that will be discussed in section 3.2, and also is consistent with the signal localization that has been observed in past measurements of our group [39], [37], [19].

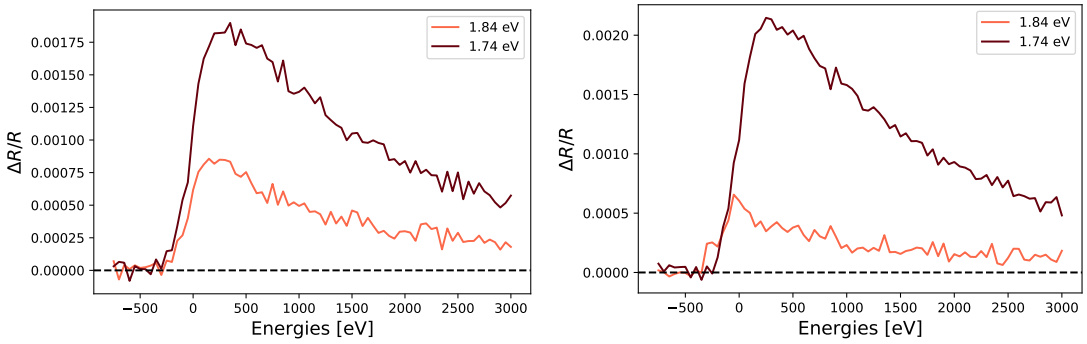

(a) (b)

Figure 50: Cuts at fixed energy for the corrected and chirped measurements, figure (a) and (b) correspond to figure 48 and 49 (middle map) respectively.

From figure 48 and 49 it is possible to see the radical change in the signal, moreover cuts at fixed energy in figure 50a and 50b show that there is a change in the dynamics at the same energies that happens for the two different pulse durations: we can see that the low energy cuts are rather similar between the two maps, while moving 100 meV above the decay dynamics are much faster and different in shape[16].

[16]The shape of the peak remembers in some way what was observed at the same energies for the above-gap excitation.

The effect is present at both 900 nm (see figure 51) and 700 nm, but was mainly investigated at the latter wavelength because it is the one that we used for the FCS experiments. Furthermore, the NOPA has both higher maximum power in this region and a better pulse spectrum.

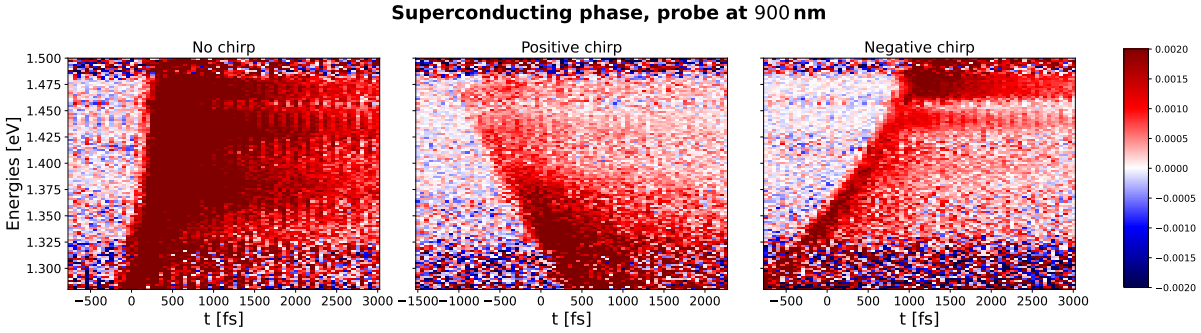

Figure 51: Measurements testing the presence of the chirp effect on the UD88 sample in the superconducting phase with the probe set at 900 nm.

3.1.1 Probe fluence

To comprehend the nature of the phenomenon and its possible perturbative origin we tested its dependence from the probe fluence. Thanks to the SLM we can easily control the intensity of the probe and estimate its fluence (overestimate, as the power meter was put in the optical path before the diamond window). We therefore took measurements with the probe at 700 nm on the UD88 sample at $T = 75\,\mathrm{K}$, gradually decreasing the fluence from its maximum value $\phi_{probe} \sim 4.5\,\mathrm{mJ/cm^2}$ down to $\phi_{probe} \sim 250\,\mu\mathrm{J/cm^2}$; the pulse was slightly positively chirped.

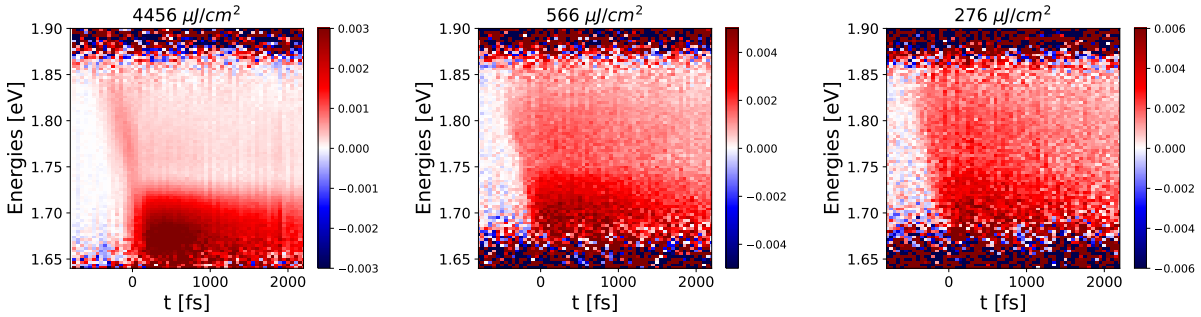

Figure 52: Scan of the probe fluence on the UD88 in the superconducting phase reflectivity measurement with a chirped probe pulse, decreasing fluence from left to right.

In figure 52 we report the full power probe and the two lowest fluence measurements. What can be seen first is a change in the overall intensity of the signal, and the presence of the effect is still clear at $\phi_{probe} \approx 566\,\mu\mathrm{J/cm^2}$; even with the lowest fluence and a lower signal-to-noise ratio the effect is still distinguishable in 53.

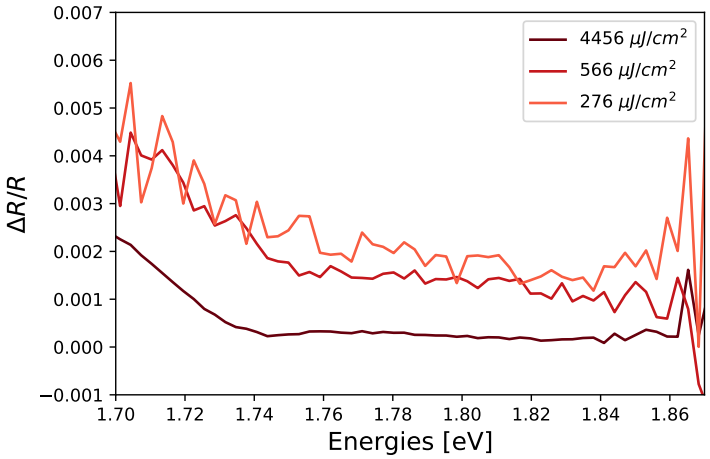

Figure 53: Cut at fixed delay $\Delta t = 500$ of the fluence scan of figure 52. The cut was taken directly on the unprocessed map, since the chirp here is weak and this operation still gives good relative information on the spectral weight.

By observing the value of the map at $\Delta t = 500\,\text{fs}$ (figure 53) we can see the presence of a higher reflectivity in the low frequencies (first frequencies arriving on the sample), even though the effect seems weaker compared to the intensity at the other energies with the other two measurements.

What is important to know is that a probe linearity test was done before these measurements, observing that for the two lowest fluences studied the signal was practically the same, but at the same fluences the chirped probe still generated a different signal. The probe linearity test is reported in Appendix B.

3.1.2 Phase dependence

To understand the nature of the phenomenon, if it is something typical of the superconductive state or not, we first of all repeated the test at $T = 300\,\text{K}$, to exclude the presence of it in the normal phase. The measurement were taken on the UD88 sample at a 700 nm wavelength of the probe.

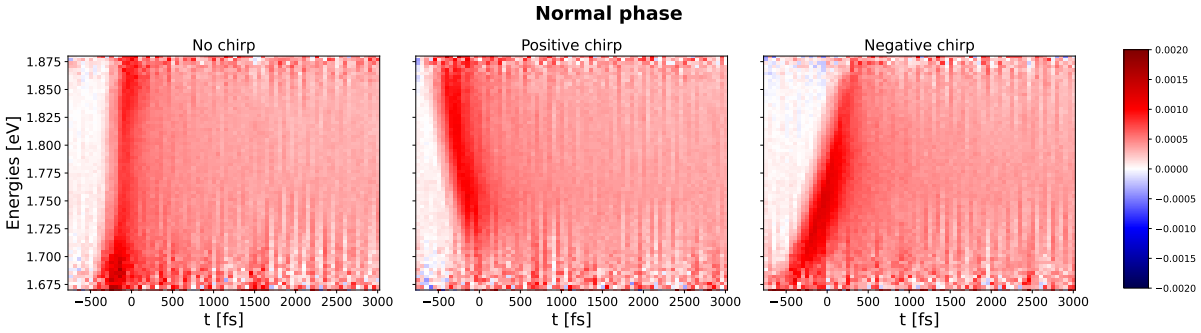

Figure 54: Reflectivity measurements in normal phase ($T = 300\,\text{K}$), in order from left to right: no chirp, positive chirp and negative chirp.

From figures 54 and 55 one can see the effect is not present at room temperature, on the contrary the intensity of the signal seems slightly higher in the last frequencies arriving on the material. The effect was also tested at 900 nm, where subtracting a (corrected in post-processing) chirped measurement to one with the compressed pulse results in a flat map.

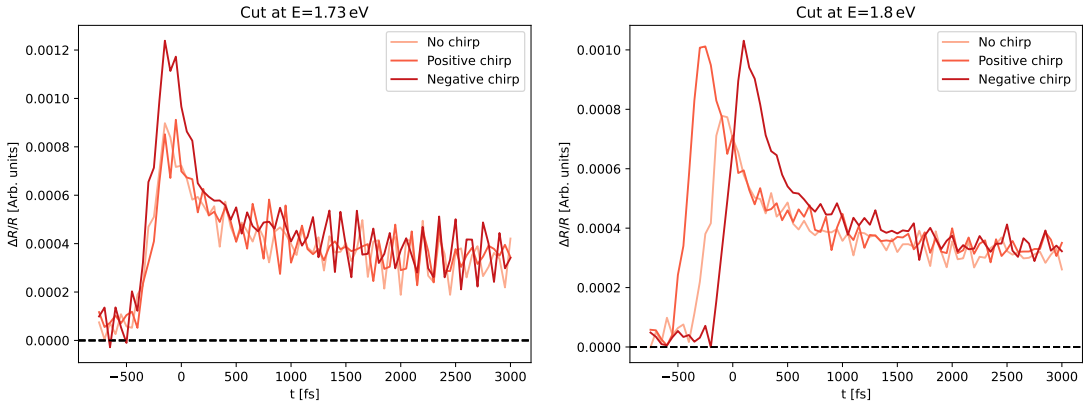

(a) (b)

Figure 55: Cuts at fixed energies (in the titles) of the maps in figure 54, showing no change in the shape of the dynamics apart from the obvious different delays.

The effect was primarily observed and studied in the superconducting phase, so the presence of the effect in the pseudogap phase cannot be stated properly. The measurements taken in this phase seem to suggest a weaker yet present perturbation of the sample, that disappears when the probe intensity is lowered: the negative pseudogap dip is present at the first frequencies arriving for the full fluence (first row of figure 56), while for the reduced fluence (second row of figure 56) it is present at all energies and the shape of the signal does not seem to be affected in any way. But differently from the superconducting measurement the compressed pulse too seems to be affected by the change of fluence.

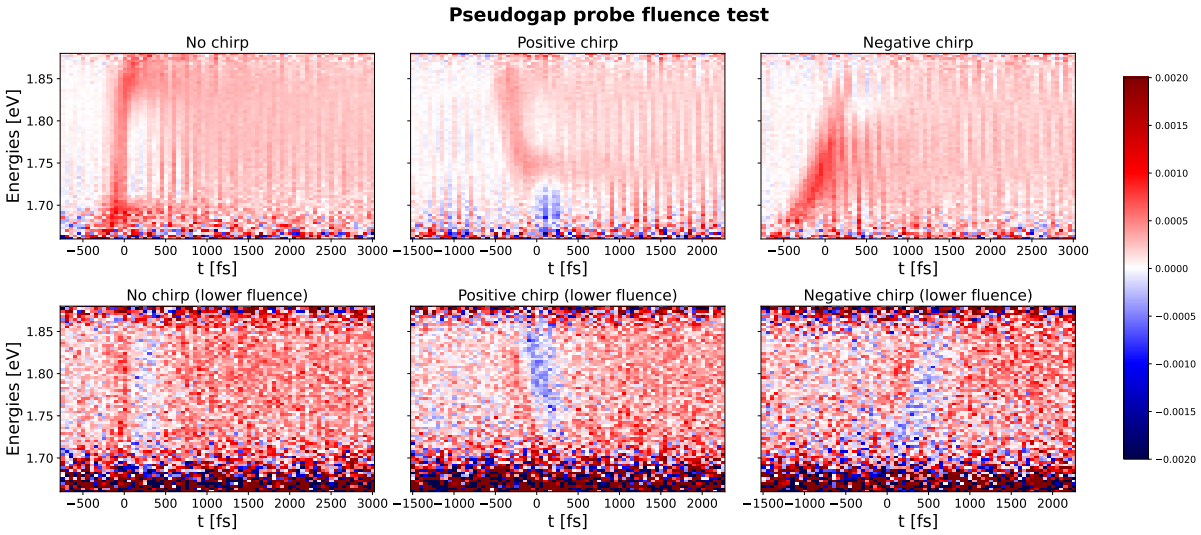

Figure 56: Reflectivity measurements in pseudogap phase ($T = 108\,\mathrm{K}$), in order from left to right: no chirp, positive chirp and negative chirp, while the upper row is with full probe fluence and the lower one is with minimum fluence. In the second row the low fluence gives a bad signal to noise ratio, but the statements of this section can by confirmed by cuts and their integration.

3.1.3 Chirp scan

To explore further the extent of this phenomenon we ran some measurements scanning a set of positive and negative chirp, in the same conditions of the former section. The resulting maximum dilation of the pulse (first and last image of figure 57) is of $\sim 5\,\mathrm{ps}$.

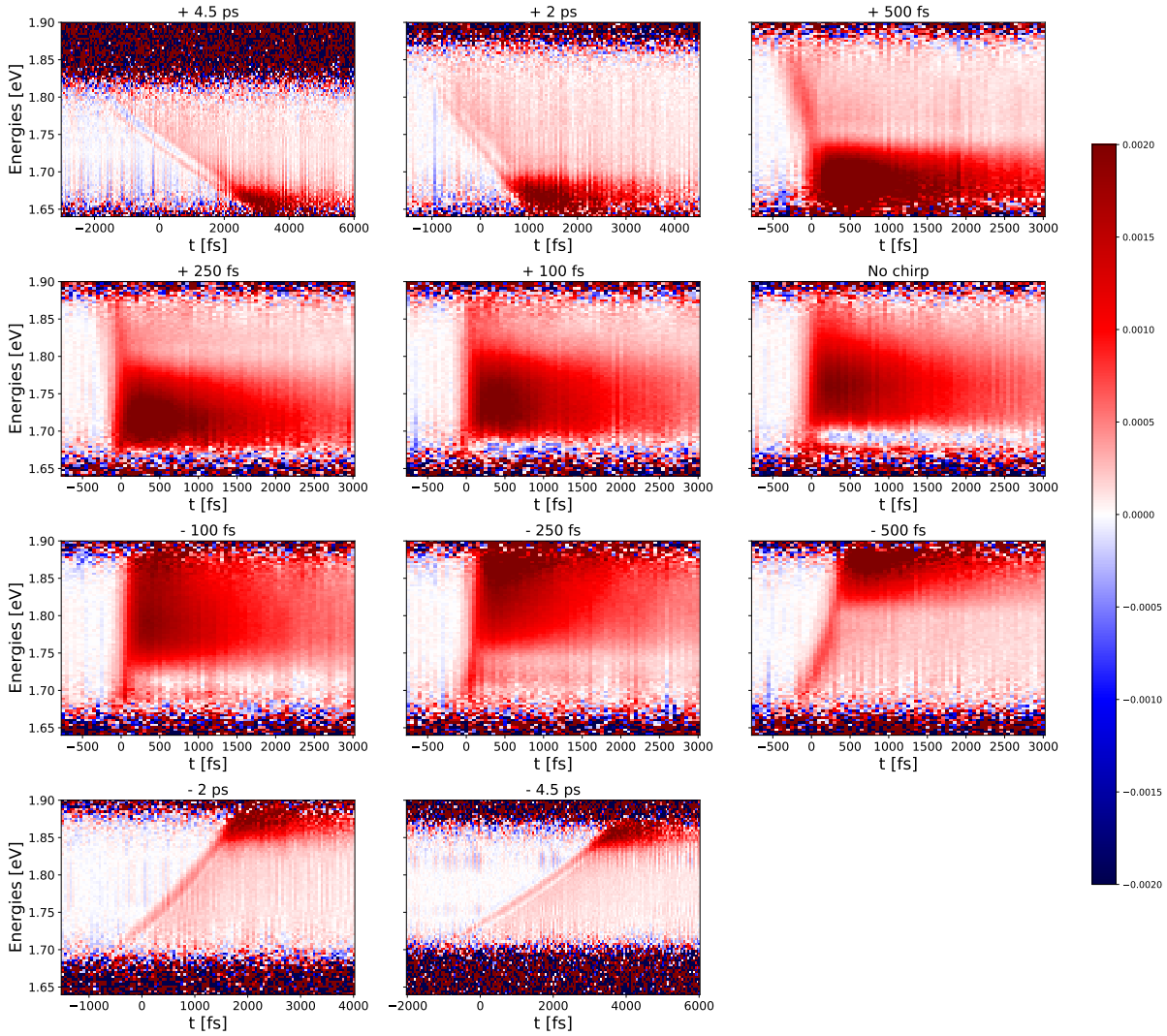

Figure 57: Scan of all the tested chirped probe reflectivity measurements with displayed the resulting added dilated duration of the pulse. The sign of the dilation represents the type of chirp, + for positive and − for negative.

What can be seen is that even a slight chirp affects the spectral weight of the signal: long-lived intense response shifts in the direction of the first frequencies impinging on the sample. Taking the zero-chirp map (left image of the second row of 57) and comparing it to the weaker chirps we can see the increasing shift of the peaks central frequency and also an increase in the maximum intensity of the signal. This clearly emerges by correcting the maps[17] and then plotting a cut at a fixed positive time (see figure 58b).

[17]The added chirp is linear and thus the correction is the simple subtraction of a straight line to the map.

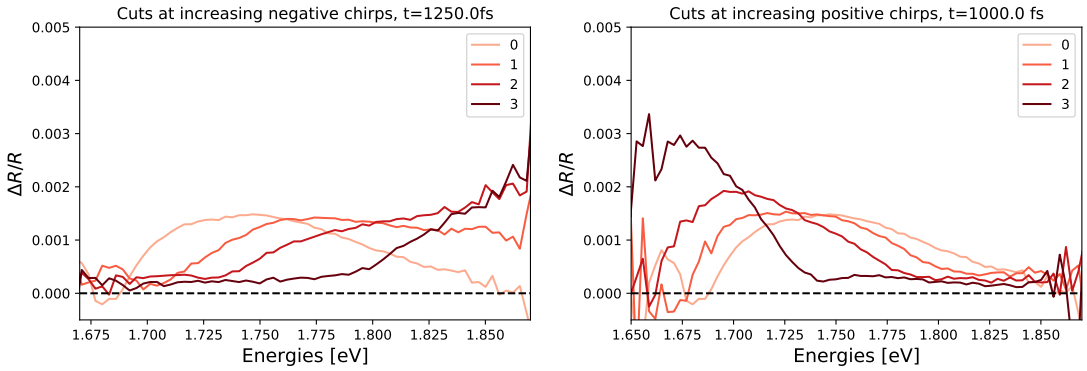

(a) (b)

Figure 58: Cuts at fixed delay $\Delta t = 500\,\text{fs}$ of some of the negatively (figure (a)) and some of the positively (figure (b)) chirped measurements of figure 57. The cut labeled "0" is the compressed one, the increasing label indicates the increasing duration; The resulting spectral weight shift is clearly visible.

It is difficult to state in a quantitative way the shift, but what can be done is consider as the center of the response its weighted sum and to plot it as a function of the chirp, expressed as the delay time between the arrival of two fixed frequencies (arbitrarily chosen), or using the duration of the pulse. This can be done properly only for the chirps that don't completely push the peak outside of the map, and the relation is symmetric for these small chirps. Another remark that must be made is that by conducting the probe fluence study in the compressed pulse configuration (third figure in the second row of figure 57) the zero/negative trace in reflectivity below 1.7 disappears below $\phi_{probe} \sim 560\,\mu\text{J/cm}^2$.
Strong chirps move the intense response to the very edges of the map, what is interesting is the emergence of a short-lived negative dip in the positive signal. We have two observations about this feature:

1. The effect could be dismissed as a pump-probe interference signal (last image of 57), a similar pattern emerges in a test that was done by setting the pump at $10\,\mu$m at a high fluence ($\phi_{pump} \approx 1.3\,m\text{J/cm}^2$). The rippled effect produced in this case is likely should not have anything to do with the condensate as it presents even at room temperature, where we know from 3.1.2 that the effect is not present. Moreover, by dilating the pulse so much through the pulse shaper also the spectral shape results affected, so we cannot exclude as the cause a distorsion of the probe.

2. The negative feature in the extreme positive chirp (first image of 57) closely resembles the signal obtained in the pseudogap phase. This can be observed in the following section's figures.

3.1.4 Doping dependence

The previous tests were all performed on the UD88 sample,and even though it was clear that the effect was present in all samples at full probe fluence, we repeated the probe fluence measurements on the OP95 and OD91 samples, to study the possible doping dependence of the chirp response. The same chirp of figure 53 was applied in all measurements.

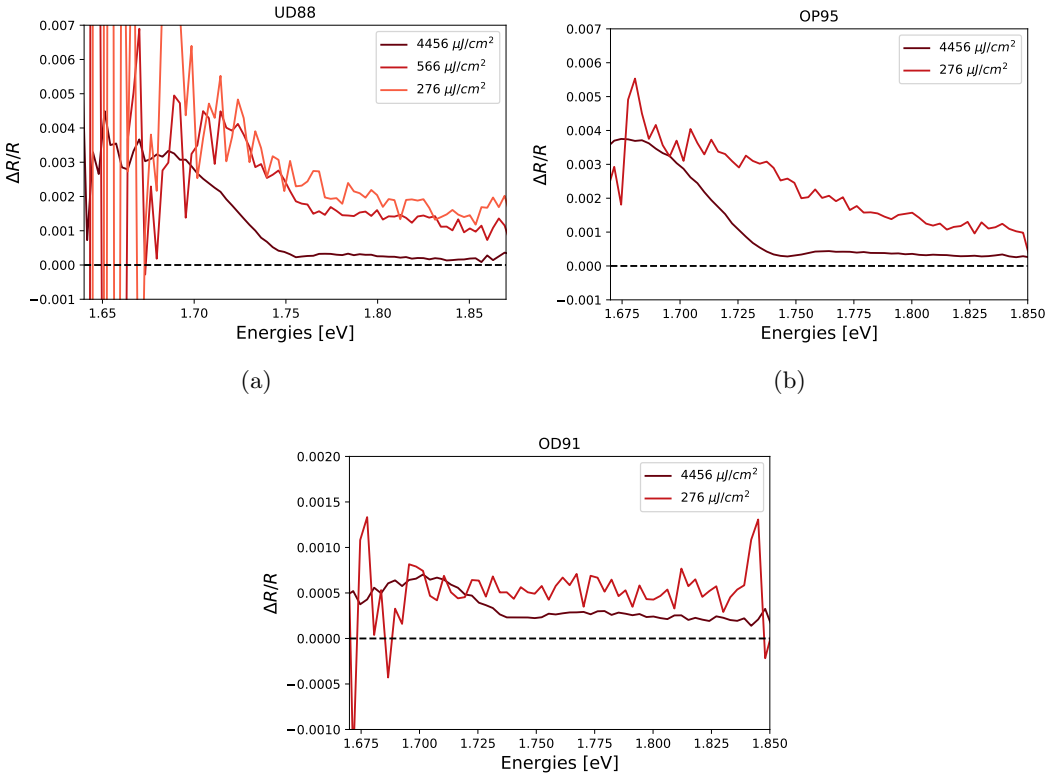

Figure 59: Cuts at fixed delay $\Delta t = 500\,\text{fs}$ of the fluence scans on different samples.

By comparing figures 59a, 59b and 59c we can observe that the effect is noticeably affected by the growing doping. At high fluence the effect is present in all the samples, but it seems that the peak is blue-shifted by the increased doping; at low fluence the spectral weight of the signal is less affected by the chirp with the increase of the doping, at the point that for the OD91 sample the signal shows the same intensity at all energies.

3.2 Discussion

Acknowledging the effect of the chirped probe on the response of the material allows us to reread all the white-light measurements made on this cuprate (e.g., figure 60): some of the intense long lived signal localized at low energies might be influenced by the fact that the supercontinuum pulse is positively chirped. The probe fluence in this case might be low enough to avoid strong radical effects, and as a matter of fact we see signal also at higher energies, while in the tests with the 700 nm probe we don't.

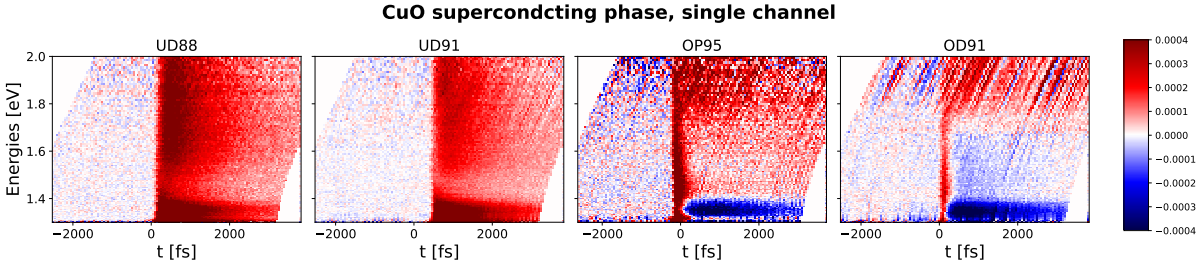

Figure 60: Chirp-corrected white-light reflectivity maps for all the samples in superconducting state, with pump polarization parallel to the *CuO* direction.

Before thinking of the different possible causes and properties of the effect, we must remember that the compressed probe is in a linear regime at the tested fluences.

- **Timescale of the phenomenon:** By observing the time interval Δt_c between the instant t_1 of the arrival of the first frequency and the instant t_2 after which the long-lived signal disappears we might understand if there is a "critical duration" for the process. For the strong chirps at full probe fluence we get $\sim 500\,\text{fs}$ interval, but the time interval for the small chirps is much shorter. As observed in the fluence study also the intensity of the probe plays a role, so it could be that there is a dependence on the amount of energy delivered in the duration of the pulse.

  The explanation through a critical amount of energy delivered could fit, but the long-lived signal does not seem to start and then be truncated, as stated before *it shifts* to the first frequencies arriving.

- **Existence of the phenomenon in the pseudogap phase:** the perturbation of phase coherence could be considered as part of the problem, but this hypothesis would be excluded by the existence of the effect in pseudogap phase[18], rather suggesting an action on the pairing mechanism itself. The chirped probe has an effect in this state when used at full fluence, but the compressed pulse itself changes at different fluences 56.

- **Doping dependence:** the effect seems to be stronger both in shift and critical probe fluence at lower doping. If the effect is caused by a disruption of the superconducting condensate this could be linked to the coherence length of the Cooper pairs at different doping.

- **Electronic modes:** the effect presents both for the B_{1g} and B_{2g} experimental configurations and the localization of the signal survives in the birefringence and thus influences also the electronic modes.

The phenomenon is clearly connected to the existence of the condensate, changing visibly the optical response of the samples even for low probe fluences. It is hard to state if the chirp causes a disruption of the condensate and through what mechanism could it do this. One thing that is clear is that the interaction with a chirped probe does affect the state of the sample, so the "probe-and-correct" paradigm that has been used in supercontinuum probe measurements (justified by [36]) is to be used with caution with material that show strong correlations: a future experimental effort could be directed to the compression of a white-light pulse, to repeat the experiments, though it is possible that for the fluence of the white-light probe the effect could be not that significant.

[18] Above T_c phase fluctuation should destroy long range coherence properties of the material.

4 Femtosecond covariance spectroscopy of BSCCO

The following section will be focused on time-resolved measurement of Raman spectra of Y-BSCCO using the novel technique of Femtosecond Covariance Spectroscopy. In the first two parts we will show a brief history of Raman spectroscopies on cuprates (including time-resolved experiments) and then the working principles of Femtosecond Covariance Spectroscopy, describing its potential in both static and time-resolved applications. In the last part we will apply the technique to our samples in different phases, measuring the signal dependence from temperature; after the discussion of our observation, a sketched phase diagram obtained from the measurement in this thesis is shown (figure 93).

4.1 Time-resolved Raman spectroscopy on cuprates

Studies of Raman spectroscopy of unconventional superconductors can access directly to the B_{1g} and B_{2g} modes of cuprates in the superconducting state and have led to the first suggestions of symmetry of the superconducting gap in cuprates ([40], [41],), such as the shift in frequency between the two modes and the scaling of the two at low frequencies, both visible in figure 61a.

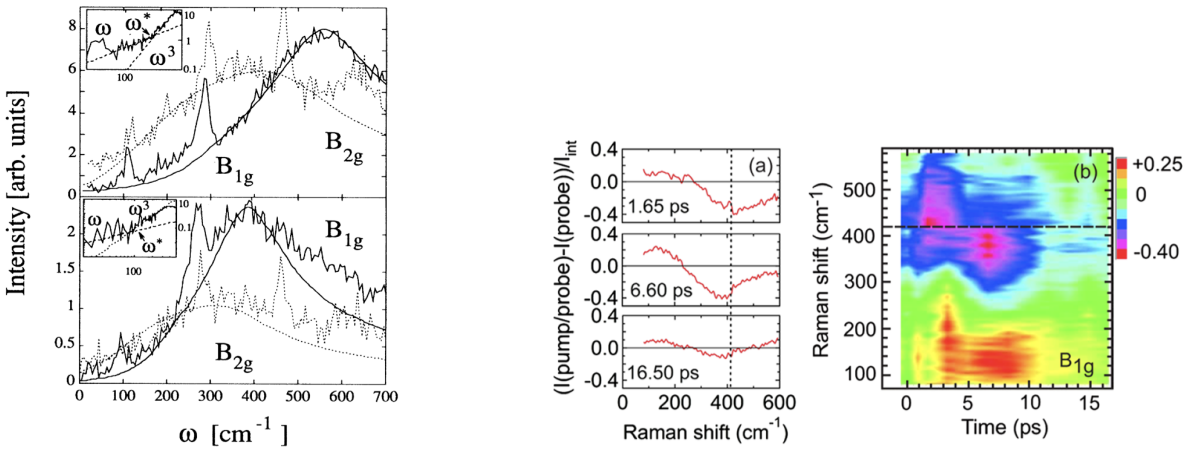

Figure 61: Raman spectroscopies of BSCCO in SC phase. In figure (a), taken from [41], B_{1g} and B_{2g} equilibrium spectra for two different level of doping. In figure (b), taken from [42], the time-resolved study

Like was mentioned before the dynamic study of Raman excitations has intrinsic limitations on its time and frequency resolutions, forcing to a compromise. The first time-resolved experiment by *Saichu et al.* [42], with a $\sim 0.9\,\mathrm{ps}$ time resolution allowed the observation of the B_{1g} mode dynamics, showing the depletion of the pair breaking peak (negative signal at higher energies in figure 61b) followed after a picosecond by an increase in quasi-particle spectral weight (positive signal at lower energies in figure 61b) that they associated to a loss of Cooper pairs caused by the pump pulse.

The FCS time resolution allows to investigate faster dynamics, such as the ones of hole-phonon coupling.

4.2 Theoretical introduction to FCS

Raman spectroscopy is a very useful tool to gain insight on the excitations that are generated in the complex condensed matter systems. One can use this technique to obtain information on the dynamics of such processes, but for every approach there is a trade-off: to have a good frequency resolution one must use a very narrow frequency pulse, which means that the pulse

must have a long duration due to the uncertainty principle. Another important factor to obtain reliable results in both static and dynamic measurements is to have a very good stability in the light source and the experimental setup. Noise, originating even from the detection, is an enemy that every scientist has to deal with, usually by averaging the data over numerous repetition; the pulse-to-pulse consistency of the source becomes a must in ultrafast spectroscopy to obtain a mean value signal.

By using a different approach and embracing random noise as a tool and not as a nuisance the Q4Q team has managed over the years to refine a different experimental paradigm: *Femtosecond covariance spectroscopy (FCS)* or *Noise correlation spectroscopy (NCS)* is a technique that can obtain (time-resolved) Raman scattering information-in particular the use of ultrafast pulses makes this an Impulsive Raman Scattering (ISRS) technique-through the use of spectrally noisy probe pulses and study of the covariance of the recorded signal ([43–45]).

As will be explained in detail, through the FCS approach one can use broadband probe pulses with stochastic fluctuations in their spectrum to recover information not from the mean value of the signal, but from the multimode spectral correlations. By handling the spectral information in this way the frequency resolution of the experiment is not affected by the width of the band, but by the correlation length of the pulse frequencies at the detection (this will be explained in 4.2.4), **effectively disentangling time and frequency resolution**.

The trade-off in this case comes from the great number of times that the process has to be repeated to obtain a relevant dataset, due to its statistical nature in which every repetition is an experiment on its own.

In this part of the section section we will introduce the theoretical structure of the technique, the experimental apparatus used to introduce noise in the pulses and the analysis of this type of information, extending then the formalism to time-resolved experiments; the second part will be dedicated to the study of the electronic excitations dynamics in $Y - Bi_2Sr_2Ca_{0.92}Cu_2O_{\delta+8}$ through *Femtosecond Covariance Spectroscopy*, with our objective being monitoring their evolution at different dopings and across their phases.

4.2.1 Basic principles of FCS

The paradigm of FCS is to obtain statistical information from covariance rather then from averaged measurements as in most of the spectroscopy techniques, which has also the advantage of revealing multimode correlations imprinted by nonlinear light-matter interaction on broadband pulses. In such experiments one must regard every pulse as a different experiment, making pulse to pulse stability-a fundamental requirement for average value measurements-detrimental to the process, as every feature in the incident pulse evolves in a correlated signal in the transmitted spectrum (see figure 62b). To this end one must eliminate the coherence of the probe, that would otherwise drown the weaker correlation signal, by introducing spectrally narrow stochastic fluctuations in the pulse spectrum. Furthermore any averaging process on the pulses must be avoided, as it would cancel precious statical information. This means that also in the detection step a shot by shot acquisition has to be used.

The introduction of fluctuations in the pulses is done through an SLM based pulse shaper, the working principles of which will be introduced in section 4.2.3. The nature of the fluctuations and their effects on our correlation observables will then be discussed, along with our data analysis procedures. Before diving into the technical details of the technique, we must introduce the Impulsive Stimulated Raman Scattering (ISRS) process, which is the dominant Raman process that occurs in the interaction of an ultrafast pulse with a material.

4.2.2 Impulsive Stimulated Raman Scattering and noise correlation

We have already given an introduction to Raman processes in the perspective of the birefringence experiments, but it is quite useful to reintroduce them in a way more oriented to the FCS, also explaining what *impulsive* means in this context.

In the approach of Raman spectroscopy what we measure are energy differences: following the model of figure 11 and in figure 62a, when a photon at frequency ω interacts with the material it can either be re-emitted at a lower frequency $\omega - \Omega$ or at a higher frequency $\omega + \Omega$, respectively what happens when an excitation Ω is created, in what is called a *Stokes process*, or when a new excitation is destroyed, which is called an *anti-Stokes process*. In Stimulated Raman Scattering the material interacts with two electromagnetic fields at frequencies ω_1 and ω_2 such that $|\omega_1 - \omega_2| = \Omega$, amplifying through this resonant condition the otherwise weak spontaneous process (which is now a stimulated process).

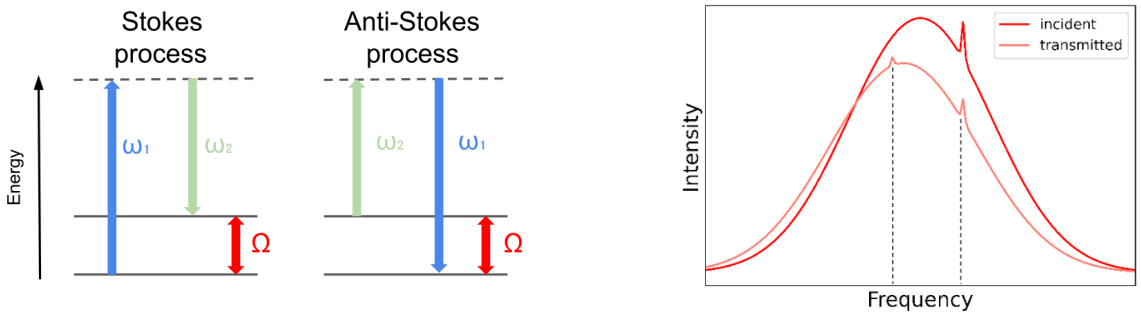

(a) (b)

Figure 62: In figure (a) are represented the Stokes and Anti-Stokes processes of Raman scattering, in figure (b) the effect of this processes on a pulse that interacts with the material; notice how the presence of a spiked feature on the incident pulse affects the transmitted pulse, generating two features at distance Ω: this principle is the origin of FCS. Figure (b) is taken from [19]

When a femtosecond pulse passes through a Raman active material the interaction produces excitations *coherently* (i.e. excitations in phase) [46]. The bandwidth of femtosecond pulses is large enough[19] to contain both the ω_1 and ω_2, and many other frequency couples that match the condition $|\omega_1 - \omega_2| = \Omega$. The field of the pulse is therefore enough to produce the stimulated Raman process.

Using femtosecond pulses results in ISRS dominating the light-matter interaction, and if all the frequencies in the pulse interact this way the transmitted pulse will result shifted with respect to the original, as shown in figure 62b. The Raman scattering information cannot be recovered directly from this shift, as it depends not only on the excitation's frequency, but also on the cross section of the process. If the incident pulse, however, contains a distinguishable feature, the transmitted pulse will show trace of this feature at the original frequency and at the scattered one. This is, as mentioned in the previous section, the working principle of FCS: if a peaked fluctuation is embedded in a Gaussian pulse at frequency ω, the detected pulse will show the effects of this feature also at $\omega \pm \Omega$; if the experiment is repeated many times with different fluctuations then the information of the Raman scattering can be recovered by the multimode correlations between frequencies established by the ISRS process itself. By extending the idea to every frequency in the pulse we get *Noise Correlation Spectroscopy* or *Femtosecond Covariance Spectroscopy*: a complete Raman spectrum can be recovered from the covariance study of a

[19] e.g. phonons have a vibrational period usually shorter than the duration of the pulse, therefore the bandwidth naturally exceeds the excitation frequency.

signal obtained by embedding stochastic fluctuations[20] at all the frequencies in the probe pulse bandwidth.

Without going too much in the detail on the quantum model and the calculations that show how this concept actually works ([43,47]), we will explain how noise is introduced in the probe pulse and how to recover the correlation information.

4.2.3 Pulse shaping

To understand FCS it is important to show how the pulse can be manipulated to introduce stochastic fluctuations, which is the most fundamental concept to the technique; this can be done through pulse shaping architectures, which are optical tools that allow us to tailor the pulse duration, chirp, or overall waveform both in the time and frequency domains. The *pulse shaper* component of our setup is based on a liquid crystal spatial light modulator (LC-SLM), but other architectures are possible and have been tested [19].

The pulse shaper of our setup operates in the Fourier domain[21] using the so called *4f line* scheme (see figure 63): the beam passes through a diffraction grating and then a lens, spatially separating the spectral components of the pulse and focusing them on a diffraction limited spot on the Fourier plane. At this point a spatial mask can be used to manipulate all the spectral components independently; the mask can be made (usually through litography) to perfectly fit the shaping requirements, but this configuration limits the system to a single shaping task; to have multitasking setup one must use a dynamic, programmable mask, such as the SLM. After the interaction the pulse then passes through another lens and diffraction grating, recombining the components in the now shaped pulse; every component of such architecture has to be at distance f, the focal length of the lens, and for this reason it is called *4f line*.

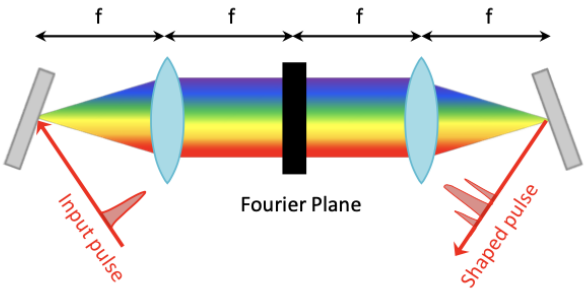

Figure 63: The general configuration of a *4f line* scheme. The choice of the optical component in the Fourier plane dictates the properties of the shaper, in our case it is the SLM.

The SLM is a matrix of pixels consisting in a layer of nematic crystals sandwiched between electrodes (these electrodes are pixelated, the liquid crystal are continuous), the light goes through them and gets reflected back by a dielectric mirror[22], as shown in figure 64. When no voltage is applied the crystals exhibit the maximal birefringence i.e. the difference between the refractive index along the extraordinary (n_e) and ordinary (n_o) axis; by controlling the voltage through the electrodes the crystals can be rotated, modifying $\Delta n = n_e - n_o$ in a controlled way and introducing a phase delay

$$\Delta\phi = \frac{\omega \Delta n(V,\omega) D}{c},$$

[20] The fluctuations can be either in the phase or in the amplitude.

[21] Other pulse shapers do operate in the temporal domain, e.g. acousto-optic modulator (AOM) and electro-optic modulators (EOM).

[22] So in this case the *4f line* uses the same lens and grating to recombine the pulse.

where ω is the frequency of the light impinging on the pixel, V is the applied voltage, D is the thickness of the liquid crystal and c is the speed of light.

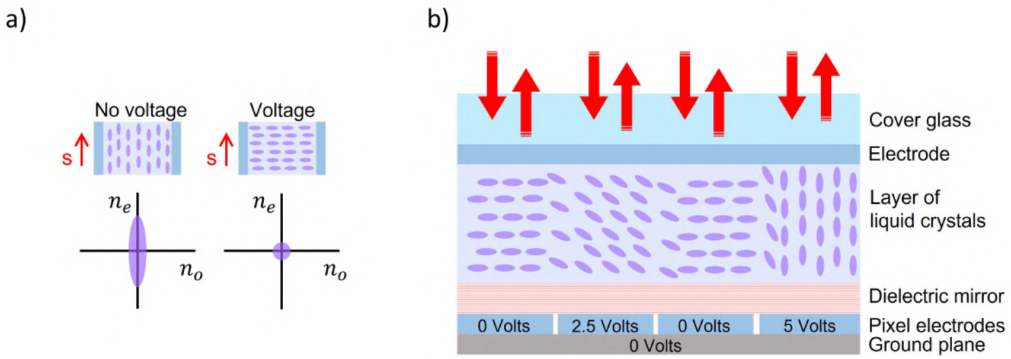

Figure 64: SLM working principle. A layer of nematic liquid crystals is placed in between two electrodes, and it is possible to control their orientation and hence the birefringence of the layer. By applying different voltages, every pixel can convey a different Δn and cause a controlled phase delay. Taken from [39].

The phase control can be directly obtained by a single row of pixels, but the spectral amplitude is not so easy to control; to have full tunability on the amplitude a 2D mask in a diffraction geometry scheme must be used. The voltages are controlled in a way that every pixel column (if we think of the light as dispersed horizontally) generates an effective blazed grating for every spectral component, and then we must select the first order beam diffracted by the mask. The phase modulation $\phi(\omega, y)$ produced along a pixel column (thus for a fixed ω) can be expressed as (figure 65, right):

$$\phi(\omega, y) = \alpha \left[\frac{1}{2} + A(\omega) S_d(\psi(\omega), y) \right], \tag{23}$$

where α is the maximum phase shift achievable with the specific SLM used, S_d is a normalized sawtooth function, $A(\omega)$ is the amplitude of the sawtooth and $\psi(\omega)$ is its phase. According to Fraunhofer diffraction the resulting first-order diffraction beam is:

$$E(\omega) \propto e^{-i\psi(\omega)} sinc \left[\pi - \frac{\alpha}{2} A(\omega) \right] \tag{24}$$

Equation 24 shows how in this configuration one can control both the phase and the amplitude of the spectral components of the pulse by adjusting the parameters $\psi(\omega)$ and $A(\omega)$.

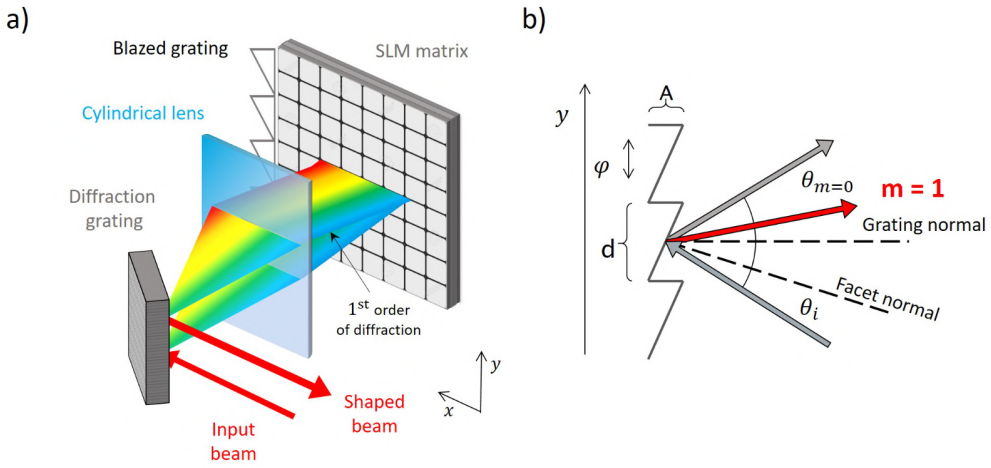

Figure 65: How the SLM can be used to modulate the spectral amplitude through diffraction geometry. Changing the voltage at the electrodes of the 2D SLM pixel matrix allows to create an effective grating profile along every pixel column, resulting in the full control over first order of diffraction beam. Taken form [39].

To calibrate the SLM a narrow sawtooth gratings pattern is applied to it and the beam coming out of the pulse shaper is focused in a spectrometer, where the resulting comb-like signal allows to associate every pixel of the SLM to a specific frequency in the pulse; the conclusive step is then using the SLM to create a map between the SLM pixels and detector pixels by scanning the SLM horizontally with a single narrow diffraction grating [43].

4.2.4 Stochastic fluctuations and noise configuration

From the last explanation one can now see how noise is introduced in experiments: 1920 random numbers are generated[23] and used to modulate the amplitude $A(\omega)$ (or the phase $\psi(\omega)$) of the grating and, as a consequence, the diffraction efficiency. The spectral amplitude of the different components in the pulse will thus result randomized. Since there is an intrinsic coupling between neighboring pixels a Gaussian-smoothing of the random values array is performed, causing a finite correlation length between the pixels. The correlation length between pixels thus depends on the FWHM of the smoothing function used. In our case the correlation length is 5 pixel, which for our setup means correlation in the pulse across a $\sim 1\,\text{nm}$ wavelength, and this number defines our frequency resolution. To observe the correlations emerge from a sample one must obtain a dataset resulting from many repetition with different randomized patterns, this is what sets the upper bound for the time needed to do a measurement: the slow[24] refresh rate of the SLM (200 Hz, in the end the actual speed of our procedures lowers it to 60 Hz) and the generation time of the random numbers causes more than 20 pulses to have the same pattern and convey the same statistical information, so only one of them or their average will be considered. In our experiment the number of different patterns that were sent to the SLM and on which the correlators were calculated[25] was 120000. This is the main limitation of the technique, causing a time-resolved measurement to last many hours. An acousto-optic modulator based pulse-shaper could allow to make way faster measurements, completely avoiding these limitations and raising the maximum repetition rate of the experiment to 30 KHz [19].

The last consideration concerning the noise introduction in the sample is the choice of

[23] Pixels in a row of the SLM matrix.

[24] Slow with respect with to the 5 KHz repetition rate at which operates the laser source during these experiments.

[25] The correlators were calculated on small batches of the total pulses, which were then averaged

noise configuration. Until now we have talked of introducing noise in the whole spectrum (*full modulation*) of the pulse, but this is not the most effective choice for the modulation, as the resulting correlations are present but relatively low. Other configurations have been tested by former members of our group [43] on an α-quartz sample, for example by introducing noise only in half of the spectrum and either leaving the other half coherent (*partial modulation*) or by setting it to zero amplitude (*mean value shaping*), as shown in figure 66. What has been observed is that the heterodyne amplification of the signal benefits from the presence of coherent spectral components. In other words, the visibility of the correlation signal is enhanced by partial modulation, as will be shown in figure 69.

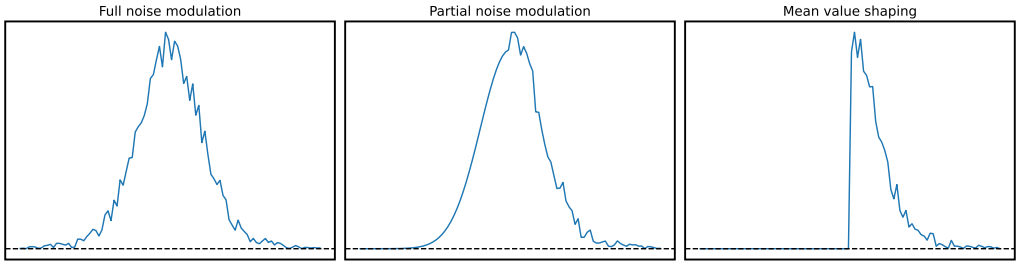

Figure 66: Simulation of the three different noise modulations used in past FCS tests.

4.2.5 Correlation signal

The detected intensities $I(\omega)$ are then processed to quantify the multimode correlation between the spectral components, and the statistical object we use for this is the *Pearson correlation coefficient*:

$$\rho(\omega_1, \omega_2) = \frac{\langle I(\omega_1) I(\omega_2) \rangle - \langle I(\omega_1) \rangle \langle I(\omega_2) \rangle}{\sigma_1 \sigma_2}, \tag{25}$$

where the $\langle \dots \rangle$ indicate the average over the dataset of measurements (in which every pulse has different stochastic fluctuations), and σ_1, σ_2 are the standard deviations of the respective intensities over the same dataset. This coefficient is a normalized covariance expression commonly used to evaluate the linear correlation between two variables, ranging from a value of 1 for perfect correlation to -1 for a perfect anti-correlation; the calculation done by considering $I(\omega_1)$ and $I(\omega_2)$ from the same pulse gives the so called *auto-correlator*. The results of of this analysis are plotted in a 2D map that quantifies the correlation for each couple of frequencies, a so called *Pearson map*. Different types of fluctuations affect the correlation signal like it is shown in figure 67; of these the most relevant in our case is the one where random noise was added to the spectral amplitude, which shows zero correlation between different frequencies on average.

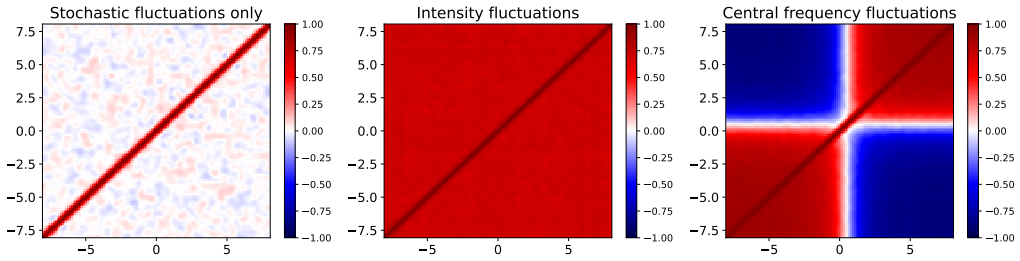

Figure 67: The Pearson maps resulting from a dataset with no correlations (on the left), one where there are random amplitude fluctuations (central) and one with fluctuations of the central frequency (on the right).

The common feature of all this maps is that they are symmetric with respect to the diagonal

(due to the definition of correlation) and that the diagonal is always at maximum correlation (every frequency is correlated to itself); the width of the diagonal depends on the level of correlation between neighboring pixels, as be explained in section 4.2.4.

The existence of a Raman interaction affects the correlation maps by **creating features at a frequency distance from the diagonal equal to the frequency of that specific excitation**. This is demonstrated in a clear way in the α-quartz experiments in [43], where the phonon modes of the material manifest as bands parallel to the diagonal of the Pearson map, like in the simulation in figure 68 and by the measurements in figure 69.

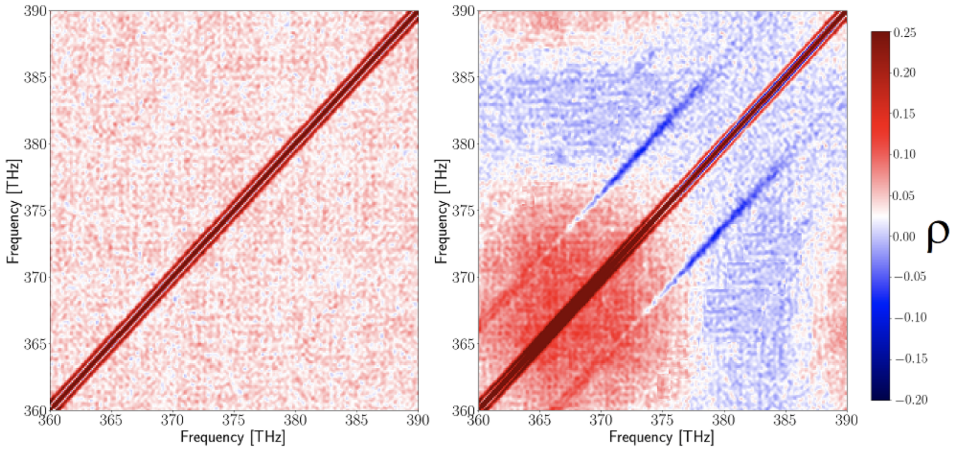

Figure 68: Pearson maps for a transmission FCS experiment on a Raman active material, showing the uncorrelated incident beam and the diagonal feature in the transmitted appearing at the Raman excitation frequency. Taken from [43].

4.2.6 Data analysis

The result of an FCS measurement can be represented as a Pearson map, but it is hard to interpret this kind of information. To make it more comprehensible we take marginals of the maps: since a correlation appears as a diagonal feature we can integrate along the diagonal and express this quantity as a function of the frequency shift from the diagonal. When the experiment is in the partial noise configuration the only regions considered are the mixed ones, i.e. the regions where one of the ω_1, ω_2 variables is in the noisy part of the spectrum and the other is in the coherent part. In figure 69 an experiment with partial noise modulation on α-*quartz* and the relative marginal are shown.

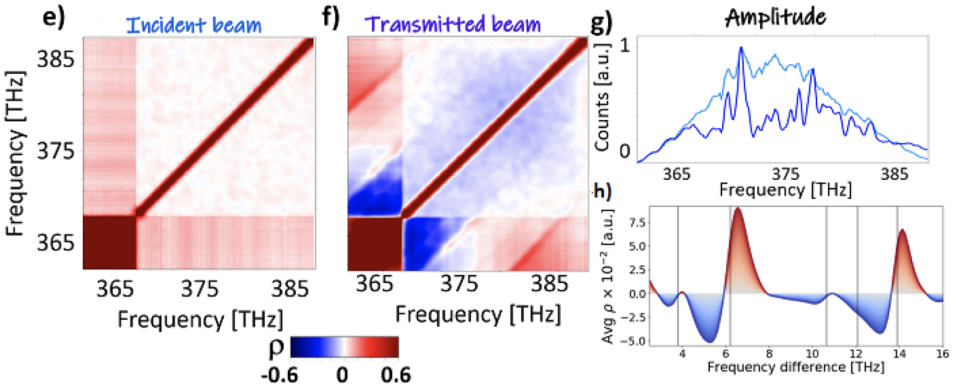

Figure 69: Results for an FCS experiment in partial noise configuration on α-*quartz*: e) and f) are the respectively the incident and transmitted beam Pearson maps, g) is the amplitude of the noisy beam (light blue is reference and dark blue is transmitted) and h) is the marginal of the mixed regions. Taken from [43].

Up to now, we observed the technique as a tool for equilibrium measurements, but what interests us is that it can be applied in a time-resolved experiment, as demonstrated in [45].

4.2.7 Time-resolved experiments and cross-correlation

The data analysis procedures shown can be done for every delay step in a time-resolved experiment and can be put together to create a map that shows the dynamics of the excitations, but first one must subtract the static correlation map (in our terms, *unpumped*) to the pumped signal. The whole process, from acquisition to the differential correlation calculation, is represented in figure 70.

Another important concept that must be introduced is related to the acquisition of the experiment, which is different from that of [43], both in the static and time-resolved measurements. In that setup a part of the noisy probe was deviated by a beam splitter before the sample and used as a reference. In our present setup the probe is split by a polarizing beam splitter after the sample (See Section 1.4 and figure 9) to separate the main polarization ($\parallel$ to the probe polarization) and the residual ($\perp$ to the probe polarization). In this configuration we can discriminate events polarization-wise, by using the cross-correlator between the two channels rather then the already mentioned auto-correlator: this should allow us to isolate the signal relative to the B_{1g} or B_{2g}, according to the chosen probe polarization.

$$\mathrm{CrossCorr}(\omega_1, \omega_2) = \frac{\langle I_{\mathrm{Main}}(\omega_1) I_{\mathrm{Res}}(\omega_2)\rangle - \langle I_{\mathrm{Main}}(\omega_1)\rangle \langle I_{\mathrm{Res}}(\omega_2)\rangle}{\sigma_{\mathrm{Main}}(\omega_1)\, \sigma_{\mathrm{Res}}(\omega_2)}. \tag{26}$$

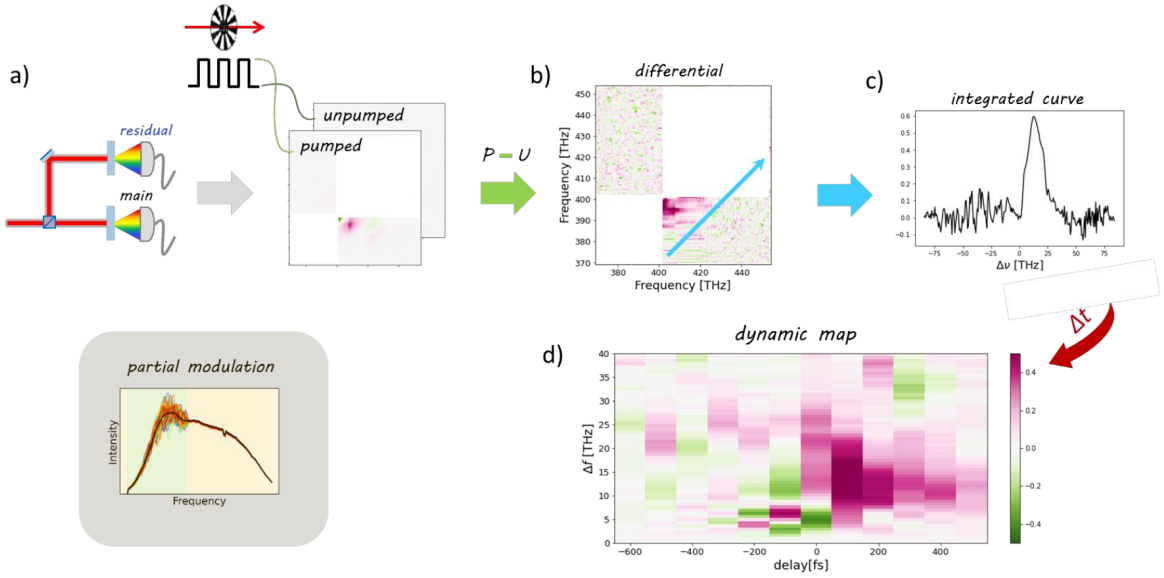

Figure 70: Processing of the dynamic FCS maps. We measure the cross-correlation (main vs residual polarization) maps for both the pumped and the unpumped data (a). The differential maps (b) are then integrated along the diagonals. We obtain an integrated trace (c) for each pump-probe delay Δt. We assemble them in a dynamic map (d) where the correlation signal is a function of the frequency shift from the main diagonal Δf and of the pulses delay Δt. When the pump-probe FCS experiment is performed with partial noise modulation, only the mixed quadrants have to be considered. Taken from [19].

4.3 Measurements on Y-BSSCO across the superconducting and pseudogap phases

As explained before, FCS allows for both high frequency and and time resolution measurements, making it possible to access the sub-picosecond Raman scattering dynamics with sub-THz resolution. The rest of this section is therefore dedicated to the results obtained by doing time-resolved measurements of FCS on the cuprate samples that have been characterized in the previous sections. The pump is set to a wavelength of $10\,\mu$m and a fluence of 12.7mJ/cm^2 (5 mW in figure 71); the high fluence is chosen to maximize the dynamic correlation signal (see figure 71). The system is thus in a highly nonlinear regime.

Figure 71: Marginal signal at the overlap for different fluences for optimally doped sample in the superconducting state ($T = 36\,\mathrm{K}$). The labels indicate the average reading with the powermeter, that can be easily converted to fluence knowing beam diameter and repetition rate.

The probe was set at 700 nm, and all the samples showed correlation signal at this wavelength, similar to the preliminary measurements on BSCCO made by our team in the past ([19]). Tests at 900 nm didn't show any clear correlation.

The noise configuration chosen for the probe was a *partial modulation of the low frequencies*, to have the heterodyning from the coherent part of the signal (so the analysis is on the mixed quadrants). The choice of the lower half of the frequencies was due once again to past measurements that showed no signal for the noisy high frequency configuration, which was attributed to the localization of the birefringence signal at low energies. New tests showed similar results, as shown and discussed in Appendix D.

To try to isolate the B_{1g} (B_{2g}) electronic mode both the pump and the probe polarization are oriented parallel to the CuO (CuCu) direction, while the detection measures both the main polarization ($\parallel$) and its residual ($\perp$). The signal is then processed, as the modes are obtained by calculating the cross-correlators between the two polarizations. To verify that some difference is present we compared the result to autocorrelation maps, basically obtaining identical maps. The method thus **cannot properly isolate the two different modes** (see appendix C for the comparison). The two different configurations still convey distinct information on the B_{1g}/B_{2g} modes mixed to the A_{1g} mode signal. We will thus refer to B_{1g}/B_{2g} only to address the respective experimental configuration.

4.3.1 Superconducting phase measurements

For both configurations the measurements in superconducting state were taken at similar temperature, T$\sim$ 36 K, and almost every measurement was taken in a delay range of $[-400, 700]$ fs at 100 fs intervals. The resulting dynamic correlation maps (obtained as described in 4.2.6 and figure 70) for the four samples are displayed in figures 72 and 73. For both the configurations a positive correlation signal emerges at frequencies between $\sim 7 - 30$ THz, while the lower frequencies show a negative correlation signal that might be related to the "coherent artefact" already observed in [45], as matter of fact similar fringes in the low energy spectrum do appear both at positive and negative times. Measurements on the UD88 sample in B_{2g} configuration could be fitted[26] with a double exponential convoluted with a Gaussian curve (to account for

[26]Due to noise, this is the only dataset that could be properly fitted, it is just to give an indication on the timescale of the process and not a general statement.

the duration of the pulse), giving as a result two decay constants $\tau_1 \sim 800\,\text{fs}$ and $\tau_2 \sim 50\,\text{fs}$. The fit is shown in appendix E.

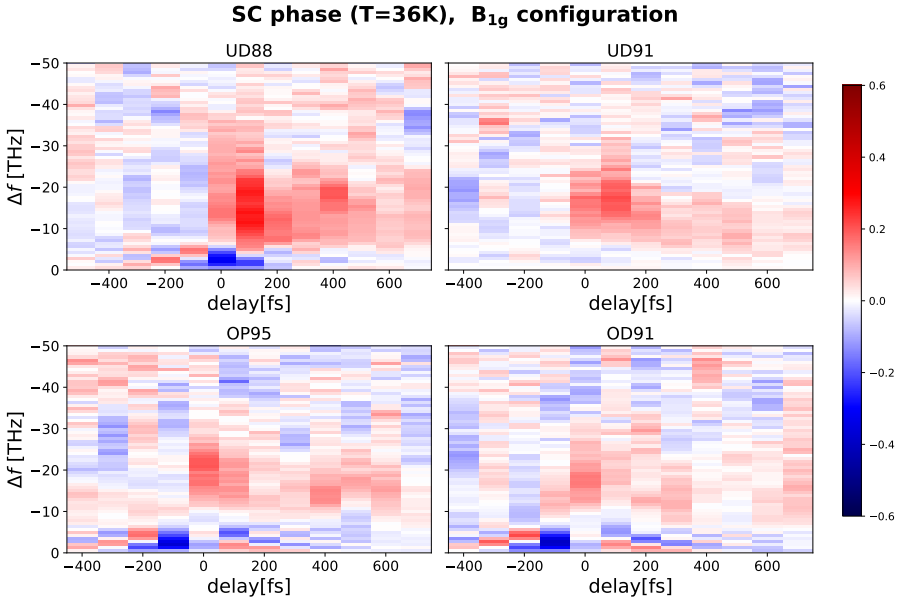

Figure 72: Dynamic correlation maps in the SC phase, in the B_{1g} configuration for the four samples.

It is difficult, due to the presence of positive and negative correlations (and obviously of noise), to define a "central frequency" for the signal, but observing the correlation marginals (see figure 76) the peak at the overlap is centered at $\sim 20\,\text{THz}$. In the following hundreds of picoseconds the peak seems to shift at slightly lower frequencies, but the overall correlation signal still lives in the same range.

There does not seem to be a substantial difference between the correlation signal for the two configurations, apart for a lower intensity in the B_{1g}, which is consistent with the birefringence measurements results. These observations will be remarked in the doping and temperature dependence analysis.

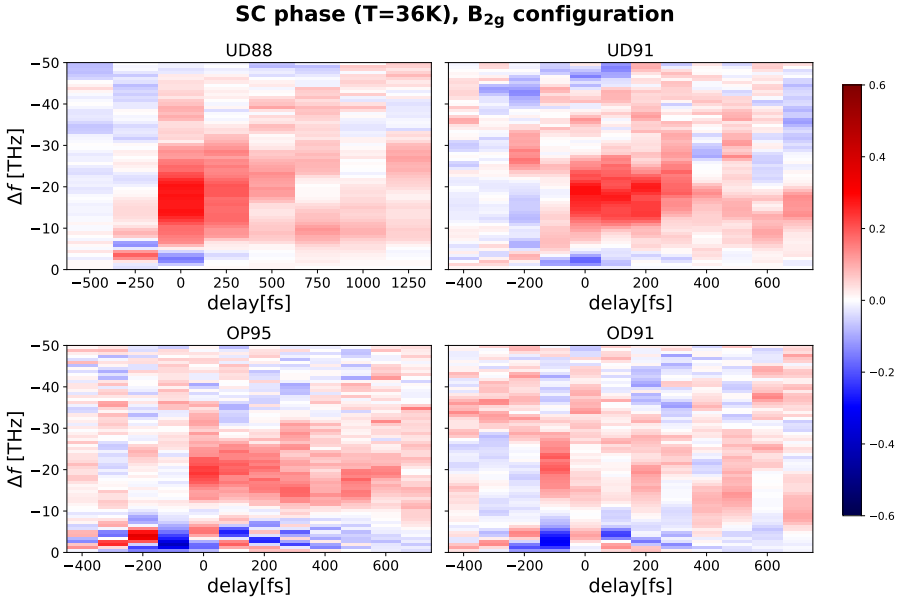

Figure 73: Dynamic correlation maps in the SC phase, in the B_{2g} configuration for the four samples.

4.3.2 Doping dependence of the signal

To further understand the correlation signal in the different samples we now show the results as a function of the doping. To recover the doping p of the sample we use the empirical formula for T_c by *Presland et al.* [48]:

$$T_c(p) = T_{c,max}[1 - 82.6(p - 16)^2]. \tag{27}$$

The formula comes from a fit of experimental data based on BSCCO samples, so the values should be a little different from ours due to the Yttrium substitution, but should give us at least a reference value for p.

In figure 75 the superconducting phase ($T \sim 36\,\mathrm{K}$) positive signal between $[-7, -25]\,\mathrm{THz}$ has been integrated in the $[-100, 500]\,\mathrm{fs}$ interval and plotted as a function of the four values of the doping for both the experimental configurations; the same signal, but only frequency integrated, is shown in 74; what is visible is a distinct decrease in the correlation signal as the value of p increases for the B_{2g} configuration, while for the B_{1g} configuration the trend is the same but less marked, apart for the UD88 sample.

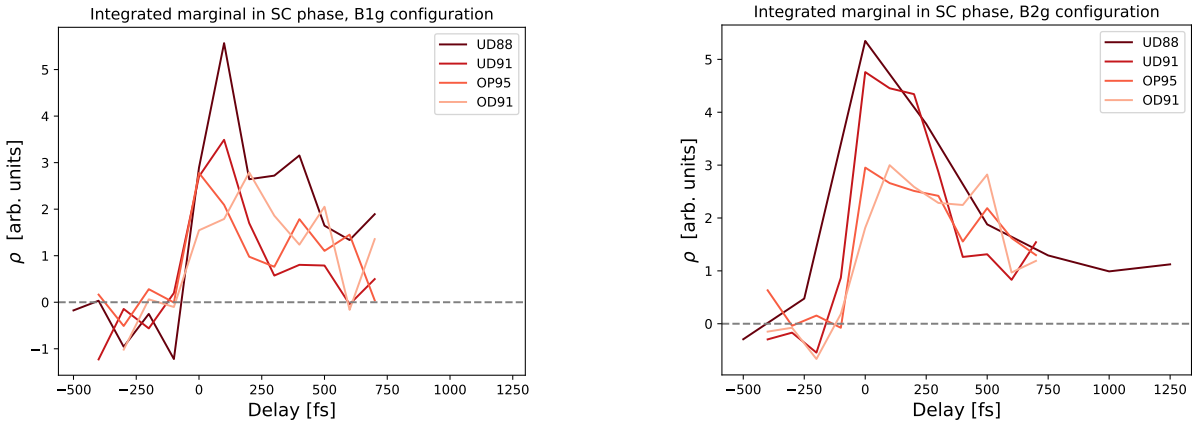

(a) (b)

Figure 74: Frequency integrated maps of the superconducting phase correlation dynamics for the different samples, in figure (a) for the B_{1g} configuration and in (b) for the B_{2g} configuration.

The other observation that can be made is about the general lower intensity of the signal in the B_{1g} configuration (in which we remember the pump polarization $\parallel CuO$) with respect to the B_{2g} ($\parallel CuCu$). By comparing figures 74a and 74b one can notice that the main cause for the difference in value of the two configurations does not come from a higher maximum intensity of the correlation signal (at the overlap the intensity is similar), but rather from what seems to be a higher intensity at positive times; to better comprehend the dynamics in different conditions we will need to do more fits, but this will be possible only with a higher signal-to-noise ratio.

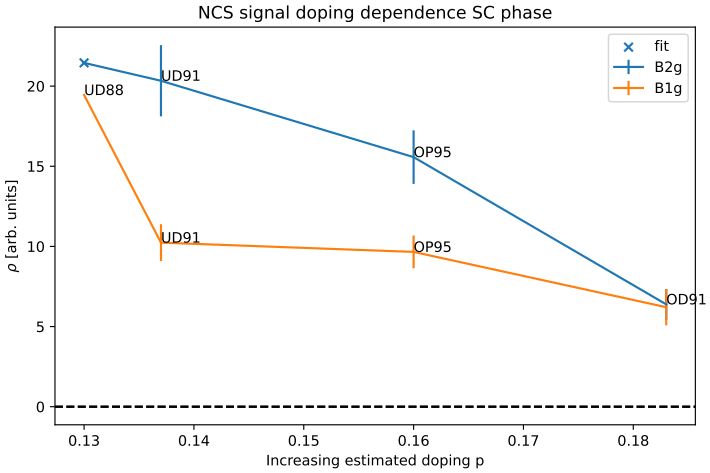

Figure 75: Time and frequency integrated correlation plots, showing the value of correlation as a function of the doping of the sample for both configurations in the superconducting phase. the UD88 sample was measured with at different delays from the other samples in the B_{2g} configuration, so the value for this point was recovered through the double exponential fit of appendix E.

The trends is the same when plotting the same quantities in the pseudogap phase ($T \sim 108\,\mathrm{K}$, figure 103 of Appendix F), but the intensity of the correlation signal for the two configurations is similar for the OP95 and OD91 sample.

While it is difficult to define a central frequency for the marginal signal and the noise makes hard stating trends, by observing the overlap signal for the different samples we see that the correlation signal at the overlap (see figure 76a) tends to be more centered at higher frequencies by increasing the doping. The already discussed intensity decrease trend is also visible. At positive times the signal does not show any visible shift (see figure 76b).

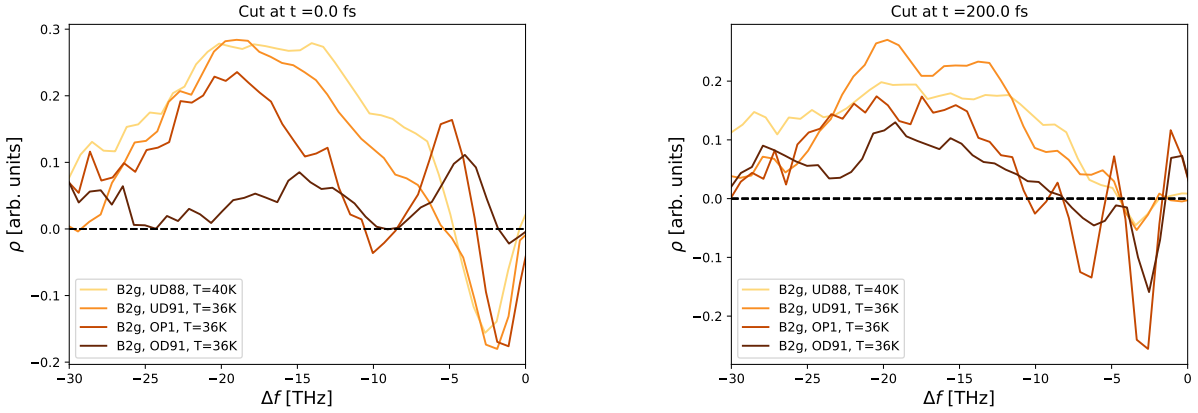

(a) (b)

Figure 76: Marginals of Pearson maps for measurements in the superconducting state on the four samples, in a) we see the overlap signal and in b) at a delay of 200 fs.

4.3.3 Temperature dependence

The FCS measurements were repeated for every sample at different temperatures, to examine the presence of correlations across the different phases and in general the temperature dependence of the signal. Due to the limitations of the technique the signal still results noisy, but a general trend can be still recovered, as will be shown in the following.

Similarly to what we did in section 4.3.2 for doping, to highlight the temperature trends for each sample we will show:

- The maps at different temperatures, which are more difficult to interpret but also show best the noise in the measurement.
- Their integration in the $[-7, -25]$ THz frequency range, so that the whole dynamics of the signal can be compared at different temperatures. Not all measurements are shown, to avoid overcrowding of the plot.
- The integration in both the $[-7, -25]$ THz frequency range and in the $[-100, 300]$ fs delay interval, plotted as a function of temperature, to best quantify the correlation signal intensity evolution in the different phases.

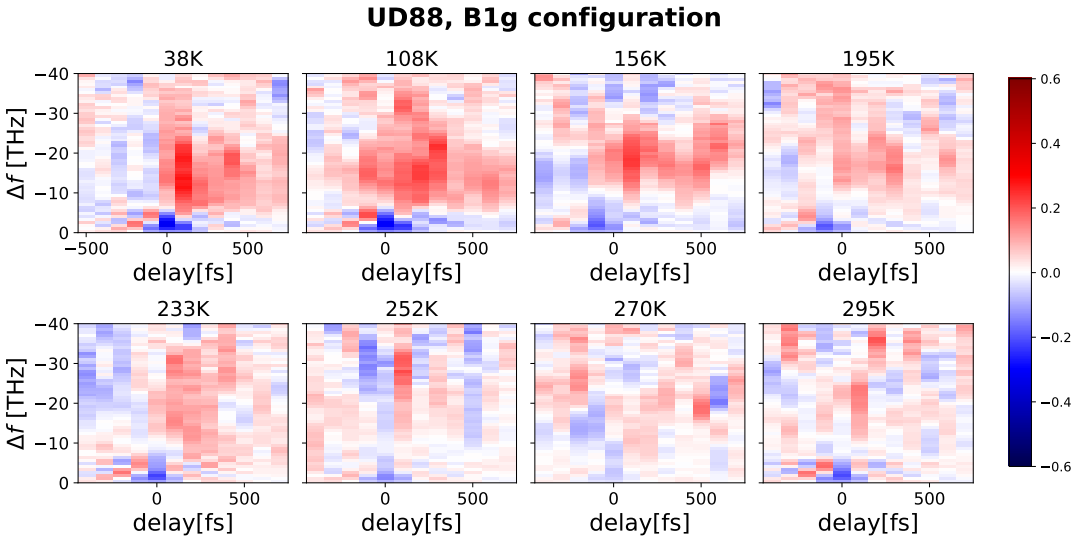

Figure 77: Set of all the measurements taken on the UD88 sample in the B_{1g} configuration at different temperatures.

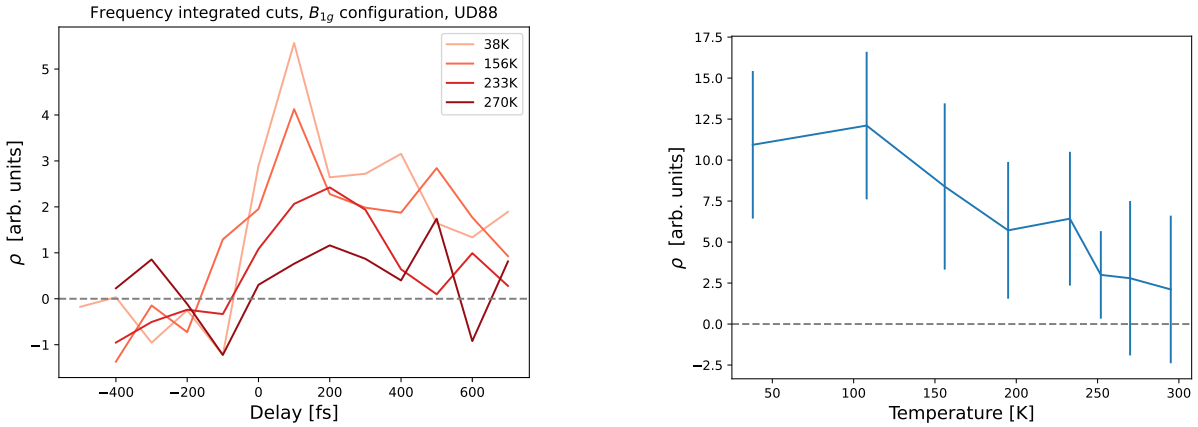

(a) (b)

Figure 78: Temperature dependence plots for the UD88 sample in the B_{1g} configuration. In figure (a) the maps in figure 77 have been integrated in frequency domain, while in figure (b) they have been further integrated in time and plotted as a function of temperature.

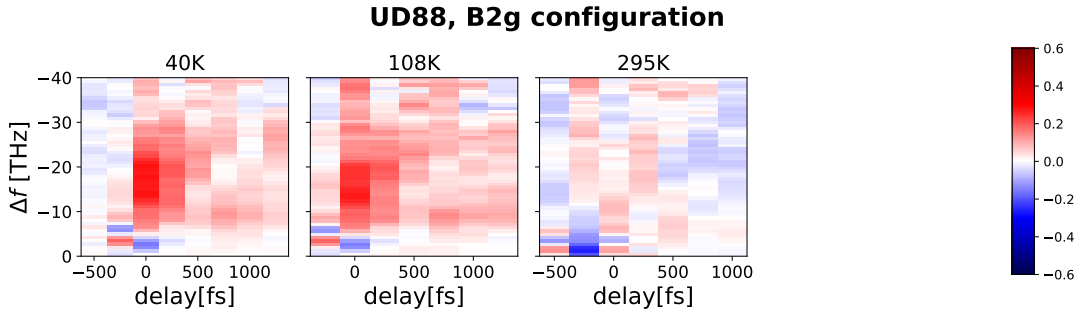

Figure 79: Set of all the measurements taken on the UD88 sample in the B_{2g} configuration at different temperatures.

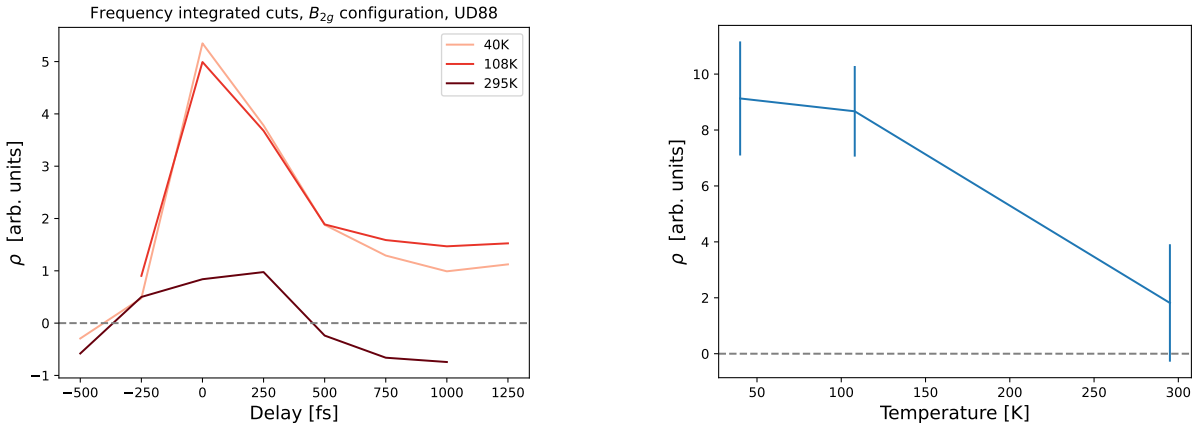

(a) (b)

Figure 80: Temperature dependence plots for the UD88 sample in the B_{2g} configuration. In figure (a) the maps in figure 79 have been integrated in frequency domain, while in figure (b) they have been further integrated in time and plotted as a function of temperature.

Starting from the lowest doping, we clearly see how in both configurations the signal decreases to near zero at $T = 295\,\mathrm{K}$, even though for the B_{2g} measurements we only have few points. Looking at the maps in 77 the signal is in the same intensity range of the noise at $T = 270\,\mathrm{K}$, which is approximately where we expect T^* to be for this sample.

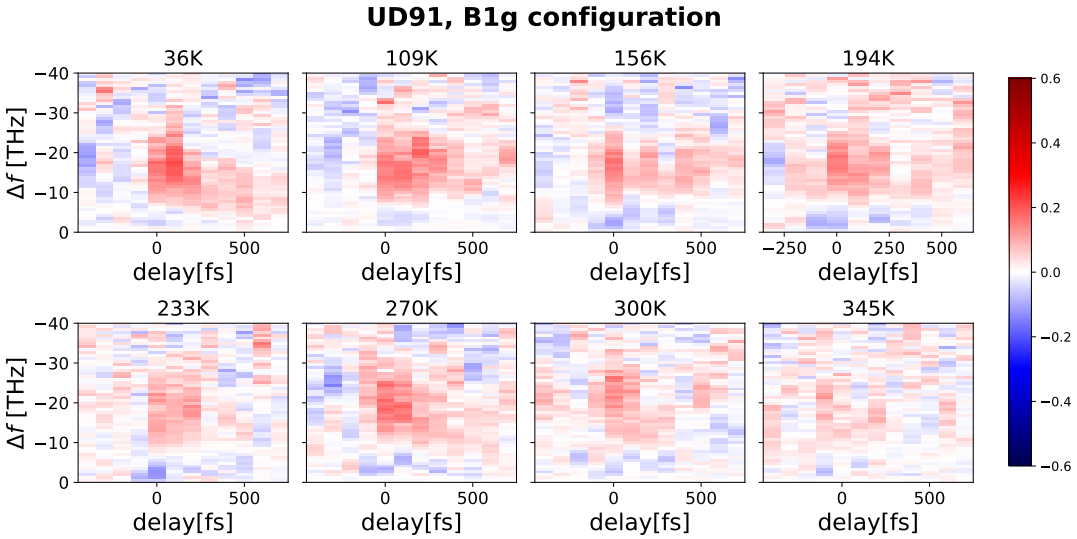

Figure 81: Set of all the measurements taken on the UD91 sample in the B_{1g} configuration at different temperatures.

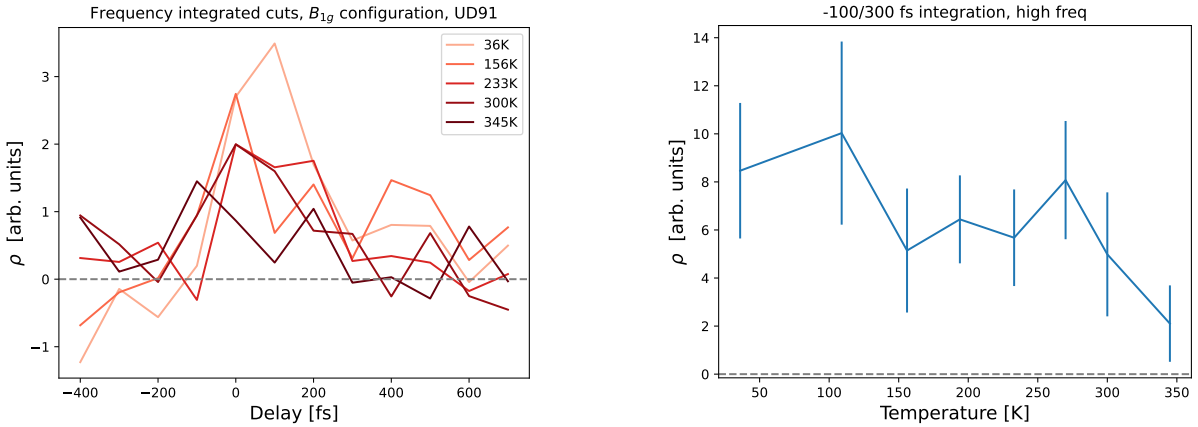

(a) (b)

Figure 82: Temperature dependence plots for the UD88 sample in the B_{1g} configuration. In figure (a) the maps in figure 81 have been integrated in frequency domain, while in figure (b) they have been further integrated in time and plotted as a function of temperature.

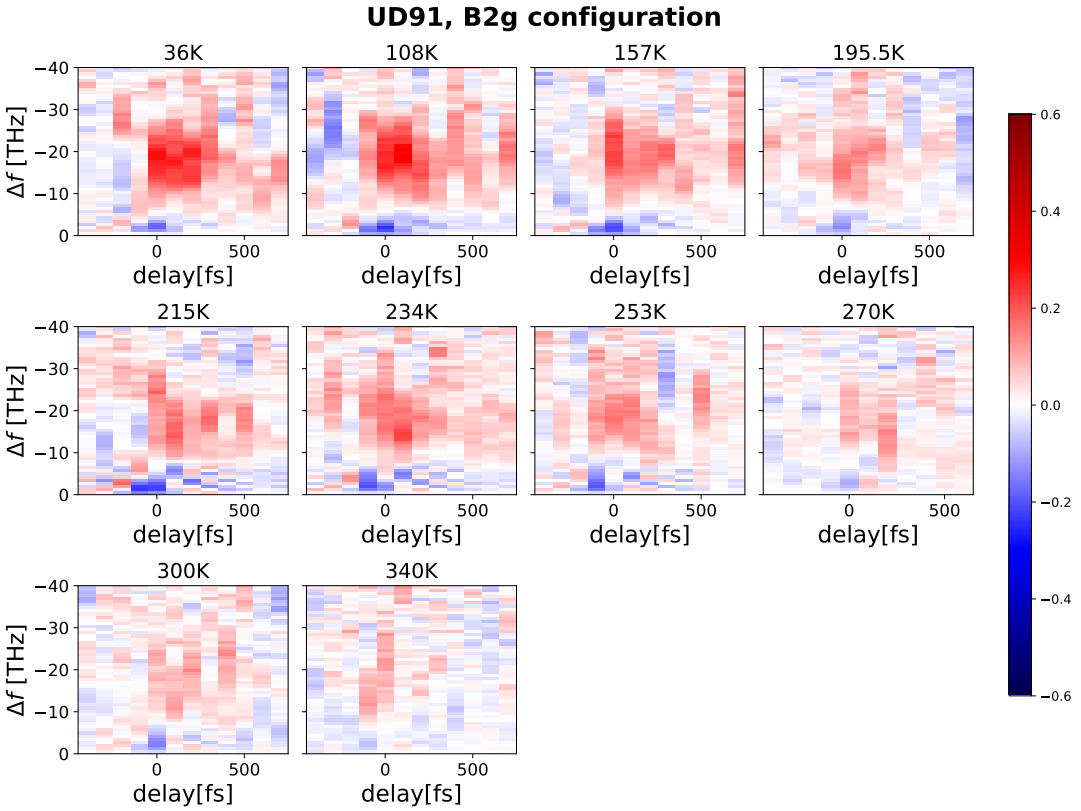

Figure 83: Set of all the measurements taken on the UD91 sample in the B_{2g} configuration at different temperatures.

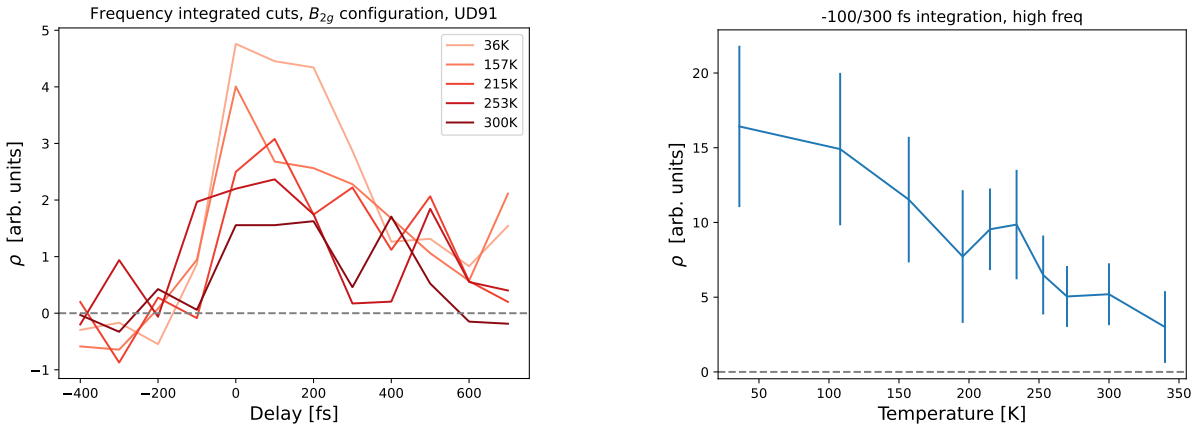

(a) (b)

Figure 84: Temperature dependence plots for the UD91 sample in the B_{2g} configuration. In figure (a) the maps in figure 83 have been integrated in frequency domain, while in figure (b) they have been further integrated in time and plotted as a function of temperature.

Observing the temperature dependence in 82, 84 and the respective maps it seems that for this higher doping, which should show a smaller pseudogap region ($T^* \sim 220\,\mathrm{K}$), a correlation signal survives up to room temperature for both the configurations. Due to this observation we heated the sample to 340 K to obtain a map with zero correlation signal.

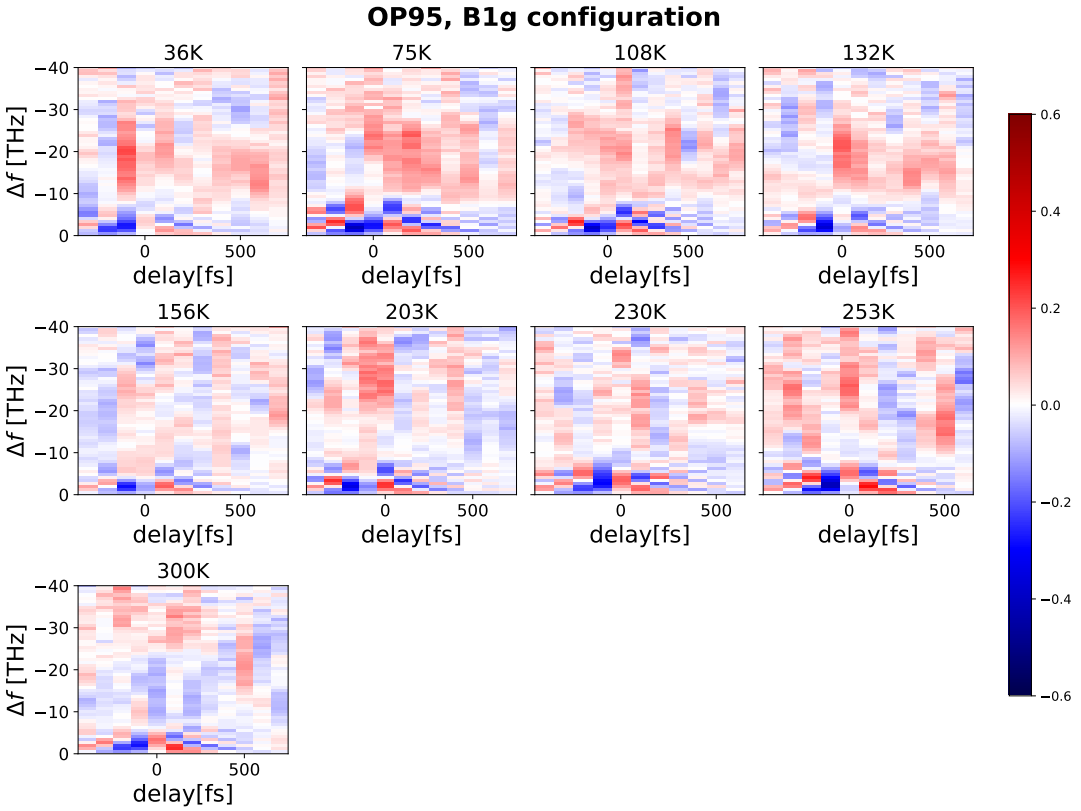

Figure 85: Set of all the measurements taken on the OP95 sample in the B_{1g} configuration at different temperatures.

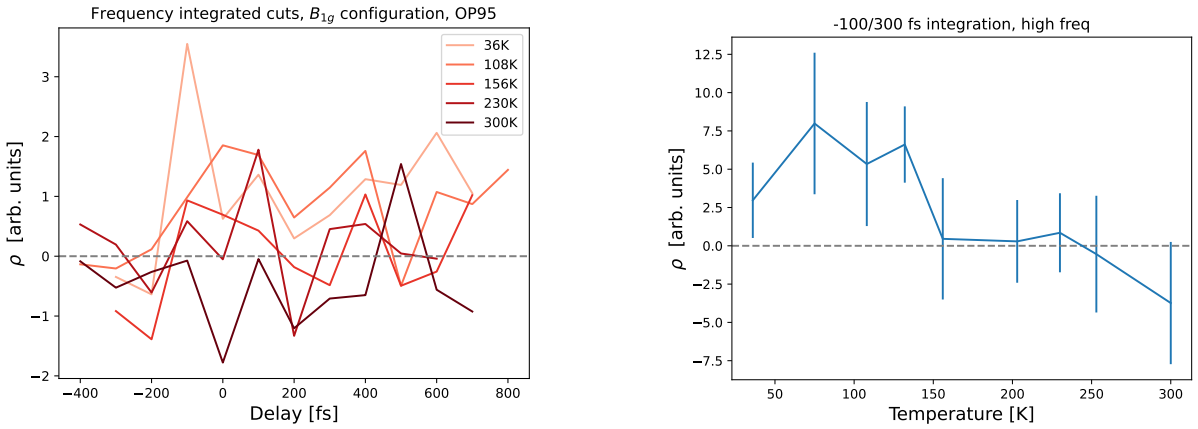

(a) (b)

Figure 86: Temperature dependence plots for the OP95 sample in the B_{1g} configuration. In figure (a) the maps in figure 85 have been integrated in frequency domain, while in figure (b) they have been further integrated in time and plotted as a function of temperature.

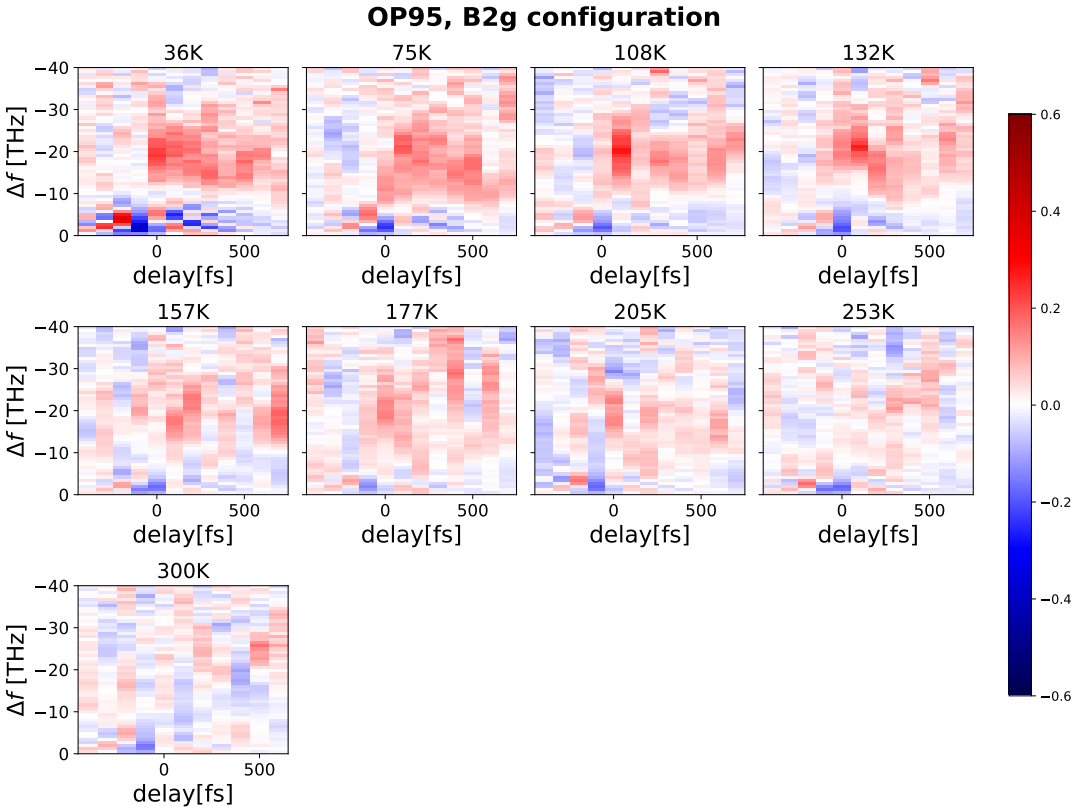

Figure 87: Set of all the measurements taken on the OP95 sample in the B_{2g} configuration at different temperatures.

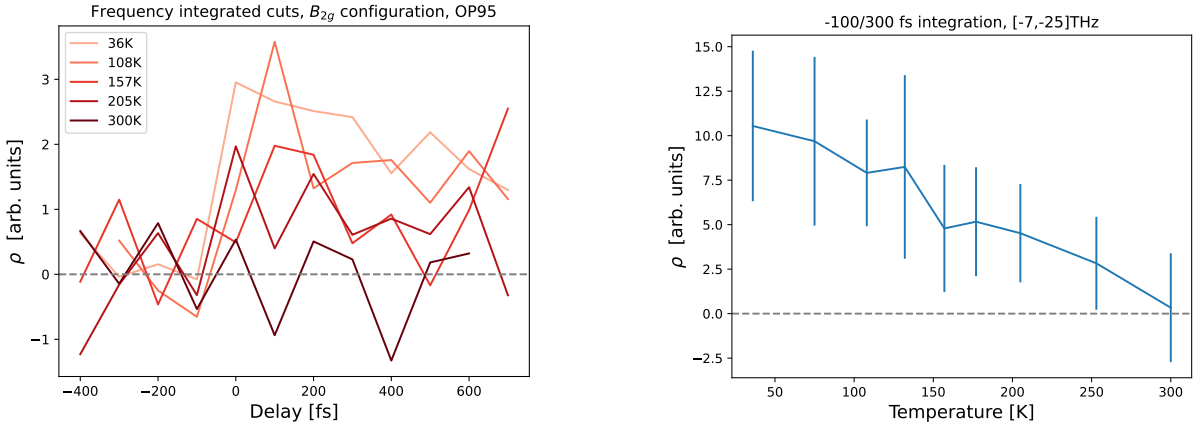

(a) (b)

Figure 88: Temperature dependence plots for the OP95 sample in the B_{2g} configuration. In figure (a) the maps in figure 87 have been integrated in frequency domain, while in figure (b) they have been further integrated in time and plotted as a function of temperature.

For the optimally doped sample the situation seems different for the two configurations: for the B_{1g} configuration the correlation seems to go to zero at arounf $T^* \sim 150\,\mathrm{K}$, beyond what we estimate to be the end of the pseudogap ($\sim 125\,\mathrm{K}$), while for the B_{2g} it seems to survive a little more, as figure 88b suggests a decreasing trend that goes to zero only at $300\,\mathrm{K}$ but the noise is quite more persistent in the $205 - 253\,\mathrm{K}$ measurements (figure 87).

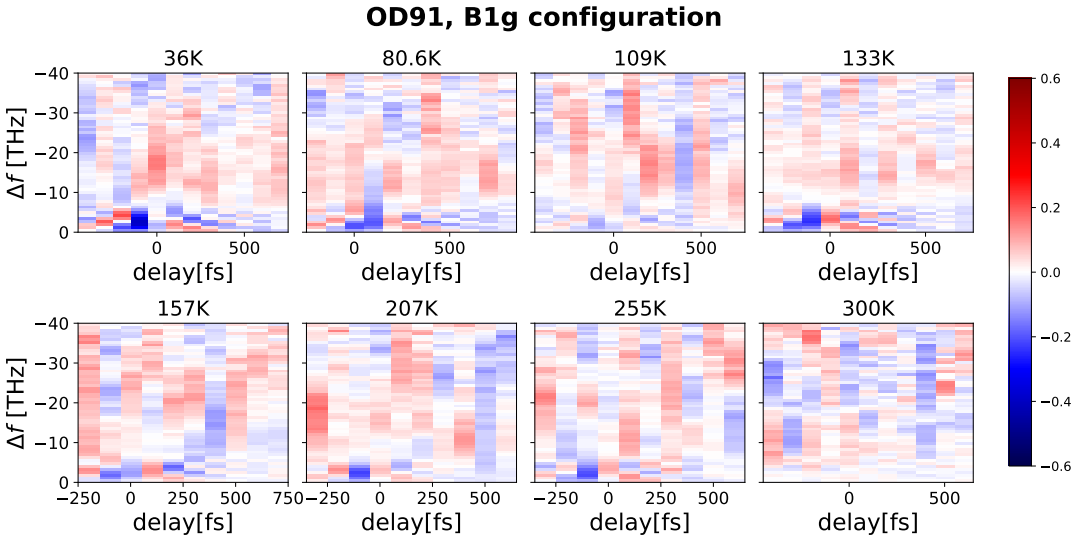

Figure 89: Set of all the measurements taken on the OD91 sample in the B_{1g} configuration at different temperatures.

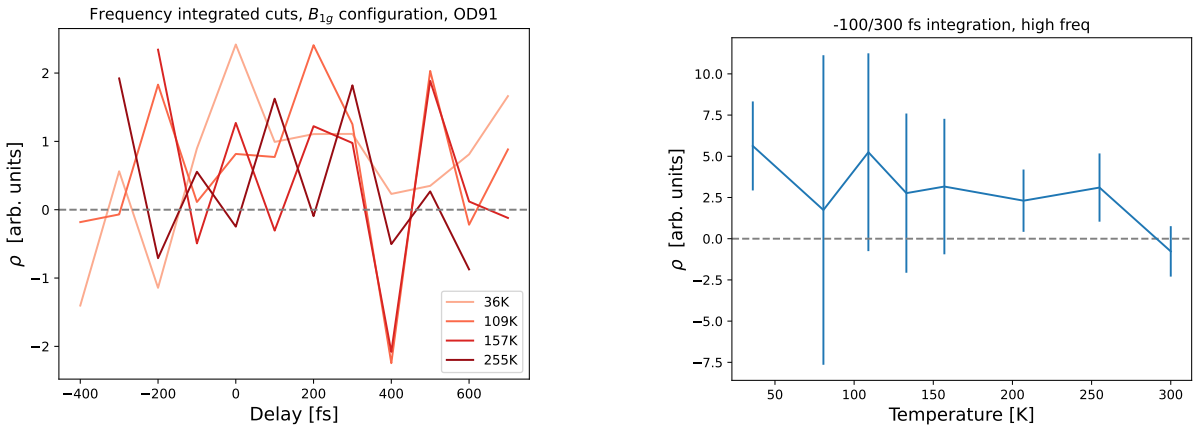

(a) (b)

Figure 90: Temperature dependence plots for the OD91 sample in the B_{1g} configuration. In figure (a) the maps in figure 89 have been integrated in frequency domain, while in figure (b) they have been further integrated in time and plotted as a function of temperature.

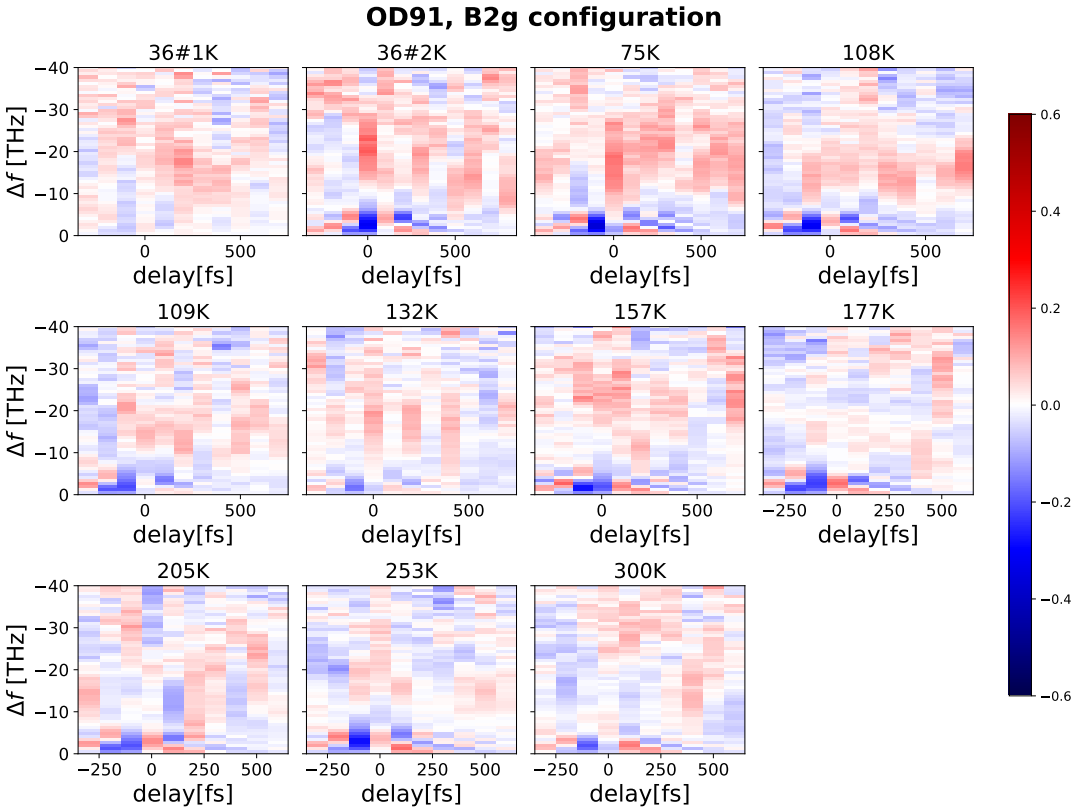

Figure 91: Set of all the measurements taken on the OD91 sample in the B_{2g} configuration at different temperatures.

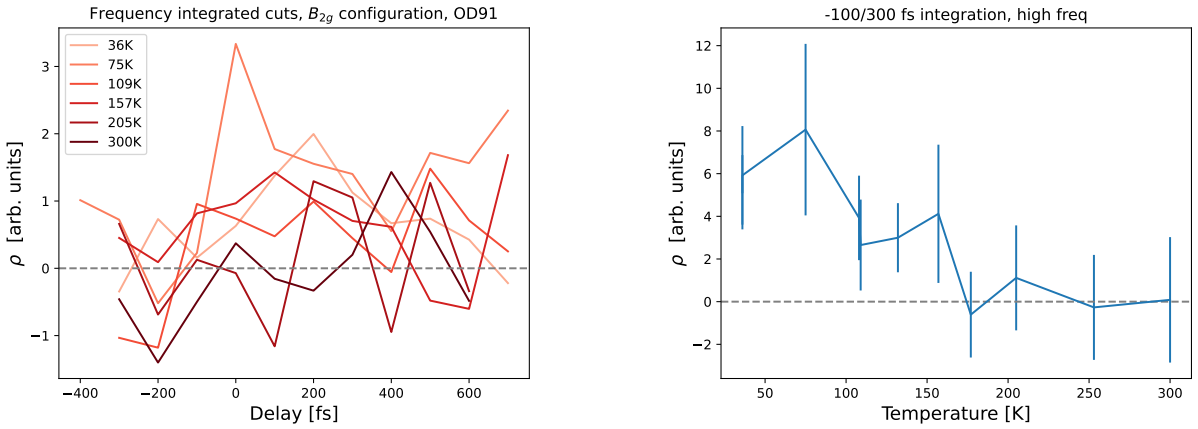

(a) (b)

Figure 92: Temperature dependence plots for the OD91 sample in the B_{2g} configuration. In figure (a) the maps in figure 91 have been integrated in frequency domain, while in figure (b) they have been further integrated in time and plotted as a function of temperature.

Lastly, for the overdoped sample the signal definitely goes to zero at a lower temperature with respect to all the other samples. We expect the end of the pseudogap to be around $T^* \sim 105 - 110\,\mathrm{K}$, which is a little below the reasonable end of the correlation signal for both configurations, but also in this case for the B_{2g} the existence of correlation above that temperature cannot be excluded (see figure 91).

4.3.4 Discussion

- **Polarization configuration**: The two different configurations are not able to properly isolate the two different electronic modes, however if one follows the calculation for the selection rules in this condition we know that for Pump$\|$ CuO we have a contribution $\propto A_{1g} + B_{1g}$, while for Pump$\|$ $CuCu$ we have proportionality to $A_{1g} + B_{2g}$. From the birefringence measurements we have observed a generally richer signal for the B_{2g} electronic mode, while for the B_{1g} mode it was rather flat and less intense. Putting this observations together might explain why we observe in most measurements a higher correlation intensity for the Pump$\|$ $CuCu$ configuration.

- **Doping dependence**: The doping dependence of the signal points to the fact that correlations grow stronger as the doping is lowered, it would be interesting to further investigate this matter with other samples with lower doping, even with a pristine BSCCO sample, to examine the possible origins of such correlations.

- **Temperature dependence**: For what concerns the temperature evolution, the method recovers a correlation signal across the superconducting and pseudogap phases, with a slight change in the dynamics but qualitatively involving a similar range of frequencies. For the UD88, OP95 and OD91 samples the signal seems to be present until the transition to the normal phase, maybe surviving a little more then expected, but it is hard to state due to the low signal-to-noise ratio. For the UD91 sample the signal seems to be present even at room temperature, which is out of the expected trend, since it should have a lower T^* than the UD88 sample. This could suggest the existence of some other order in this doping region; the underdoped region is in fact the one that presents strongest quantum correlations and thus the richest phase diagram (see figure 2), even though the onset of charge order should be lower than T^*.

In the past, spontaneous Raman scattering experiments have shown the response of the electronic modes in the superconducting state, but any signal present was demonstrated to go to zero above T_c [32].However, our measurements showed the presence of signal also throughout the pseudogap region. In this perspective, we underline that FCS is a technique that radically differs from standard Raman spectroscopy measurements because 1) it is impulsive and requires no time integration 2) and because its stimulated nature generates phase-locked excitations: as a consequence, the recorded signal is *coherent*, differently from the spontaneous Raman scattering incoherent signal. The existence of a correlation signal in the pseudogap phase and its disappearance in the normal phase could be thus an indication of the existence of local pairing above T_c, reinforcing the idea that phase coherence and electron pairing are two different requirements needed to attain the superconducting state [23]. These local pairs would be invisible to standard spontaneous Raman scattering, as their random phase signal would average to zero in the integration, but not to FCS, due to the already explained properties of the technique [19].

Another consideration is the probe wavelength dependence: since the birefringence signal is not present at 700 nm for all samples, and since now we know that the detection cannot isolate the two modes through cross-correlation, what is the rationale behind the existence of a correlation signal at 700 nm and not at 900 nm ? A resonant condition at this wavelength could explain the difference and might be linked to the different results obtained by changing the noise configuration (Appendix D).

To conclude this final section of the thesis, before the actual conclusion section, we have put together the estimated transition temperatures recovered with the different measurements to create a phase diagram, which is represented in figure 93. The estimated T_c are calculated as an average between the estimate done from the B_{1g} and B_{2g} temperature dependence study,

which results rather similar to the nominal T_c of the samples; The two T^* represent, as visible in the legend, the end of the pseudogap phase as estimated in the single channel section (see the table at the end of 2.3.1) and an approximate end of the correlation signal in the FCS experiments. The dashed purple line separating the pseudogap phase and the normal phase has been obtained by doing a linear regression on the single channel T^* values.

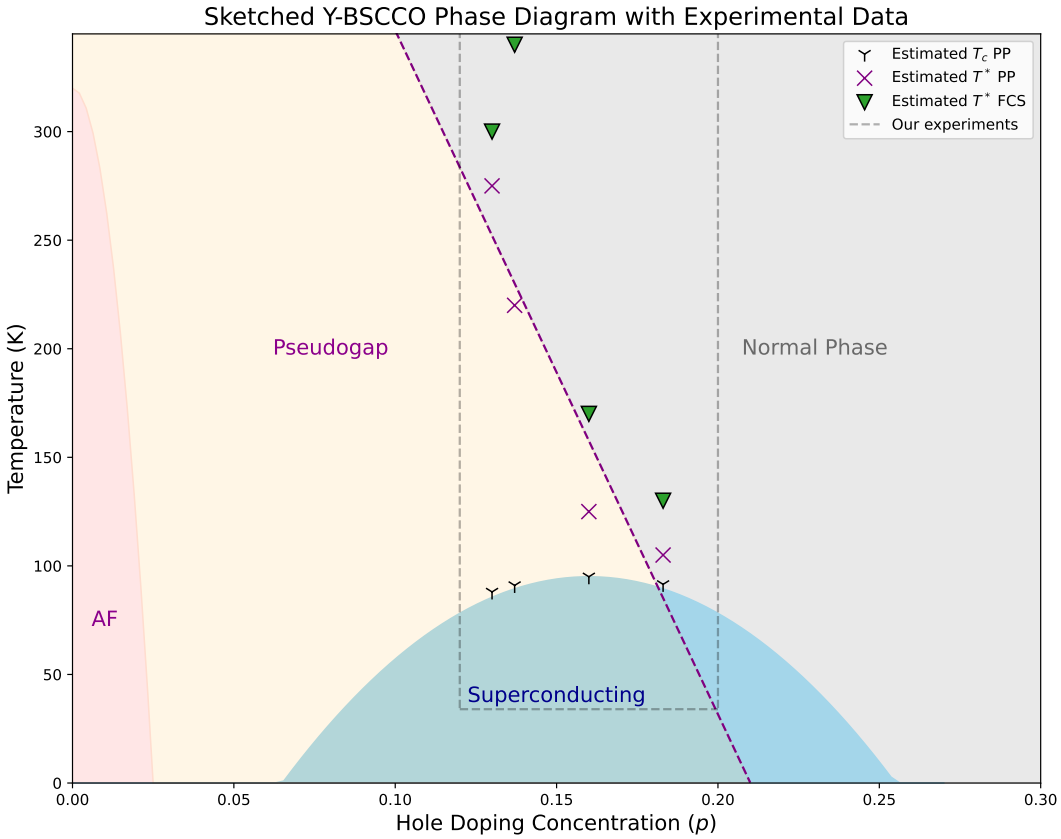

Figure 93: Sketched phase diagram of cuprates overlapped with the experimental data obtained through optical observables from the different types of measurements used in this thesis. The grey dashed lines contains the region of the diagram explored by our measurements.

5 Conclusions

In this thesis we explored the dynamics of high-temperature superconductor $Y-Bi_2Sr_2Ca_{0.92}Cu_2O_{\delta+8}$ samples at different doping, using nonlinear spectroscopy techniques to explore its reflectivity spectrum in the superconducting, pseudogap and normal phase. In particular we used a "conventional" pump-probe technique and a novel spectroscopy technique relying on the measurement of multimode correlations imprinted by the material on the pulse.

In the first part we studied evolution of the transient differential reflectivity signal across the $1.3-2.0\,\mathrm{eV}$ energy range caused by a MIR excitation with a wavelength of $17\,\mu\mathrm{m}$. Most importantly, by measuring the birefringence signal, we managed to isolate two different electronic modes of the sample. The B_{1g} mode, which is associated with the antinodal excitations, did not exhibit strong signal, but showed changes across the T_c transition. The B_{2g} mode, which is associated with nodal excitations, showed a much intense signal, a richer spectrum and a strong dependence from the doping in the superconducting state.

In the second part we explored a perturbation effect in the superconducting signal caused by the presence of chirp in the probe pulse: the spectral weight of the signal shifts towards the first interacting frequencies. We then proceeded to test the dependence of such effect from the phase, the doping, and the fluence of the probe. We discovered that the effect is present also at low fluences, when the probe is in the linear regime, and is stronger in sample with lower doping. The effect is an interesting finding that might be explored more in the future and prompts caution about the use of chirped probes in complex systems, but also introduces a new degree of freedom in the manipulation of the system.

In the last part of the thesis we used Femtosecond Covariance Spectroscopy-a spectroscopic technique developed by our group-to explore the electronic correlation dynamics of the samples across different phases, with sub-ps resolution. Notably, we measured a multimode correlation signal in the superconducting state of all the Y-BSCCO samples that we tested. The intensity of the correlation signal depends on which electronic mode is involved, and coherently with the birefringence measurements, the B_{2g} mode is the more intense. Importantly, the correlation signal survives to the superconducting-to-pseudogap transition and decreases to zero as the temperature increases; a correlation signal also appears to survive at temperatures associated with the normal phase. The technique still cannot achieve a good signal-to-noise ratio due to the long acquisition time necessary for a single measurement. Making precise statements is thus difficult in this condition, but the existence of the signal and its temperature dependence are clear. The possibility that the correlation signal is an indication of local pairing in pseudogap and the existence of a signal above the expected T^* prompt to the exploration of other samples at different doping, to better understand the nature of these correlations and local orders that might cause them.

A Birefringence signal of transition at T^*

As stated before the transition between pseudogap and normal phase is in general harder to detect compared to the end of the superconducting phase. Through single channel measurements we can map the transition because of the negative trace at higher energies, but this feature appears to be linked mainly to the A_{1g} mode, because it does not show in either of the birefringence configurations. In most samples the transition barely shows in the birefringence signal (see figure 94a), but in figure 94b it seems that by integrating the upper energy region we can manage to get observe a weak change in the OP95 sample measurement. Notice that even if integrating in a wider energy range, the variation that the signal exhibits over the whole measurement is more than an order of magnitude smaller then what can be seen in the single channel signal 25.

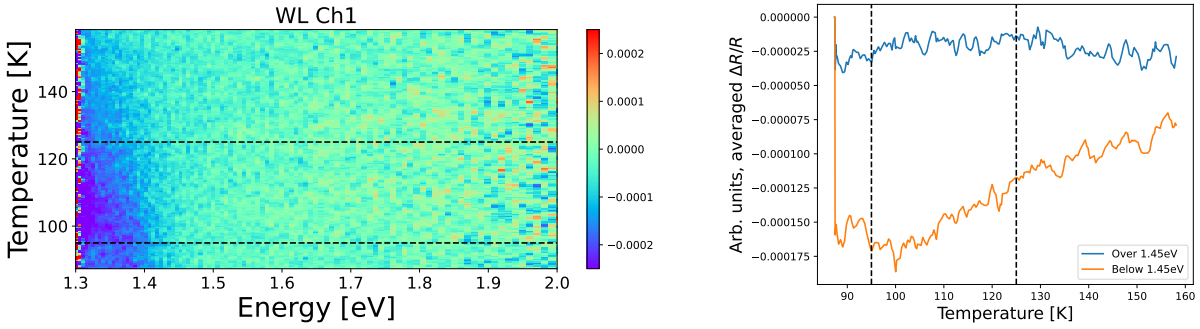

(a) (b)

Figure 94: Birefringence signal temperature scan across T^* for the OP95 sample in the B_{1g} configuration. In figure (a) the measurement has been averaged along a picosecond duration to show the intensity of the birefringence as a function of frequency an temperature, while in figure (b) it has been also averaged to compare the weight of different spectral regions (the regions are in the labels). The dashed lines indicate T_c and the estimated T^*.

B Probe linearity measurement of the $700nm$ probe

To verify that the perturbation was introduced by the chirp itself we used the pulse shaper to vary the fluence of the compressed probe pulse, obtaining the measurements in figure 95. At the top of the titles is reported the average pulse power in mW, which can be converted in fluence by knowing the beam diameter and repetition rate:

Power [μW]	39	76	181	350	636
Fluence [mJ/cm^2]	27.6	53.8	128.0	247.6	449.9

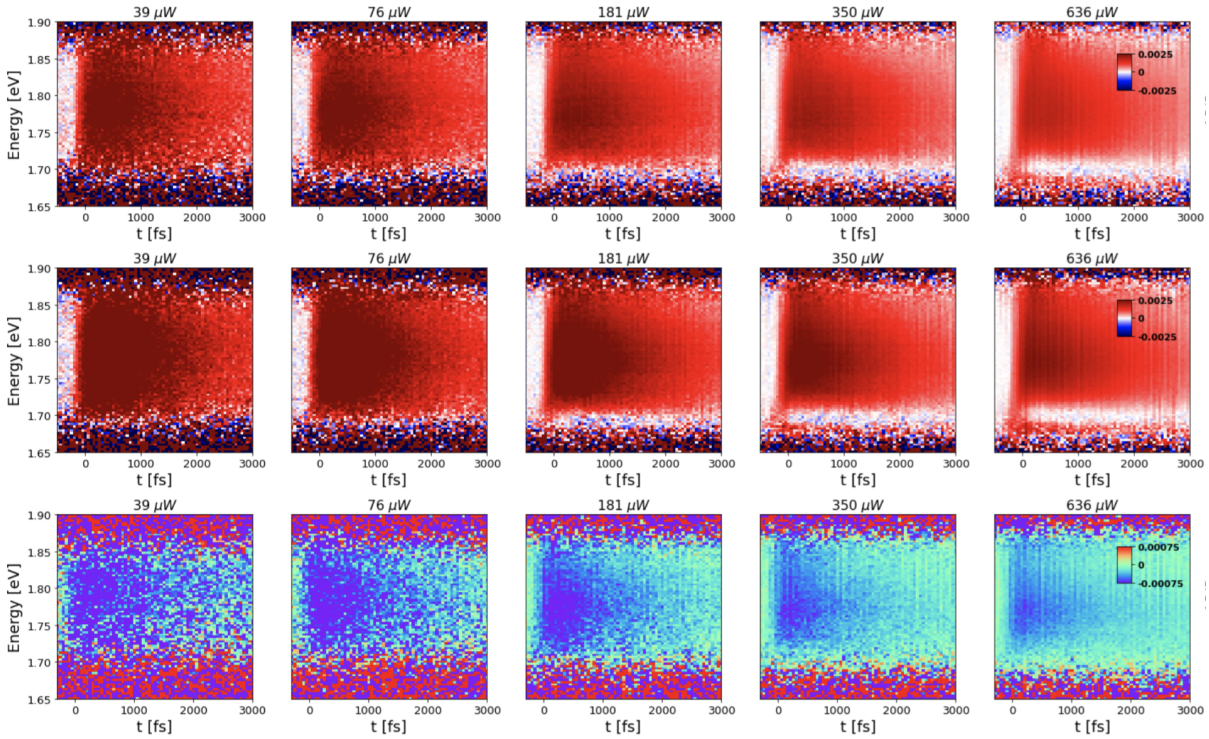

Figure 95: Differential reflectivity measurements at increasing probe fluences (in the titles) for the UD88 sample in the superconducting state. In the first row the signal in Ch0, in the second of Ch1 and in the third row the resulting birefringence, isolating the B_{2g} mode.

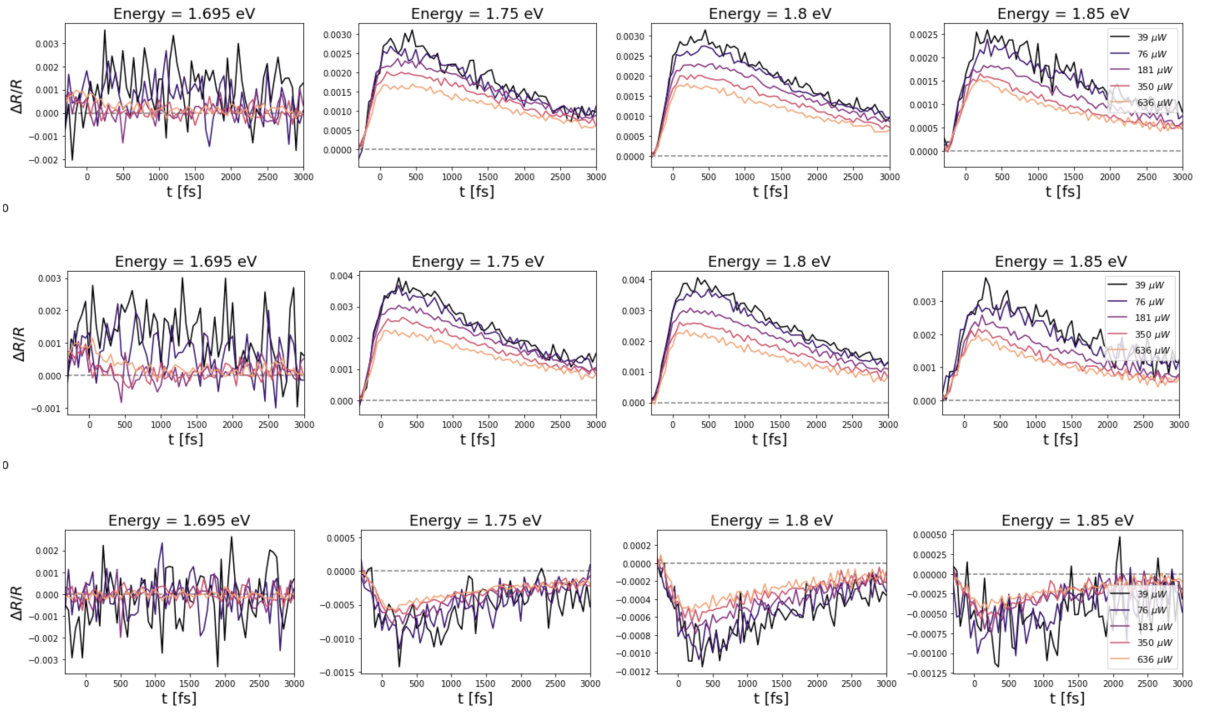

Figure 96: Cuts at fixed energies (in the titles) of the probe linearity test of figure 95, the rows of the two figures are corresponding.

By observing the resulting measurements and their cuts at fixed energy respectively in figures 95 and 96 the signal appears to decrease its intensity by increasing the fluence (at every step

the fluence roughly doubles), with only the two lowest fluences resulting in superimposed. The shape of the signal at single energy is similar across the different measurements, apart from the negative trace at low energy.

C Autocorrelation vs. cross-correlation

The original idea was to isolate the electronic modes correlations through the study of the cross-correlators of the main and residual polarizations. It appears that this method does not give the expected results, as the signal is in most cases indistinguishable from the auto-correlator one, there must be a "spillage" between the two polarizations, due to the imperfect filtering by the polarizing beam splitter.

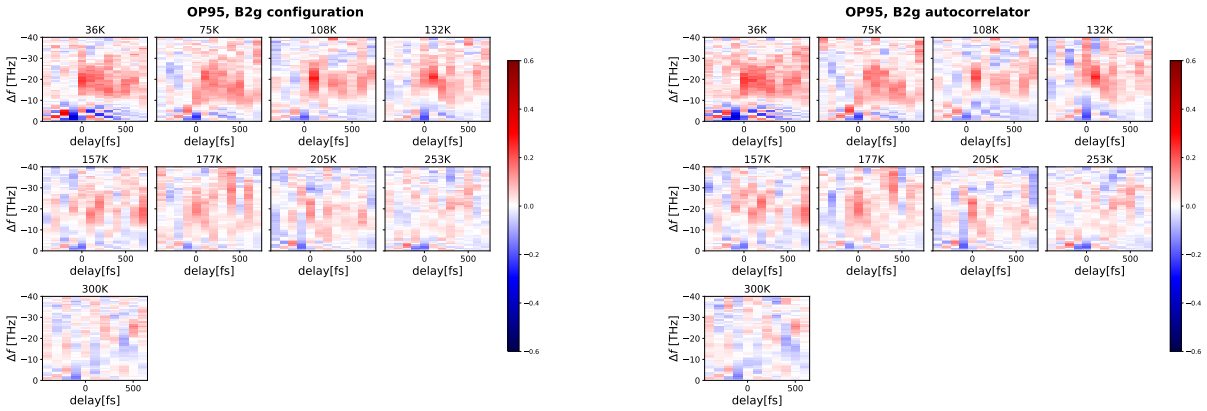

(a) (b)

Figure 97: Correlation dynamics maps at different temperatures for the optimally doped sample in the B_{2g} configuration calculated with cross-correlation (left) and autocorrelation (right).

D Noise configuration test

The selection of the partial noise modulation adds the choice of which side of the spectrum will be subjected to the stochastic fluctuations. This should not change qualitatively the correlation signal, but as shown in figure 98 the application of noise to the high or low energy side of the pulse spectrum results in very different correlation signals at the overlap.

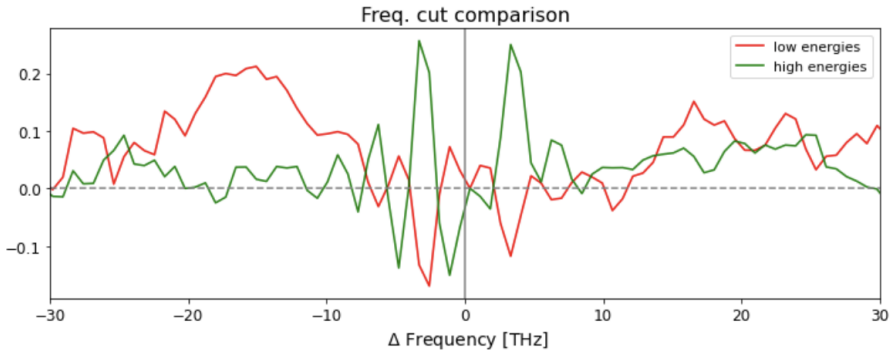

Figure 98: Correlation marginals at the overlap for two different noise configurations in the superconducting state.

The low energy features are present also in this case, amplified and sign flipped, but the positive correlation trace is zero. To better understand the reasons of this change we will test

different probe wavelengths to see if this is due to some sort of resonant condition. Another possibility is that the effect is related to the arrival of some frequencies before others, like the phenomenon of Section 3, in this case it will be necessary to manipulate the temporal profile of the pulse.

E Superconducting correlation fit

As stated in section 4 the frequency integrated correlation signal (integrating in the positive correlation region, $[10, 35]$ THz range) could be fitted to the convolution of two exponential functions and a Gaussian. Due to the low signal-to-noise ratio the only datasets on which we could do the fit were measurements of the UD88 sample in the superconducting phase (B_{2g} configuration); we could increase the number of repetitions, as that would increase too much the duration of the experiment, making it susceptible to setup instabilities (e.g. changes in humidity can cause misalignments and laser power decrease).

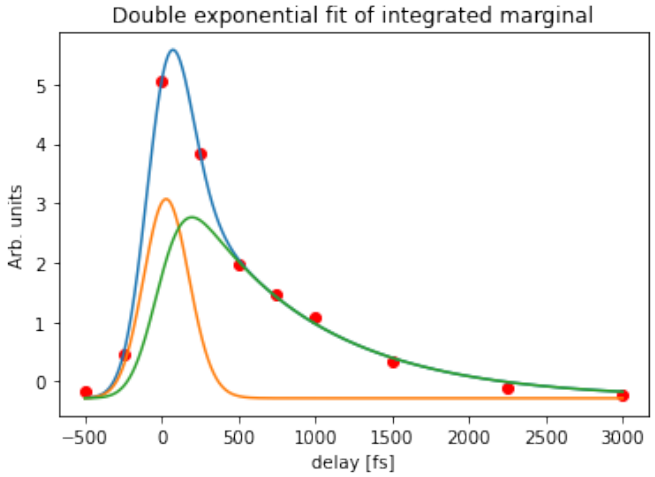

Figure 99: Fit of the exponential decay of the correlation signal in the UD88 sample in SC phase

F Pseudogap phase correlation signal

As discovered in previous measurements by our group, a correlation signal analogous to the superconducting one exists also in the pseudogap phase. Therefore, if the correlation signal is due to the scattering of the superconducting gap, this might point to the existence of local pairing above T_c.

The experimental conditions for the measurements in the pseudogap phase are analogous to the ones in superconducting phase, with the temperature set at $T \sim 108\,\mathrm{K}$. As already observed in [19], [39], a correlation signal analogous to the superconducting one exists also in this phase. The dynamics in this case are not visibly different from the superconducting ones, the only clear trends are the decrease of correlation signal intensity. Another thing that can be observed is that the signal shows correlation even at $-100\,\mathrm{fs}$, which might be due to the interaction of the material with the noisy tail of the probe.

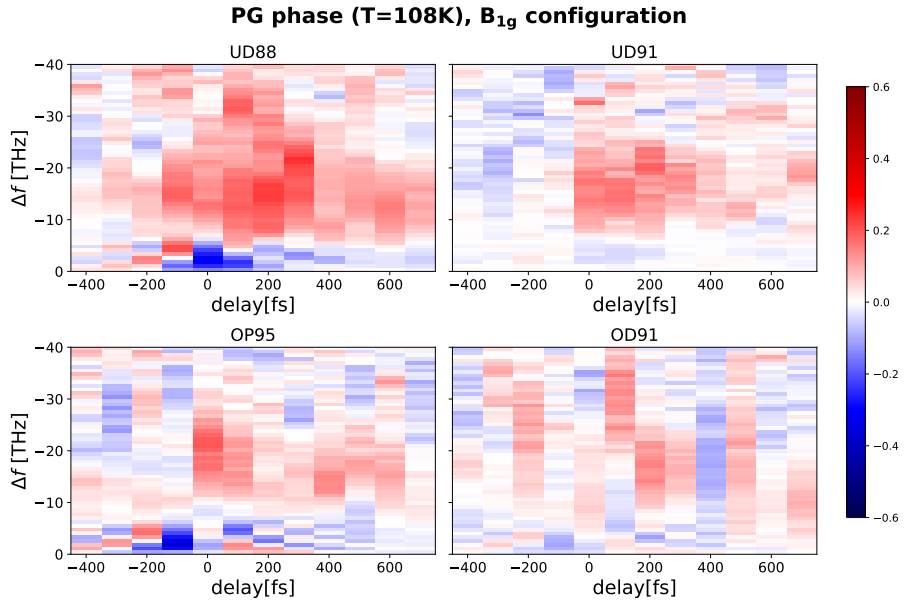

Figure 100: Dynamic correlation maps in the SC phase, in the B_{1g} configuration for the four samples.

Also in this type of measurements there seems to be an intensity difference (with weaker B_{1g}) between the two configurations, by comparing 100 and 101. In figure 103 this trend does not appear so clearly in the OP95 and OD91 samples, but from the cuts (figure 102) we can see that many of these measurements appear rather noisy, so it is hard to make statements.

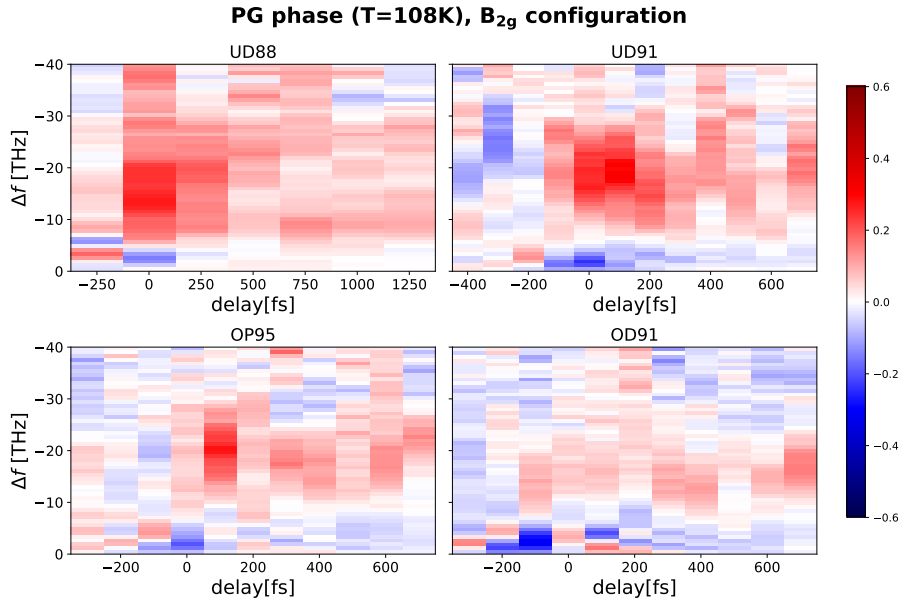

Figure 101: Dynamic correlation maps in the SC phase, in the B_{2g} configuration for the four samples.

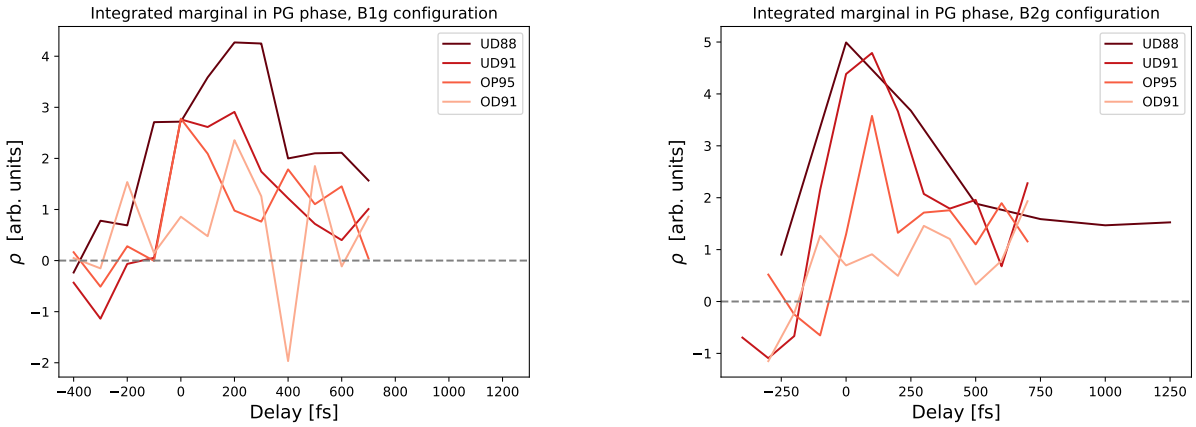

(a) (b)

Figure 102: Frequency integrated maps of the pseudogap phase correlation dynamics for the different samples, in figure (a) for the B_{1g} configuration and in (b) for the B_{2g} configuration.

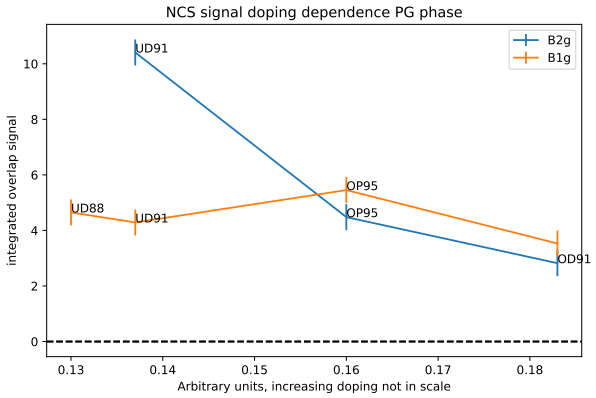

Figure 103: Time and frequency integrated correlation plots, showing the value of correlation as a function of the doping of the sample for both configurations in the pseudogap phase. The UD88 sample was measured with at different delays from the other samples in the B_{2g} configuration, and unlike figure 75 this point could not be recovered through a fit.

References

[1] Margherita Maiuri, Marco Garavelli, and Giulio Cerullo. Ultrafast spectroscopy: State of the art and open challenges. *Journal of the American Chemical Society*, 142(1):3–15, December 2019.

[2] Subir Sachdev. *Quantum Phases of Matter*. Cambridge University Press, March 2023.

[3] J. Bardeen, L. N. Cooper, and J. R. Schrieffer. Theory of superconductivity. *Phys. Rev.*, 108:1175–1204, Dec 1957.

[4] J. G. Bednorz and K. A. Müller. Possible hight c superconductivity in the ba?la?cu?o system. *Zeitschrift für Physik B Condensed Matter*, 64(2):189–193, June 1986.

[5] Philip W. Anderson. Is there glue in cuprate superconductors? *Science*, 316(5832):1705–1707, 2007.

[6] B. Keimer, S. A. Kivelson, M. R. Norman, S. Uchida, and J. Zaanen. From quantum matter to high-temperature superconductivity in copper oxides. *Nature*, 518(7538):179–186, February 2015.

[7] Eduardo Fradkin, Steven A. Kivelson, and John M. Tranquada. Colloquium: Theory of intertwined orders in high temperature superconductors. *Rev. Mod. Phys.*, 87:457–482, May 2015.

[8] Liyang Chen, Dale T. Lowder, Emine Bakali, Aaron Maxwell Andrews, Werner Schrenk, Monika Waas, Robert Svagera, Gaku Eguchi, Lukas Prochaska, Yiming Wang, Chandan Setty, Shouvik Sur, Qimiao Si, Silke Paschen, and Douglas Natelson. Shot noise in a strange metal. *Science*, 382(6673):907–911, November 2023.

[9] Shusen Ye, Changwei Zou, Hongtao Yan, Yu Ji, Miao Xu, Zehao Dong, Yiwen Chen, Xingjiang Zhou, and Yayu Wang. The emergence of global phase coherence from local pairing in underdoped cuprates. *Nature Physics*, 19(9):1301–1307, June 2023.

[10] J. Zaanen, G. A. Sawatzky, and J. W. Allen. Band gaps and electronic structure of transition-metal compounds. *Phys. Rev. Lett.*, 55:418–421, Jul 1985.

[11] M. A. van Veenendaal, G. A. Sawatzky, and W. A. Groen. Electronic structure of $\mathrm{bi_2sr_2ca_{1-x}y_xcu_2o_{8+\delta}}$: Cu 2p x-ray-photoelectron spectra and occupied and unoccupied low-energy states. *Phys. Rev. B*, 49:1407–1416, Jan 1994.

[12] N. Harima, A. Fujimori, T. Sugaya, and I. Terasaki. Chemical potential shift in lightly doped to overdoped $\mathrm{bi_2sr_2ca_{1-x}}R_x\mathrm{cu_2o_{8+y}}$ (r = Pr, er). *Phys. Rev. B*, 67:172501, May 2003.

[13] Claudio Giannetti, Massimo Capone, Daniele Fausti, Michele Fabrizio, Fulvio Parmigiani, and Dragan Mihailovic. Ultrafast optical spectroscopy of strongly correlated materials and high-temperature superconductors: a non-equilibrium approach. *Advances in Physics*, 65(2):58–238, March 2016.

[14] G. Ghiringhelli, N. B. Brookes, E. Annese, H. Berger, C. Dallera, M. Grioni, L. Perfetti, A. Tagliaferri, and L. Braicovich. Low energy electronic excitations in the layered cuprates studied by copper L_3 resonant inelastic x-ray scattering. *Phys. Rev. Lett.*, 92:117406, Mar 2004.

[15] Michael Tinkham. *Introduction to superconductivity*. Courier Corporation, 2004.

[16] H. J. A. Molegraaf, C. Presura, D. van der Marel, P. H. Kes, and M. Li. Superconductivity-induced transfer of in-plane spectral weight in $Bi_2Sr_2Ca_{0.92}Cu_2O_{\delta+8}$. *Science*, 295(5563):2239–2241, 2002.

[17] Andrea Damascelli, Zahid Hussain, and Zhi-Xun Shen. Angle-resolved photoemission studies of the cuprate superconductors. *Rev. Mod. Phys.*, 75:473–541, Apr 2003.

[18] Jianqiao Meng, Guodong Liu, Wentao Zhang, Lin Zhao, Haiyun Liu, Xiaowen Jia, Daixiang Mu, Shanyu Liu, Xiaoli Dong, Jun Zhang, Wei Lu, Guiling Wang, Yong Zhou, Yong Zhu, Xiaoyang Wang, Zuyan Xu, Chuangtian Chen, and X. J. Zhou. Coexistence of fermi arcs and fermi pockets in a high-tc copper oxide superconductor. *Nature*, 462(7271):335–338, November 2009.

[19] Enrico Maria Rigoni. *Ultrafast non-equilibrium studies of complex materials through pump-probe and stochastic spectroscopies*. PhD thesis, University of Trieste, 2023.

[20] Fabio Novelli. *In search of selective excitations for studying out-of-equilibrium properties in strongly correlated electron systems and high temperature superconductors*. PhD thesis, University of Trieste, 2012.

[21] Allen Rothwarf and B. N. Taylor. Measurement of recombination lifetimes in superconductors. *Physical Review Letters*, 19(1):27–30, July 1967.

[22] Claudio Giannetti, Giacomo Coslovich, Federico Cilento, Gabriele Ferrini, Hiroshi Eisaki, Nobuhisa Kaneko, Martin Greven, and Fulvio Parmigiani. Discontinuity of the ultrafast electronic response of underdoped superconducting $Bi_2Sr_2Ca_{0.92}Cu_2O_{\delta+8}$ strongly excited by ultrashort light pulses. *Physical Review B*, 79(22), June 2009.

[23] F. Boschini, E. H. da Silva Neto, E. Razzoli, M. Zonno, S. Peli, R. P. Day, M. Michiardi, M. Schneider, B. Zwartsenberg, P. Nigge, R. D. Zhong, J. Schneeloch, G. D. Gu, S. Zhdanovich, A. K. Mills, G. Levy, D. J. Jones, C. Giannetti, and A. Damascelli. Collapse of superconductivity in cuprates via ultrafast quenching of phase coherence. *Nature Materials*, 17(5):416–420, April 2018.

[24] D. Fausti, R. I. Tobey, N. Dean, S. Kaiser, A. Dienst, M. C. Hoffmann, S. Pyon, T. Takayama, H. Takagi, and A. Cavalleri. Light-induced superconductivity in a stripe-ordered cuprate. *Science*, 331(6014):189–191, 2011.

[25] F. Giusti, A. Marciniak, F. Randi, G. Sparapassi, F. Boschini, H. Eisaki, M. Greven, A. Damascelli, A. Avella, and D. Fausti. Signatures of enhanced superconducting phase coherence in optimally doped $\mathrm{bi_2sr_2y_{0.08}ca_{0.92}cu_2o_{8+\delta}}$ driven by midinfrared pulse excitations. *Phys. Rev. Lett.*, 122:067002, Feb 2019.

[26] F. Giusti, A. Montanaro, A. Marciniak, F. Randi, F. Boschini, F. Glerean, G. Jarc, H. Eisaki, M. Greven, A. Damascelli, A. Avella, and D. Fausti. Anisotropic time-domain electronic response in cuprates driven by midinfrared pulses. *Phys. Rev. B*, 104:125121, Sep 2021.

[27] Claudio Giannetti, Federico Cilento, Stefano Dal Conte, Giacomo Coslovich, Gabriele Ferrini, Hajo Molegraaf, Markus Raichle, Ruixing Liang, Hiroshi Eisaki, Martin Greven, et al. Revealing the high-energy electronic excitations underlying the onset of high-temperature superconductivity in cuprates. *Nature communications*, 2(1):353, 2011.

[28] F. Giusti, A. Marciniak, F. Randi, G. Sparapassi, F. Boschini, H. Eisaki, M. Greven, A. Damascelli, A. Avella, and D. Fausti. Signatures of Enhanced Superconducting Phase Coherence in Optimally Doped $\mathrm{Bi_2Sr_2Y_{0.08}Ca_{0.92}Cu_2O_{8+\delta}}$ Driven by Midinfrared Pulse Excitations. *Phys. Rev. Lett.*, 122:067002, Feb 2019.

[29] Chandrasekhara Venkata Raman and Kariamanikkam Srinivasa Krishnan. A new type of secondary radiation. *Nature*, 121(3048):501–502, March 1928.

[30] Francesca Giusti. *Intensity and fluctuation dynamics in pump-probe experiments in complex materials*. PhD thesis, University of Trieste, 2018.

[31] Manuel Cardona. Raman scattering in high tc superconductors: phonons, electrons, and electron–phonon interaction. *Physica C: Superconductivity*, 317–318:30–54, May 1999.

[32] Thomas P. Devereaux and Rudi Hackl. Inelastic light scattering from correlated electrons. *Reviews of Modern Physics*, 79(1):175–233, January 2007.

[33] Philip B. Allen. Fermi-surface harmonics: A general method for nonspherical problems. application to boltzmann and eliashberg equations. *Phys. Rev. B*, 13:1416–1427, Feb 1976.

[34] Francesco Randi. *Low-energy physics in strongly correlated materials via nonlinear spectroscopies*. PhD thesis, University of Trieste, 2016.

[35] Angela Montanaro, Enrico Maria Rigoni, Francesca Giusti, Luisa Barba, Giuseppe Chita, Filippo Glerean, Giacomo Jarc, Shahla Y. Mathengattil, Fabio Boschini, Hiroshi Eisaki, Martin Greven, Andrea Damascelli, Claudio Giannetti, Dragan Mihailovic, Viktor Kabanov, and Daniele Fausti. Dynamics of nonthermal states in optimally doped $Bi_2Sr_2Ca_{0.92}y_{0.08}Cu_2o_{8+\delta}$ revealed by midinfrared three-pulse spectroscopy. *Phys. Rev. B*, 110:125102, Sep 2024.

[36] D. Polli, D. Brida, S. Mukamel, G. Lanzani, and G. Cerullo. Effective temporal resolution in pump-probe spectroscopy with strongly chirped pulses. *Physical Review A*, 82(5), November 2010.

[37] Costanza Lincetto. Time-resolved raman measurements in the cuprate superconductor $Bi_2Sr_2Ca_{0.92}y_{0.08}Cu_2o_{8+\delta}$, 2023.

[38] Maria Recasens, Valentin Kasper, Maciej Lewenstein, and Allan S. Johnson. Chirped pulse control over the melting of superconductors. *Phys. Rev. B*, 111:064513, Feb 2025.

[39] Angela Montanaro. *Non-equilibrium response of quantum materials to resonant low-energy electronic photo-excitations*. PhD thesis, University of Trieste, 2021.

[40] T. P. Devereaux, D. Einzel, B. Stadlober, R. Hackl, D. H. Leach, and J. J. Neumeier. Electronic raman scattering in high-t_c superconductors: A probe of d_x^2-y^2 pairing. *Phys. Rev. Lett.*, 72:396–399, Jan 1994.

[41] T. P. Devereaux. Theory of electronic raman scattering in disordered unconventional superconductors. *Phys. Rev. Lett.*, 74:4313–4316, May 1995.

[42] R. P. Saichu, I. Mahns, A. Goos, S. Binder, P. May, S. G. Singer, B. Schulz, A. Rusydi, J. Unterhinninghofen, D. Manske, P. Guptasarma, M. S. Williamsen, and M. Rübhausen. Two-component dynamics of the order parameter of high temperature $bi_2sr_2cacu_2o_{8+\delta}$ superconductors revealed by time-resolved raman scattering. *Phys. Rev. Lett.*, 102:177004, Apr 2009.

[43] Giorgia Sparapassi. *Femtosecond Covariance Spectroscopy*. PhD thesis, University of Trieste, 2019.

[44] Jonathan Owen Tollerud et al. Femtosecond covariance spectroscopy. *Proceedings of the National Academy of Sciences*, 116(12):5383–5386, 2019.

[45] Giorgia Sparapassi, Stefano M. Cavaletto, Jonathan Tollerud, Angela Montanaro, Filippo Glerean, Alexandre Marciniak, Fancesca Giusti, Shaul Mukamel, and Daniele Fausti. Transient measurement of phononic states with covariance-based stochastic spectroscopy. *Light: Science & Applications*, 11(1), March 2022.

[46] Yong-Xin Yan, Edward B. Gamble, and Keith A. Nelson. Impulsive stimulated scattering: General importance in femtosecond laser pulse interactions with matter, and spectroscopic applications. *The Journal of Chemical Physics*, 83(11):5391–5399, December 1985.

[47] Filippo Glerean, Stefano Marcantoni, Giorgia Sparapassi, Andrea Blason, Martina Esposito, Fabio Benatti, and Daniele Fausti. Quantum model for impulsive stimulated raman scattering. *Journal of Physics B: Atomic, Molecular and Optical Physics*, 52(14):145502, June 2019.

[48] M.R. Presland, J.L. Tallon, R.G. Buckley, R.S. Liu, and N.E. Flower. General trends in oxygen stoichiometry effects on tc in bi and tl superconductors. *Physica C: Superconductivity*, 176(1–3):95–105, May 1991.

[49] Yao Wang, Martin Claassen, Chaitanya Das Pemmaraju, Chunjing Jia, Brian Moritz, and Thomas P Devereaux. Theoretical understanding of photon spectroscopies in correlated materials in and out of equilibrium. *Nature Reviews Materials*, 3(9):312–323, 2018.

[50] Angela Montanaro, Enrico Maria Rigoni, Francesca Giusti, Luisa Barba, Giuseppe Chita, Filippo Glerean, Giacomo Jarc, Shahla Y. Mathengattil, Fabio Boschini, Hiroshi Eisaki, Martin Greven, Andrea Damascelli, Claudio Giannetti, Dragan Mihailovic, Viktor Kabanov, and Daniele Fausti. Dynamics of nonthermal states in optimally doped $Bi_2Sr_2Ca_{0.92}Y_{0.08}Cu_2O_{8+\delta}$ revealed by midinfrared three-pulse spectroscopy. *Phys. Rev. B*, 110:125102, Sep 2024.

[51] Fabio Novelli, Jonathan O. Tollerud, Dharmalingam Prabhakaran, and Jeffrey A. Davis. Persistent coherence of quantum superpositions in an optimally doped cuprate revealed by 2d spectroscopy. *Science Advances*, 6(9):eaaw9932, 2020.

Ringraziamenti

Laser, coppie di Cooper, fasi della materia esotiche e misure che mi hanno fatto arrovellare il cervello per giorni eppure questa mi rimane la parte più difficile da scrivere, tante sono le persone che devo ringraziare, sperando che qualche parola su questa pagina vi possa comunicare un po' dell'affetto e della commozione che sto provando scrivendole. È la fine di un percorso di cinque anni, l'inizio di un'altra avventura per cui sono entusiasta ma che purtroppo mi fa allontanare da questa bellissima città e dalle tante persone a cui voglio bene che ci sono.

Ringrazio Daniele per avermi dato questo bellissimo progetto e la possibilità di far parte del suo gruppo nel dottorato che mi è ormai prossimo. Ringrazio i miei corelatori, Angela ed Enrico, specialmente quest'ultimo per aver sopportato i miei deliri in sei mesi di esperimenti.

Ringrazio Gabri C., Matteo e Marcello, che hanno cominciato il percorso al Collegio con me e sono tutti, come me, alla fine di esso, con mille avventure alle spalle. Ringrazio Marina, Gabriele 1 e Gianpaolo, compagni di innumerevoli caffè alle macchinette e dialoghi tutt'altro che sopra i massimi sistemi del mondo. Ringrazio gli amici del dipartimento, colleghi di sessioni di studio disperate in T17, di serate in BarH davanti ad una fidatissima Lasko, di abbondanti spaghettate e di parole crociate a barcola. Ringrazio Mattia e Andrea, che spero di poter rivedere davanti a un bel fritto di pesce a Numana; ragazzi, quanto siamo cresciuti.

Grazie a Rick per aver sopportato questo compagno di stanza per 5 anni, chissà chi ci succederà in 326. Ringrazio i tanti amici del Collegio sparsi per il mondo, che vorrei rivedere di piu. Ringrazio gli amici della 333: Yous, Anto, Ermes, Stefano, Marta, Sara e Anna con cui credo di aver condiviso dei momenti più identificabili con la famiglia che con l'amicizia.

Parlando di famiglia, più cresco e più mi rendo conto della mia fortuna, di aver avuto dei genitori stupendi che hanno supportato, supportano le mie scelte e che mi hanno dato tantissimo, così tanto che la commozione dello scrivere "vi voglio bene" mi fa tremare. Lo sapete, ma non ve lo dico abbastanza. A concludere questi ringraziamenti ci sei tu Marti, perché non c'è migliore conclusione: sei il il più grande complimento che si possa fare alla mia vita. Grazie per tutto quello che mi dai e per supportarmi in questo viaggio.